FEDERAL UNIVERSITY OF CEARÁ

CENTER OF SCIENCE

PHYSICS DEPARTMENT

GRADUATE PROGRAM IN PHYSICS

MARIA CLARA FERNANDES DE ANDRADE

A STUDY ON CASHEW BAGASSE HYDROCHARS AND PYROCHARS AND THEIR INTERACTION WITH WATER AND SOIL

FORTALEZA

2020

MARIA CLARA FERNANDES DE ANDRADE

A STUDY ON CASHEW BAGASSE HYDROCHARS AND PYROCHARS AND THEIR INTERACTION WITH WATER AND SOIL

Master's Thesis presented to Federal University of Ceará Graduate Program in Physics, as a partial requirement to obtain the Master in Physics title. Concentration Area: Condensed Matter Physics.

Academic Supervisor: Dr. Odair Pastor Ferreira.

FORTALEZA

2020

Dados Internacionais de Catalogação na Publicação
Universidade Federal do Ceará
Sistema de Bibliotecas
Gerada automaticamente pelo módulo Catalog, mediante os dados fornecidos pelo(a) autor(a)

A568s Andrade, Maria Clara Fernandes de.
A study on cashew bagasse hydrochars and pyrochars and their interaction with water and soil / Maria Clara Fernandes de Andrade. – 2020.
104 f. : il. color.

Dissertação (mestrado) – Universidade Federal do Ceará, Centro de Ciências, Programa de Pós-Graduação em Física, Fortaleza, 2020.
Orientação: Prof. Dr. Odair Pastor Ferreira.

1. Carbonização hidrotérmica. 2. Pirólise.. 3. Ativação termoquímica. 4. Interação água-biochar. I. Título.
CDD 530

MARIA CLARA FERNANDES DE ANDRADE

A STUDY ON CASHEW BAGASSE HYDROCHARS AND PYROCHARS AND THEIR INTERACTION WITH WATER AND SOIL

Master's Thesis presented to Federal University of Ceará Graduate Program in Physics, as a partial requirement to obtain the Master in Physics title. Concentration Area: Condensed Matter Physics.

Approved in: 22/12/2020

EXAMINATION COMMISSION

_____
Prof. Dr. Odair Pastor Ferreira
Federal University of Ceará (UFC)

_____
Prof. Dr. Antonio Gomes de Souza Filho
Federal University of Ceará (UFC)

_____
Prof.ª Dra. Andreia Fonseca de Faria
University of Florida

_____
Prof. Dr. Jaedson Cláudio Anunciato Mota
Federal University of Ceará (UFC)

To my family, friends and teachers.

ACKNOWLEDGMENTS

To FUNCAP for its financial support through the maintenance of the scholarship.

To my Academic Supervisor, Dr. Odair Pastor Ferreira, for giving me the best guidance possible and for being very present during the project.

To the professors from the examination commission Prof. Dr. Odair Pastor Ferreira, Prof. Dr. Antonio Gomes de Souza Filho, Prof.ª Dra. Andreia Fonseca de Faria, Prof. Dr. Jaedson Cláudio Anunciato Mota for the time, for the valuable collaborations and suggestions.

To my parents, who always provided me with the material and psychological help I needed.

To my brother Breno, who has always been by my side.

To my grandfather Joaquim Fernandes Alves who provided me with the raw material for this work and a great stimulus to my scientific career.

To my friend Leandro, who has been with me since your bachelor's degree, in the most difficult and decisive moments.

To my colleagues from LaMFA, Laís Helena, Laís Fregolente, Victor, Janaína, Pamella, Camila, Yasmine, Cecília, Anupama and other participants, who gave me the work environment that I always wished and that will be forever in my heart.

To the past and current members of the Department of Physics, who built a world-class infrastructure and materially made this work possible.

To the Analytical Center of the Federal University of Ceará, for the microscopies.

We thank the X-Ray Laboratory of the Federal University of Ceará for providing the XRD analyses.

To Prof. Dr. Alejandro Pedro Ayala and Dr. Bruno Sousa Araújo, for the DSC and STA training.

To the Soil Physics Laboratory of the Federal University of Ceará for the water retention measurements.

And finally, to the people of Ceará, my first and main inspiration for the development of this study. May we through knowledge, work, respect and compassion give each other more and more life quality for years to come.

“O silêncio também é uma sabedoria. Assim em seu silêncio Fabiano pensava. Se chover, tudo se proverá. Ali calado na sua mais profunda melancolia suspirou e devaneou. Sonhou com a chuva, os pastos verdes, os meninos correndo atrás das cabras. Sonhou com Sinhá Vitória dormindo numa cama, uma cama melhor do que a do senhor Tomás da bolandeira. Choveu.”

Vidas Secas, Graciliano Ramos

ABSTRACT

The Northeast of Brazil has been facing throughout its history problems related to severe droughts. Different projects should be suggested in order to minimize this problem. Among them are new soil additives as biochars, materials made from biomass that, among many possibilities, have the potential to increase the water retention capacity of the soil to which it are added. In order to elucidate the possibility of the preparation of biochar with biomass from the Northeast region, this work was developed with cashew bagasse as the precursor. The objective was to study the preparation, characterization and activation of these biochars and clarify the interactions between them and water. So, in Stage I cashew bagasse was first dried and grounded, and then charred by two methodologies: pyrolysis and hydrothermal carbonization. The pyrolysis process took place at 350, 450 and 550 °C during 90 min and the hydrothermal carbonization reaction at 200 and 250 °C for 4 and 24 h. Both were performed with 2 grams. The biochars were then characterized by CHNS Elemental Analysis, Fourier Transform Infrared Spectroscopy (FT-IR), Raman Spectroscopy, X-Ray Diffraction (XRD), Scanning Electron Microscopy (SEM) and N_2 Adsorption-Desorption Isotherms. It was observed that the pyrochar at 450 °C had very similar compositional results to the 550 °C pyrochar. For hydrochars, it was evident that the increase of reaction time from 4 to 24 h did not cause significant differences. For Stage II, a new batch of cashew bagasse was retrieved to produce hydrochars (200 and 250 ° C for 4 h) and pyrochars (350 and 550 °C) using 13.5 g of cashew bagasse. The increase from 2 to 13.5 grams and the new cashew bagasse batch did not cause significant differences in structure, composition and texture of the carbonaceous materials. Stage II samples were activated with KOH in the 1:2 weight ratio of carbon per KOH for 1 h at 700 °C and characterized by the same techniques used before. It was observed that even though precursor biochars presented very different profiles, activated samples were very similar to each other in structure, composition and texture. Surface area increased from 13 ~ 33 m^2/g to 598 ~ 847 m^2/g. The thermochemical activation process promoted a decreased in the contact angles with distilled water for all samples, suggesting enhancing in the hydrophilicity. When added to soil in 1 % of mass, activated biochar increased soil Plant Available Water Capacity (PAWC) from 0.40 % to 4.35 ~ 6.30 %. Differential Scanning Calorimetry (DSC) results for water-biochar interactions did not present any easily distinguishable pattern, although for the best PAWC sample (CH_250 KOH), bulk water supercooling was softened and micropore lodged water appeared after activation. The results of cashew bagasse experiments present improvement when compared to experiments with different raw materials described in the literature, meaning that it would probably be suitable to be used as soil conditioner.

Keywords: Hydrothermal Carbonization. Pyrolysis. Thermochemical Activation. Water-Biochar Interaction.

RESUMO

O Nordeste do Brasil vem enfrentando ao longo de sua história problemas relacionados a secas severas. Diferentes projetos devem ser sugeridos para minimizar este problema. Entre eles, estão novos aditivos para o solo, como o biochar, material feito a partir da biomassa que, entre muitas possibilidades, tem o potencial de aumentar a capacidade de retenção de água do solo ao qual é adicionado. Com o objetivo de elucidar a possibilidade de preparação do biochar com biomassa da região Nordeste, este trabalho foi desenvolvido tendo como precursor o bagaço de caju. O objetivo foi estudar a preparação, caracterização e ativação desses biochars e esclarecer as interações entre eles e a água. Assim, no Estágio I do projeto o bagaço do caju foi primeiro seco e moído, e então carbonizado por duas metodologias: pirólise e carbonização hidrotérmica. O processo de pirólise ocorreu a 350, 450 e 550 °C durante 90 min e a reação de carbonização hidrotérmica a 200 e 250 °C por 4 e 24 h. Ambos foram realizados com 2 gramas. Os biochars foram então caracterizados por Análise Elementar CHNS, Espectroscopia no Infravermelho com Transformada de Fourier (FT-IR), Espectroscopia Raman, Difração de Raios-X (XRD), Microscopia Eletrônica de Varredura (MEV) e Isotermas de Adsorção-Dessorção de N_2. Foi observado que o carvão pirolítico de 450 °C tinha composição muito semelhante ao de 550 °C. Já para os carvões hidrotérmicos, ficou evidente que o aumento do tempo de reação de 4 para 24 h não causou diferenças significativas. No Estágio II do projeto, um novo lote de bagaço de caju foi coletado para produzir para ativação termoquímica carvões hidrotérmicos (200 e 250 °C por 4 h) e carvões pirolíticos (350 e 550 °C) usando 13,5 g de bagaço de caju. Para ambas as metodologias, foi realizado um estudo comparativo dos resultados da carbonização com 2 e 13,5 gramas. O aumento de 2 para 13,5 gramas e os diferentes lotes de bagaço de caju não causaram diferenças significativas na estrutura, composição e textura das amostras. Os parâmetros de carbonização das amostras do Estágio II foram selecionados de acordo com as conclusões anteriores. Amostras do Estágio II foram ativadas com KOH na proporção de 1:2 em peso de carbono por KOH por 1 h a 700 ° C e caracterizadas pelas mesmas técnicas utilizadas anteriormente. Foi observado que embora os biochars precursores apresentassem perfis muito diferentes, as amostras ativadas eram muito semelhantes entre si em estrutura, composição e textura. A área de superfície aumentou de 13 ~ 33 m^2/g para 598 ~ 847 m^2/g com a ativação. A ativação aumentou o ângulo de contato com a água destilada, tornando todas as amostras hidrofílicas. Ao ser adicionado ao solo na proporção de 1 % de massa, o biochars ativado aumentou a Capacidade de Água Disponível para as Plantas de 0,40 % para 4,35 ~ 6,30 %. Os resultados da Calorimetria Diferencial de Varredura para as interações água-biochar não apresentaram nenhum padrão facilmente distinguível, embora para a melhor amostra PAWC (CH_250 KOH), o super-resfriamento

da água bulk foi suavizado e a presença de água alojada nos microporos foi evidenciada pelo teste após a ativação. Os resultados dos experimentos com bagaço de caju se apresentam melhorias aos resultados com diferentes matérias-primas descritas na literatura, o que significa que provavelmente seria adequado para ser usado como condicionador de solo.

Palavras-chave: Carbonização Hidrotérmica. Pirólise. Ativação Termoquímica. Interação Água-Biochar.

LIST OF FIGURES

Figure 1 – FT-IR spectra of hydrochars from Stage I…….. 41

Figure 2 – Raman spectra of hydrochars from Stage I……. 44

Figure 3 – X-ray diffractograms (XRD) of cashew bagasse (BC), cellulose and hydrochars from Stage I……. 46

Figure 4 – N_2 adsorption-desorption isotherms at 77 K for bagasse (BC) and hydrochars from Stage I…… 48

Figure 5 – Pore size distribution obtained by BJH method of bagasse (BC) and Hydrochars from Stage I…….. 49

Figure 6 – SEM images of three selected hydrochars produced in Stage I …… 50

Figure 7 – FT-IR spectra of BC and pyrochars from Step I…… 53

Figure 8 – Raman spectra of BC and Stage I pyrochars…… 54

Figure 9 – X-ray diffractograms (XRD) of cashew bagasse (BC), cellulose and pyrochars from Stage I…….... 55

Figure 10 – N_2 adsorption-desorption isotherms for cashew bagasse (BC) and pyrochars from Stage I at 77 K...……..…… 57

Figure 11 – Pore size distribution for cashew bagasse (BC) and pyrochars from Stage I obtained by BJH method ……. 58

Figure 12 – SEM images of pyrochars from Stage I……. 59

Figure 13 – FT-IR spectra of cashew bagasse (BC_2) and hydrochars and pyrochars produced in Stage II with 13.5 g…….. 63

Figure 14 – Raman spectra of cashew bagasse (BC_2) and hydrochars and pyrochars produced in Stage II with 13.5 g …… 64

Figure 15 – XRD diffractograms of cashew bagasse (BC_2), cellulose, hydrochars and pyrochars produced in Stage II with 13.5 g …… 65

Figure 16 – N_2 adsorption-desorption isotherms for cashew bagasse (BC_2) and biochars from Stage II and cashew bagasse (BC_2) at 77 K …… 67

Figure 17 – Pore size distribution for cashew bagasse (BC_2) and biochars from Stage II obtained by BJH method ……. 68

Figure 18 – SEM images of cashew bagasse (BC_2) and hydrochars and pyrochars produced in Stage II with 13.5 g …….. 70

Figure 19 – Van Krevelen Diagram for biochars produced in Stage II using 13.5 g of cashew bagasse (BC) and KOH activated biochar prepared at 700 °C.…… 73

Figure 20 – FT-IR spectra of the KOH activated biochars at 700 °C …… 74

Figure 21 – Raman spectra of activated biochar produced by KOH activation at 700 °C …. 75
Figure 22 – X-ray diffractograms (XRD) of activated biochars produced by KOH activation at 700 °C …….. 76
Figure 23 – N_2 adsorption-desorption isotherms at 77 K for KOH activated samples …… 77
Figure 24 – Pore size distribution for KOH activated samples from Stage II obtained by BJH method …….. 78
Figure 25 – SEM images of activated biochars produced by KOH activation at 700 °C … 79
Figure 26 – Illustrative image of the contact angle for a drop of water on a (a) hydrophilic solid surface and on a (b) hydrophobic solid surface…….. 81
Figure 27 – Stage II samples and activated ones on ultrapure water after agitation and allowed to settle for 3 min. For these pictures a small quantity of biochar was agitated with 20 mL of ultrapure water ……. 83
Figure 28 – Results of plant available water capacity (PAWC) expressed as percentage of mass gain for Stage II activated and non-activated samples. Soil was described for comparison ……. 87
Figure 29 – Plant Available Water Capacity and Water holding Capacity linear regression for activated and non-activated samples from Stage II. Soil is described for comparison …… 88
Figure 30 – Differential scanning Calorimetry (DSC) curves recorded during the cooling process on the second run for activated and non-activated hydrochars from Stage II with different water contents. Moist contents were calculated according to Equation 5……. 90
Figure 31 – Differential scanning Calorimetry (DSC) curves recorded during the cooling process on the second run for activated and non-activated pyrochars from Stage II with different water contents. Moist contents were calculated according to Equation 5…….. 91
Figure 32 – Peak area (J/g) calculated from DSC curves for bulk water solidification around – 20 and – 10 °C ……. 92

LIST OF TABLES

Table 1 – Main products exported by Ceará 2018-2019 ……. 20

Table 2 – Results of elemental analyses, initial and final reactional pH, yields, ash and water contents for Stage I hydrochars and BC……. 39

Table 3 – Attempted attributions for the vibrational bands from FT-IR spectra in the 4000-600 cm^{-1} region..... 42

Table 4 – I_D/I_G Ratios of Stage I hydrochars.……... 45

Table 5 – Textural properties of cashew bagasse (BC) and hydrochars from Stage I... 47

Table 6 – Results of CHNS elemental analyses, yields, ash and water contents for BC and Stage I pyrochars ……. 51

Table 7 – I_D/I_G Ratios of Stage I pyrochars …… 54

Table 8 – Textural properties of cashew bagasse (BC) and pyrochars from Stage I … 56

Table 9 – pH measurements for the samples from Stage I …….. 60

Table 10 – Results of CHNS elemental analyses, ash and water contents, initial and final reactional pH of hydrothermal carbonization and yields for biochars prepared with 13.5 g in Stage II …… 62

Table 11 – I_D/I_G ratios for biochars produced in Stage II with 13.5 g …….. 64

Table 12 – Textural Properties of cashew bagasse (BC_2) and hydrochars and pyrochars produced in Stage II with 13.5 g ……. 65

Table 13 pH results for cashew bagasse (BC_2) and biochars from Stage II…… 69

Table 14 – Results of CHNS elemental analyses, ash and water contents and yields for thermochemical activated biochars treated with KOH at 700 °C …….. 72

Table 15 – I_D/I_G ratios of activated biochars produced by KOH activation at 700 °C…….. 75

Table 16 – Textural Properties of activated biochars produced by KOH activation at 700 °C 76

Table 17 – pH results for KOH activated samples from Stage II…… 80

Table 18 – Results of contact angle measured by sessile drop method for cashew bagasse (BC_2), samples produced in Stage II and activated biochars with KOH …….. 81

Table 19 – Results of water holding capacity (WHC) expressed as percentage of mass gain for non-activated and activated and samples. Soil was described for comparison… 84

Table 20 – Physicochemical properties of the soil used in the plant available water capacity (PAWC) tests …….. 85

Table 21 – Achievements for Plant Available Water Capacity (PAWC) from Literature ….. 89

LIST OF ABBREVIATIONS AND ACRONYMS

ASN	Agência Sebrae de Notícias
BET	Brunauer–Emmett–Teller
CH	Carvão Hidrotérmico
CP	Carvão Pirolítico
DSC	Differential Scan Calorimetry
EMBRAPA	Empresa Brasileira de Pesquisa Agropecuária
FBW	Freezable Bound Water
FFW	Freezable Free Water
FT-IR	Fourier-transform infrared spectroscopy
IBGE	Instituto Brasileiro de Geografia e Estatística
IPECE	Instituto de Pesquisa e Estratégia Econômica do Ceará
LaMFA	Laboratório de Materiais Funcionais Avançados
MIDIC	Ministério da Indústria, Comércio Exterior e Serviços
NFW	Non-Freezable Water
PAWC	Plant Available Water Capacity
SEBRAE	Serviço Brasileiro de Apoio às Micro e Pequenas Empresas
SECEX	Secretaria de Comércio Exterior
SEM	Scanning Electron Microscopy
TGA	Thermal Gravimetric Analysis
WHC	Water Holding Capacity
XRD	X-Ray Diffraction

TABLE OF CONTENTS

1	**INTRODUCTION**	18
1.1	**Cashew Value Chain and Sustainable Biochar Production**	19
1.2	**Carbonization Methods for Biochar Production**	21
1.2.1	***Activation***	23
1.3	**Conditioning Soil with Biochar**	24
1.4	**Water retention on soil amended with Biochar**	25
1.5	**State of the Art in Water-Biochar Interaction**	25
2	**OBJECTIVES**	30
3	**EXPERIMENTAL PART**	31
3.1	**Biomass Acquisition**	31
3.2	**Cashew Bagasse Pretreatment and Characterization**	31
3.3	**Hydrothermal Carbonization of Cashew Bagasse**	32
3.4	**Pyrolysis of Cashew Bagasse**	33
3.5	**Biochar KOH Activation**	33
3.6	**Hydrochar and Pyrochar characterizations**	34
3.7	**Biochar-Water Interaction Evaluation**	35
3.8	**Water retention of Biochar added to Soil**	37
4	**RESULTS AND DISCUSSION**	38
4.1	**Stage I – Study of Cashew Bagasse Carbonization Parameters**	38
4.1.1	***Hydrochars***	38
4.1.2	***Pyrochars***	50
4.1.3	***Pyrolysis and Hydrothermal Carbonization: A Comparison***	59
4.2	**Evaluation of Precursor Mass in the Carbonization Reactions**	61
4.3	**Stage II – Thermochemical Activation of Cashew Bagasse Biochars**	71
4.4	**Water-biochar interaction and water retention capacity**	80
4.4.1	***Wetting properties***	80
4.4.2	***Plant Available Water Capacity (PAWC) test***	85
4.4.3	***Low-temperature Differential Scanning Calorimetry (DSC) analysis***	89
5	**CONCLUSIONS**	95

6 **BIBLIOGRAPHY**.....…….. 97

1 INTRODUCTION

The Laboratory of Advanced Functional Materials (LaMFA) has been working on many projects that use hydrothermal carbonization for different purposes. Among them, there are the production of hydrochar from sugarcane bagasse and vinasse (SILVA, 2017; BENTO et al., 2019; DO SANTOS et al., 2020; FREGOLENTE et al., 2020), studies with iron-carbon hybrid materials (CASTRO, 2018; SOARES, 2017; VIEIRA et al., 2016; VIEIRA et al., 2020), preparation of carbon micro and nanoparticles for interaction with proteins (CASTRO, 2017; CASTRO et al., 2017) and hydrothermal carbonization for fuel production (COSTA et al., 2019).

On the context of carbonized biomass addition to the soil, the first experiments on a controlled environment begun in the early 2000s (LEHMANN; GAUNT; RONDON, 2006). In 2005, the term "biochar" was coined by Peter Read, a researcher at Massey University, New Zealand. The term defined pyrolysed biomass for use as soil conditioner (READ, 2009). Biochar made by pyrolysis is also called pyrochar. Later on, this term was also used to refer to hydrothermally carbonized biomass (also called hydrochar) (SOHI et al., 2010). In contrast, the term coal, refers to carbonaceous materials found in underground natural reservoirs and is widely used as a fuel (NWAKA et al., 2016). In this work, we will use "biochar" to refer to both pyro and hydrochar.

On the context of research on biochar, according to the International Biochar Initiative (IBI), there are groups focused on the promotion of biochar for agriculture in the five continents, mainly in the most developed countries (IBI, c2018). According to the virtual platform, biochar benefits to soil are: carbon sequestration (helps to combat global warming and assists in low-carbon economy); positive impacts on water quality (reduced nutrient leaching); increase in soil fertility, thereby increasing food security and preserving the diversity of cultivated land; reduced need for chemical fertilizer; reduction of agricultural waste (as it is used as raw material for biochar production); reduced erosion and soil degradation and decreased loss of native vegetation, making arable land more fertile and, as our goal, higher soil water retention (IBI, c2018).

The inspiration to use carbonized biomass as soil conditioner comes from the so-called Terra Preta de Indio, present in Amazonian areas, occupying strips of land from about 10,000 m^2 to several hundred hectares (USBI, 2020). The theory about its formation is that rubbish (ashes and charcoal, feces, bones and household waste) from indigenous villages accumulated in those areas and eventually decomposed and gave rise to a soil that was extremely rich in organic carbon (what justifies the dark aspect of these soils), as well as phosphorus, calcium, magnesium, zinc and manganese (OLIVEIRA et al., 2018; TEIXEIRA et al., 2009). Such soils have high fertility as their

main feature because of, among other reasons, the large amount of organic matter becomes a source of energy and nutrients for microorganisms and plants. This is the principle used when adding pyrolytic or hydrothermal chars to the soil, as it aims to mimic the carbon found in anthropogenic dark earth, i.e., to condition the soil so that it has similar features to Amazonian Dark Earths (TEIXEIRA et al., 2009).

This Thesis will study the biochar produced from cashew bagasse, since it is known from the literature that biochar produced from biomass has shown good results in sandy soils in water retention and increase of organic matter (MANGRICH, 2015; LIU et al., 2017; MOLLINEDO et al., 2015; SULIMAN et al., 2017). The biochar-water interaction study will be the objective of this work. Thus, if such a proposal reached product level, there would be water savings for irrigation and added value to the waste.

A quick approach to the main methods of preparation of biochar and the main properties of biochar made from cellulosic materials will be carried out and the advances in this area will be addressed to situate the research on the problem.

1.1 Cashew Value Chain and Sustainable Biochar Production

Within the context of agriculture, the use of biochar comes as an answer to two problems. The first one concerns sustainable economy, due to the fact that biochar can be produced from waste, making it possible to reinsert it into the value chain. The second, already exposed, comes from the possibility that biochar could improve the soil to which it is added, since Ceará's soil is mainly sandy and there is a historical problem of drought in the region.

In order to discuss the choice of the object of study (biochar) and its raw material (cashew bagasse), the importance of cashew for the northeastern economy will be addressed, providing some information regarding the local climate and the cashew value chain. Firstly, the cashew market will be characterized and how it generates several tons of bagasse that are not reused will be explained.

After World War II, various policies were given to encourage cashew farming in Brazil due to the great economic interest in cashew nuts. Thus, today, there is an expressive area with cashew trees. When it comes to fruit species in Brazil, this area is the third largest, being surpassed only by orange and banana trees (IBGE, 2018). In Ceará, much of this area is located on the state coast.

In northeastern Brazil, cashew nut production alone stands out from other cashew products and makes up a good slice of the economy. The market for this sector produces around 130 thousand

tons of nuts per year (BRAINER and VIDAL, 2018), making up more than 180 million dollars in exportation in Ceará between 2018 and 2019 (IPECE, 2020) , as shown in Table 1.

Table 1 – Main products exported by Ceará - 2018-2019

Product Description	2018		2019		Var %
	US$	Part %	US$	Part %	
Metallurgical Products	1,390,160,207	59.36	1,208,661,751	53.36	-13.06
Footwear and it's parts	266,991,847	11.4	235,915,996	10.42	-11.64
Electric machines, apparatus and materials and it's parts	65,222,451	2.78	175,331,707	7.74	168.82
Cashew nuts, fresh or dried, without shell	94,182,618	4.02	99,001,930	4.37	5.12
Ind. Food Products And baby	84,106,051	3.59	81,574,077	3.6	-3.01
Vegetable Waxes	55,090,371	2.35	68,797,361	3.04	24.88
Fruits (except cashew)	85,924,813	3.67	62,143,610	2.74	-27.68
Lobster	42,087,459	1.8	58,328,818	2.58	38.59
Leather and fur	75,725,266	3.23	52,793,292	2.33	-30.28
Mineral and Derived fuels	18,958,439	0.81	51,325,606	2.27	170.73
Other products	163,628,825	6.99	171,059,599	7.55	4.54
Ceará	2,342,078,347	100	2,264,933,747	100	-3.29

Source: SECEX/MDIC. Elaborated by IPECE, 2020.

During industrial management of cashew, it is separated in two parts: the chestnut (true fruit and high-quality almond) and the peduncle (the false fruit rich in vitamin C). The chestnut is made of the shell and the almond, and they are used separately: cashew nut liquid (used in varnishes, paints, etc.) is extracted from the shell and the film that coats the almond and the almond itself are used for food and balsam/creams. The peduncle is used to produce integral juice, nectar, tropical juice, *cajuína*, pulp and cashew candies. During the manufacture of those products, large quantities of bagasse are produced (LIMA et al., 2016).

According to Serrano et al. (2016), to meet the demand for cashew nuts, about 75 % of cashew peduncle production is not commercially consumed, i.e., most of the peduncles are not used after the removal of the nut, besides the organic matter left after the production of juices and candies. Also, according to Serrano et al. (2016), Brazil commercially uses about 350 thousand tons of cashew peduncle per year (which would correspond to the 25 % that are used not necessarily to meet the

demand for cashew nuts and most of it is used in a manner not to consume the bagasse, as in juices and nectar), then annually thousands of tons of bagasse would become waste. These huge amounts of waste require sustainable solutions in order to mitigate losses and provide optimal utilization of raw materials.

The alternative that researchers have been developing to take advantage of the bagasse is the production of human groceries (through the manufacture of flours, dietary fibers, hamburgers, biscuits, breads and snacks, as well as serving as a functional food component), animal feed, dyes, biogas, adsorbents for effluent treatment, substrates for enzyme production, mineral aromas and soil conditioners (MELLO, 2015; SIQUEIRA; BRITO, 2013). However, it is known that its use as animal feed is restricted due to the high concentration of tannin that can inhibit the absorption of other nutrients, which can cause starvation (MELLO, 2015). Also, raw biomass is reported to be unstable when applied to soil and to decompose fast (LIBRA et al., 2011). According to the study by Queiroz et al. (2010) application of fresh bagasse on soil did not represent any advantage as a soil conditioner during the 8 months of experiment. Therefore, it is expected that cashew bagasse will need an extra step of modification to be applied as a soil conditioner.

Besides the issue of waste management, cashew production has other obstacles still in the planting phase. The crop is often affected by deficient rainfall in some regions and by the pH of northeastern soils that tend to be lower than optimal for cultivation (BRAINER and VIDAL, 2018; TANIGUCHI; CRISOSTOMO, 2016).

In this context, the use of bagasse as a raw material for biochars would add value to the cashew industry by-product while soil conditions would be improved as pointed out by studies already described in the literature (MANGRICH et al., 2015; LIU et al., 2017; NOVOTNY et al., 2015; KALDERIS; PAPAMELETIOU; KAYAN, 2019; LIU et al., 2019).

1.2 Carbonization Methods for Biochar Production

Biochar can be obtained by various techniques including gasification, pyrolysis, hydrothermal liquefaction, microwave, roasting and hydrothermal carbonization. In all of these procedures, biomass is transformed into a highly stable carbon-rich material (NOVOTNY et al., 2015). The methods used in this work were hydrothermal carbonization and pyrolysis.

Both pyrolysis and hydrothermal carbonization carried out carbonization via thermal treatment. However, in order to obtain hydrochar, the process takes place in aqueous medium, closed reactor and, consequently, self-generated pressure (NOVOTNY et al., 2015; CASTRO, 2018, 2017;

SOARES, 2017). Hydrothermal carbonization is performed at temperatures between 100 and 300 °C and hydrolysis, dehydration, elimination and condensation reactions of sugars, polysaccharides and lignin from biomass occur forming amorphous and porous carbonaceous materials (MELO et al., 2017; NOVOTNY et al., 2015). Reaction parameters are determinant for hydrochar properties. Temperature has been reported to be inversely proportional to solid yield and oxygen content and directly to carbon content, with an enhancement of the heating value (ROMÁN et al., 2018). Temperature, associated to reaction time (which some authors associate as a single parameter, the reaction severity) has been known to influence carbonization degree, with higher severity being correlated with the accelerating of carbonization reactions (GUO et al., 2016). Reaction time sole influence is less studied, but it is also important. It depends on heating rate and/or residence times (ROMÁN et al., 2018).

According to Guo et al. (2016), regarding the increase of precursor mass in the reaction, the ratio between water and biomass has also a significant effect on the hydrochar yield. The researchers observed that as the ratio of water to biomass increases, hydrochar yield decreases. This is consistent with other studies that have shown that the concentration of intermediate compounds in the liquid phase may increase faster and the polymerization reaction may start earlier with a lower water/biomass ratio. This would lead to inhibiting more conversions, i.e., it would need a higher reaction severity (longer times or temperatures) to promote new reactions if less water is available (GUO et al., 2016).

On the other hand, pyrolysis consists of an endothermic process of thermal degradation of biomass under limited oxygen atmosphere, thus forming gaseous, liquid and solid compounds such as coal, bio-oil and CO_2, CO and CH_4 as products (ATKINSON et al., 2010; BANKS et al., 2016). Temperature reactions vary between 300 and 700 °C, first evaporating the water present in the sample, then detaching volatile compounds and further leading to aromatization and graphitization due to carbonization reactions. The process is based on the concomitant carbonization of lignin, cellulose and hemicellulose. The yield and quality of the product depend on the reaction parameters like temperature, residence time, biomass composition and heating rate. Biomass composition affects pyrochar properties in the sense that cellulose content present in the biomass helps in the formation of liquid products while high lignin content is favorable for the solids production. Also, moisture present in the biomass can inhibit the char formation. Temperature is reported to be the main parameter which controls the biochar yield. High temperature leads to low solid yield and high gaseous and liquid yield. Also, large particle size is reported to create a temperature gradient between

biomass core and outer surface which in turn suits the formation of solid products (TRIPATHI; SAHU; GANESAN, 2016).

1.2.1 Activation

Also, biochar properties can be designed by post-treatments outside carbonization like physico-chemical activation. Activation can be achieved by steam and heat (that is considered as physical activation) or by addition of chemicals and heating (chemical activation). These processes can be used mainly to achieve larger specific surface area and porosity (AZARGOHAR; DALAI, 2008; JIN et al., 2014; QIU et al., 2018).

Chemical activation was used in this work and it consists on mixing biochar with an activation agent (for example KOH), and applying heat to it on a pyrolysis-like procedure (ISLAM et al., 2017; LUO et al., 2016; QIU et al., 2018; UÇAR et al., 2009). During activation reaction, KOH reacts with the carbon present in the biochars at high temperatures as shown in Reactions 1 through 7 below (HUI; ZAINI, 2015):

1) $2KOH \rightarrow K_2O + H2O$
2) $C + H_2O \rightarrow H_2 + CO$
3) $CO + H_2O \rightarrow H_2 + CO_2$
4) $K_2O + CO_2 \rightarrow K_2CO_3$
5) $K_2O + H_2 \rightarrow 2K + H_2O$
6) $K_2O + C \rightarrow 2K + CO$
7) $K_2CO_3 + 2\ C \rightarrow 2\ K + 3\ CO$
8) $K_2CO_3 + 2\ HCl \rightarrow 2\ KCl + H_2O + CO_2$

Thus, the gases and volatile matter formed due to carbonaceous matrix degradation and products decomposition due to the reactions between KOH and carbonaceous matrix (reactions 1 to 7) produces pores and channels in the activated carbon. Reaction 8, refers to washing biochar after activation with HCl. The acid reacts with K_2CO_3 forming water, CO_2 and KCl that is later solubilized in water and eliminated from the samples.

Other than changes in texture (surface area, porosity, etc.), activation can lead to increase in carbon crystallite size (LEE et al., 2019) and as will be discussed later, increase in carbon content (due to the higher activation temperatures that it can enhance further decomposition of samples) and wettability.

According to literature, KOH activation leads to high micropore formation and can increase biochar specific surface area from 10 to 1500 m^2/g (AZARGOHAR and DALAI, 2008). Also, according to Wang et al. (2012), KOH activation can enhance the integration of small mesopores and micropores into the framework of various nanostructured carbons that drastically increases the interconnected pore networks and porosity, while maintaining the original textural properties (morphology, pore size, etc.)

1.3 Conditioning Soil with Biochar

Hydro and pyrochars are carbon-rich, microporous, structurally disordered materials that may have a highly functionalized or non-functionalized surface (AZARGOHAR; DALAI, 2006; KHAN et al., 2019). Depending on the raw material and the methodology, reactions will produce carbonaceous materials with different properties and several functionalities applicable to soils. Carbon fixation is one of these properties, since the structure of the biochars are more recalcitrant than biomass and can interfere on microbial activity responsible for organic matter decomposition (YOUSAF et al., 2017).

Regarding pyrochars, this material could increase soil pH (liming potential); since cations, such as calcium, potassium, magnesium, sodium and silicon, from the raw material form carbonates and/or oxides during pyrolysis (BREWER et al., 2012; ENDERS et al., 2012), allowing their reaction with acidic compounds, decreasing the acidity and thereby increasing the pH. It should be noted that such reaction will not occur for already alkaline soils (DAI et al., 2017).

Another very desired feature is the capacity to supply nutrients. As previously mentioned, phosphorus, calcium, magnesium, zinc, manganese and carbon remained in the biochars from the original biomass. These nutrients are particularly important to recover degraded soils and stimulate vegetation growth, which can protect the soils (UZOMA et al., 2011). Also, the presence of biochar in soils can increase their capacity of cationic and anionic exchange (UZOMA et al., 2011; ZHAO et al., 2015), due to its property of adsorbing metal ions, which is important for retaining these nutrients in the soil increasing its fertility (NOVOTNY et al., 2015). It is also worth mentioning the adsorption of pesticides and other organic compounds by biochars. This process contributes to the reduction of groundwater or nearby basins contamination and prevents these compounds from sticking into the roots of plants by biochar application. Finally, the feature of greatest interest in this thesis is the water retention capacity. Due to the porous character of biochar, there is a possible pore formation within

biochar and between biochar and soil particles. These pores could act as a water reservoir. Also, a biochar with a hydrophilic surface is more prone to retain water in soil.

1.4 Water retention on soil amended with Biochar

Some studies have shown the potential of carbonaceous materials for increasing the water retention in sandy soils (MANGRICH et al., 2015; Suliman et al., 2017). Suliman et al. (2017) recent works have reported the improvement in retention capacity in sandy soils due to the addition of pyrolytic char, with over than 100 % increase in Plant Available Water Capacity (PAWC) (LIU et al., 2017; SULIMAN et al., 2017). PAWC is the amount of water in soil that is available for plant nutrition. This quantity depends on soil texture and it considers that plants can only capillary pull water between -1.5 kPa (permanent wilting point) and -33 kPa (field capacity), except for sandy soils. In the case of sandy soils, field capacity can be higher. Mangrich et al. (2015), conducted a study in Sergipe using pyrochars prepared from local industry waste (green coconut shells, orange peel, coconut biomass used for palm oil extraction, sugar cane bagasse and water hyacinth). Their results have shown a 36 % increase in Water Holding Capacity (WHC), which can be defined as the amount of water retained by soil after complete drain divided by amount of soil used.

It has also been observed that physical characteristics of prepared biochars are primarily important for obtaining good biochar-water interaction. The tensile forces between the pore wall must be adequate in order to provide maximum water retention, while still overcoming the tension inside the pore, which would result in available water to the plant (ABEL et al., 2013; EIBISCH et al., 2015; HARDIE et al., 2014; LIU et al., 2017; MOLLINEDO et al., 2015; SULIMAN et al., 2017). So, this Thesis has aimed to produce pyro and hydrochars with highly porous texture, relying on results and literature studies. In the next section, the latest research findings related to biochar surface interactions with water will be addressed.

1.5 State of the Art in Water-Biochar Interaction

Studying the interaction of water with biochar is of primary interest to understand water retention. Several studies regarding the water behavior on soil amended with biochar have been performed on. However, little is still known about the behavior of water directly interacting with biochar.

On the other hand, studies on the interaction of water with charcoal are vast. Since the 1950s, different techniques have been introduced to examine physicochemical events associated with surface water movement and coal pores, such as dilatometry and vapor pressure isotherms (MRAW; NAAS-O'ROURKE, 1979). From the beginning, these studies have aimed the development of better drying methods for the use of charcoal as fuel (NWAKA et al., 2016; TAHMASEBI et al., 2014; YU et al., 2013). Some examples of results achieved by those works will be discussed below.

According to Yu et al. (2013), the behavior of water in charcoal depends on many factors, such as: existence of hydrogen bonds between water and charcoal molecules, if these molecules are in the form of small clusters or not, etc. According to the researchers, lower rank coals (like lignite) behave like a gel that can swell and shrink significantly (~ 30 % vol). In aqueous media, carboxyl and hydroxyl groups serve as carbon stabilizers, i.e., if removed, charcoal loses its hydrophilicity and colloidal nature. Researchers have cited the example of lignite-type charcoal (YU et al., 2013), where the interparticle pores and capillaries are saturated with water and each coal particle is surrounded by a multimolecular layer of water with a thickness of 4 to 5 water molecules. Monolayer water, which in lignite-type coals comprises only one-twentieth of the total water present, is bound to coal by hydrogen bonding to suitable polar functional groups (YU et al., 2013).

Another interesting discovery of these studies is that water, depending on how the binding to coal occurs, will behave differently. Thus, researchers have discussed "types" of water present in coal. Arisoy and Akgun (1994), for example, classified water bonded to coal as: water adsorbed by physicochemical forces, free water maintained by physico-mechanical forces, and chemically bonded water. Many researchers agree that water molecules interact with the surface of coal by hydrogen bonds with oxygen functional groups. The hydrogen bonds in water saturated coal include the hydrogens bonds that exist within coal (between H and O, N or F within biochar) and the bonds between water and coal, formed mainly with biochar carboxyl and hydroxyl groups (YU et al., 2013). Kaji et al. (1986) found a linear relationship between these hydrophilic sites and the water retention capacity of coal (KAJI et al., 1986). The relationship between the moisture content in equilibrium (coal moisture retention capacity) and the number of polar groups on the surface is due to the fact that water has a higher affinity to bind to hydrophilic surfaces (KADIOĞLU; VARAMAZ, 2003). Highly acidic carboxylic groups have been shown to be the preferred adsorption sites over the other functional groups (YU et al., 2013) .

Svabova et al. (2011) also observed that there is a linear dependence between the quantity of hydroxyl and carboxyl groups and the water absorption capacity by coal, with a high correlation coefficient (> 0.998). Considering the primary sites of coal as the oxygen-containing functional

groups sites (ŠVÁBOVÁ et al., 2011) and the secondary sites as the ones containing water already adsorbed; they found that for low relative water pressures, adsorption at the primary sites dominates, while with increasing water pressure, adsorption at the secondary sites gains significance. The percentage of adsorption at secondary sites depends on the oxygen-containing functional groups concentration, as a higher concentration of groups better supports the binding of water molecules. For coals with high oxygen content, it is easier to form water aggregates (CHARRIÈRE and BEHRA, 2010). In these studies, while increasing water vapor pressure, the authors observed that the primary and secondary adsorption sites were occupied, resulting in water condensation (YU et al., 2013).

Studies addressing the interaction of water with biochar are relatively new (BIKBULATOVA et al., 2018; BUBICI et al., 2016; CONTE et al., 2014) and the main used techniques were Fast Field Cycle Nuclear Magnetic Resonance Relaxometry (FFC-NMR), Exploratory Differential Scanning Calorimetry (DSC) and X-Ray Diffraction (XRD). The FFC-NMR technique is used to provide the values of water proton relaxation time in pores of different sizes (ANOARDO; GALLI; FERRANTE, 2001) and it was used, for example, by Conte et al. (2014), in a study about the interaction of water with the biochar pore walls. The interaction study was based on the concept of longitudinal relaxation time of water protons (NMR), interacting with pores of pyro and hydrochars. The longitudinal relaxation rates of hydrochar were substantially faster than pyrochar, so it could be inferred that biochars with larger surface area would retain more water since hydrochars had larger average surface areas than pyrochars (129 ± 2 m^2 and 54.6 ± 0.2 m^2, respectively). It was also observed that the longitudinal relaxation time of water protons reached a maximum point in the biochar pore walls, which may be associated with a temporary water adsorption at these sites by weak and unconventional hydrogen bonds. These bonds can become stronger if water molecules encounter polar groups on the surface. Although, it has been shown that the maximum points of relaxation time depend on the ratio between the pore surface and its volume, as well as the diffusion of water through the pore. In smaller pores, there will be less mobility available to water, turning hydrogen bonds more efficient. As the measured time is the time taken by the sample to reach equilibrium, it is understood that shorter times mean greater stability. In this sense, this balance can be achieved in the smaller pores as they provide stronger bonds. On the other hand, longer times are related to the difficulty of water to get into balance, suggesting its location at larger pores. But since there is an almost continuous distribution of pore size, there is also a continuous distribution of relaxation times.

It was observed that for pyrochar, larger pores than those observed for hydrochar have been reported. In their work, Conte et al. (2014) have indicated that the pores in biochar particles, which are formed by volatilization of organic groups during carbonization, are very important in water

retention. The formation of pores with hydrophilic surface occurs during thermochemical conversion processes of biomass, especially pyrolysis, due to the gasification of certain elements. Thus, these spaces are available for water storage, and the water available to plants is stored in pores large enough for the dispersion of molecular forces. Also, the chemical composition of biochar for water storage shown low significance, and pore size and size distribution are the most important factors for water retention and its release.

Bubici et al. (2016) also examined three types of biochar using NMR and Sessile Drop test. According to the applied methods, an agreement between the results for hydrophilicity under microscopical (NMR) and macroscopical (contact angle) perspectives was reached.

The DSC technique measures the difference in heat flow rate between a reference sample and a test sample under an inert atmosphere with a constant rate temperature variation (HÖHNE; HEMMINGER; FLAMMERSHEIM, 2003). In order to minimize uncertainty, the measurements were performed with similar configurations of sample and reference (or its containers) and temperature sensor. Once it is symmetrically adjusted, the furnace is heated, and the heat is transferred to sample and reference at the same rate (a temperature sensor is placed along their crucibles). A differential temperature signal is measured between both, and, if this steady-state equilibrium is disturbed by a sample transition, a differential signal, proportional to the difference between the heat flow rates of the test sample and the reference, is generated. Thus, it is useful to study the phenomena in which the sample has a change in its specific heat, or occurs heat release or absorption, such as chemical reactions and phase changes, since these events can modify the heat transfer rate capacity. For example, water specific heat is greater than for ice, so, after the solidification, there is an increase in the heat flow capacity and, during solidification, there is a disturbance between sample's and reference's heat flow rate.

DSC technique can be useful for examining water-biochar interaction, on the sense that different water storage sites internal to biochar can reveal different solidification peaks according to stronger or weaker interaction between water and biochar molecules. Also, the magnitude of the peak can be associated with the water quantity (BIKBULATOVA et al., 2018; NAKAMURA; HATAKEYAMA; HATAKEYAMA, 1981). On the other hand, the X-Ray Diffraction technique has been used at low temperatures to characterize changes in the crystalline nature of ice, and for defining the boundary between freezing and non-freezing water in coals with different pore structures.

Thus, Bikbulatova et al. (2018) performed DSC and XRD analyses on steam gasified pyrochar (pyrolysis chars were partially gasified using steam - 15 vol% balanced with nitrogen - in a vertical fixed-bed quartz reactor) moistened at different water/biochar mass ratios. In addition to

those analyzes, a water retention test was also performed. Water retention capacity and water adsorption rate demonstrated a direct correlation with the total micropore volume of pyrochar, suggesting that the physical structure of the biochar plays a key role during interaction with water. The results indicated that partial activation with steam is a promising method for biochar production suitable for soil remediation. In addition, two types of freezing water, namely freezing free water (FFW) and freezing bound water (FBW), were directly detected in the samples during DSC analysis. The presence of these two types of water was detected as the data showed two exothermic peaks on the DSC thermograms, one around -15 and one around -40 °C, indicating phase change on the water present in the pores of the biochar. The presence of non-freezing water (NFW), i.e., water present in the smallest pores with insufficient free energy for phase changing, was also confirmed in biochar, identified by the difference between the total water content of the samples and the sum of FFW and FBW. The amount of FFW showed a direct relation with the gasification degree of lignite char, with the latter leading to a more prominent formation of mesopores, suggesting that FFW is present mostly in mesopores. However, an opposite trend was observed for FBW and NFW in the biochars, indicating that those two types of water were present in the micropores.

The existence of non-freezing water in coal was induced, observing that, even though water mass was detected using a precision scale, no exothermic peaks were detected in DSC for samples with water saturation below 18 % in mass. At low temperature XRD, using different, but close, water/biochar mass ratios, it was possible to infer at which water saturation rate all water was NFW, since no peak of crystallized water was apparent. This rate is different for every sample. The presence of NFW is inducible, since lowering water content, at some point all the water was trapped in NFW sites (micropore with strongly entrapped water). It is inferred that for PAWC, meso and macropore predominant biochars are more desirable, so plant roots could win water-biochar attractive forces.

2 OBJECTIVES

General Objective:

The objective of this work is the reuse of residues from cashew industrial processing as a sustainable source for the production of carbon-based functional materials, which could be used for application as soil amendments, especially for water retention.

The specific objectives of this work are:

1. Prepare carbon-based materials through hydrothermal carbonization and pyrolysis, coupled with thermochemical activation, using cashew bagasse as feedstock;
1. Evaluate the material's structure, composition, morphology, textural and thermal properties obtained through hydrothermal carbonization and pyrolysis;
2. Evaluate the effect of thermochemical activation in material's structure, composition, morphology, textural and thermal properties;
3. Compare the effect of thermochemical activation on hydrothermal and pyrolytic chars and its water interaction;
4. Measure water retention capacity of biochars and biochars added to soil.

3 EXPERIMENTAL PART

3.1 Biomass Acquisition

The first batch of cashew was collected in 2017. The cashew used in this research was collected in Cascavel city, Ceará, and used to produce cashew bagasse. The preliminary studies were carried out using this raw material and dedicated to know how cashew bagasse behaves under different methodologies of carbonization. These studies were called Stage I of this project.

For Stage II, a new batch of cashew was collected in October 2018 at the same location of the first one. Stage II was dedicated to study how different cashew bagasse made biochars behave under the same KOH thermochemical activation parameters and how they would interact with water.

3.2 Cashew Bagasse Pretreatment and Characterization

Both batches of the produced bagasse were kept frozen, however, before drying them, they were completely defrosted. The first batch of bagasse was sun-dried for 3 days, grounded with a knife mill (Fortinox, model Star FT 50) and sifted with a 2 mm sieve. The first batch of bagasse is referred to as BC. The second batch, named BC_2, was first dried at 40 °C for 24 h according to ABNT NBR 16550 standard for sugarcane bagasse chemical characterization (sample preparation). Its ash and moisture percentages were measured before milling, also based on the ABNT NBR 16550.

To determine moisture, uncapped porcelain crucibles were washed and dried at 105 °C until constant mass and then added 1 g of bagasse. Then the set was kept in an oven at 105 °C until constant mass again. The moisture percentage was determined in triplicate, and calculated as the difference between wet and dry bagasse divided by wet bagasse mass.

The percentage of ash was determined using a muffle furnace from EDG Equipment (model 3P-S), where three lid crucibles were subjected to 575 °C for 4. Subsequently, it was added 1 g of bagasse in each and then re-submitted to 575 °C for 4 h. The ash content was determined in triplicate, and the percentage calculated as the ash mass divided by dry basis bagasse mass, According to Equation 1:

$$A = AM.100/Cma_s \quad (1)$$

where A is total ash content, AM is ash mass and Cma_s is cashew bagasse mass in dry basis.

Moisture and ash measurements for all samples (including BC and BC_2 after milling) were also measured using the TGA technique (STA 449 F3 equipment from Netzsch) under synthetic air (20 % oxygen and 80 % nitrogen) on the temperature range of 30 °C to 800 °C, and rate of 10 °C/min.

3.3 Hydrothermal Carbonization of Cashew Bagasse

For hydrothermal carbonization in the Stage I, 2 or 4 g of BC were added to 60 mL of distilled water and stirred with a magnetic stirrer for 30 min. After that, the pH was measured using a pHmeter (Quimis, model Q400AS) and the suspension was added to the stainless-steel mini bench top reactor, model 4566C, controller model 4848 from Parr Instrument Company. The sample was heated to the desired temperature (200 or 250 °C) and a residence time of 4 or 24 h was applied. The air that participated in the thermochemical process was only the air contained in the Parr reactor capsule space that was not occupied by the suspension (about 40 mL).

The obtained solid products were isolated by vacuum filtration using a Millipore® filtration system, containing Millipore porous membrane of 0.45 μm (hydrophilic PVDF) and the mother liquor pH were measured using a pHmeter (Quimis, model Q400AS). The solid product was washed with 1 L of distilled water divided in four 250 mL washes and then dried at 105 °C for 24 h.

The hydrochars prepared in this step were named CH_200_4_4, CH_200_4, CH_200_24, CH_250_4, CH_250_24 according to reaction temperature and residence time (CH_temperature_time). For the CH_200_4_4 sample, the mass in grams was added at the end of the name. All the other reactions in Stage I were performed with 2 g.

The percentage of mass recovered was calculated according to Equation 2:

$$P_r = M_c.100/(M_b(1 - I_s/100)) \quad (2)$$

where P_r is the percentage of mass recovered, M_c is the mass of hydrochar after reaction, M_b is the mass of cashew bagasse before reaction and I_s is the percentage of moisture present on bagasse.

Some carbonizations from Stage I were selected to proceed to Stage II based on the results previously obtained. So, it was decided that samples CH_200_4 and CH_250_4 would be produced in Stage II. However, the amount of raw material for each reaction was increased from 2 to 13.5 g from Stage I to Stage II to enable the activation step that had a relatively lower reaction yield.

So, in Stage II, 13.5 g of BC_2 was added to 55 mL of distilled water and stirred with a magnetic stirrer for 30 min. The pH of each suspension was measured and then these suspensions

were added to the stainless-steel reactor model 4848 from Parr Instrument Company. The suspensions were heated to the desired temperature (200 °C or 250 °C) and 4 h residence time was applied. The hydrochars prepared in this step were named CH_200 13.5 g and CH_250 13.5 g according to the reaction temperature (CH_temperature).

3.4 Pyrolysis of Cashew Bagasse

For preparation of pyrochars in the Stage I, 1 g of BC was added to alumina boats and placed in a quartz reactor in tubular furnace from EDG equipment (FT-HT series). The samples were inserted in the quartz and purged with nitrogen (N_2) gas for 30 min at room temperature. Subsequently, the ramp was set to 5 °C/min to the desired temperature (350, 450 or 550 °C) under moderate N_2 flow and residence time was set to 1.5 h. The furnace was allowed to cooling down until it reached 50 °C before removing the samples. These samples were named as CP_350, CP_450 and CP_550, according to the pyrolysis temperature (CP_Temperature). The percentage of mass recovered was calculated according to Equation 2.

The amount of raw material for each reaction was increased from 2 to 13.5 g from Stage I to Stage II to enable the activation step that had a relatively lower reaction yield.

For pyrochars prepared in the Stage II, 13.5 g of BC_2 was added alumina boats, inserted ina tubular furnace (EDG equipment, FT-HT series) and carried out the same processes as in the previous step, i.e., purge with moderate N_2 flow at room temperature for 30 min and set to ramp on 5 °C/min to the desired temperature: 350 and 550 °C for 1.5 h. The samples were named as CP_350 13.5 g and CP_550 13.5 g, according to the reaction temperature.

3.5 Biochar KOH Activation

In order to increase surface area and porosity values, a thermochemical activation process with KOH was applied. Activation temperature and biochar:KOH ratio were chosen based on previous works (HUI; ZAINI, 2015; VIEIRA et al., 2016). The aim was to choose a temperature not so low as not to enhance the increase in surface area and not so high that yield would diminish too much. Biochar:KOH ratio was chosen according to the greatest mesopore volume for Vieira et al. (2016) since there is an indication in literature that micropore cannot retain and deliver water for plants as well as bigger pores (HARDIE et al., 2014; SULIMAN et al., 2017).

The activation was made only with samples from Stage II and a 1:2 mass ratio of biochar:KOH was used. So, about 8 g of KOH (Vetec, 85 %) was added to 40 mL of distilled water and stirred with a magnetic stirrer for 10 min, and then added to 4 g of biochar and stirred for more 10 min. The mixtures were placed in an oven at 105 °C for one night to dry and macerated in the next morning. They were then placed in the tubular furnace (EDG equipment, FT-HT series) and first purged for 30 min with moderate N_2 flow. Subsequently, heated to 700 °C in a ramp of 10 °C/min under N_2 flow, with residence time of 1 h. Afterwards, the samples were allowed cool down at 105 °C before they were removed of the furnace.

Samples were then macerated and sonicated for 5 min with 50 mL of a 0.3 M HCl solution and then left under magnetic stirring for 30 min. The samples were filtered by vacuum filtration using a Millipore® filtration system, containing Millipore porous membrane of 0.45 μm of hydrophilic PVDF. The pH was measured using a pHmeter (Quimis, model Q400AS) and the process was repeated until it reached filtrate pH under 5. Then, samples were washed with distilled water, and dried using an oven at 105 °C for 24 h. After this process, the activated carbons were named as CH_200 KOH, CH_250 KOH, CP_350 KOH and CP_550 KOH according to the production process and the activation temperature.

3.6 Hydrochar and Pyrochar Characterizations

For pH measurements, all biochars were suspended at deionized water 1:20 sample:water mass ratio, agitated for 90 min and had their pH measured using a pHmeter (Quimis, model Q400AS), according to IBI-STD-2 standard for product definition and product testing for Biochar (IBI, 2015).

Carbon (C), nitrogen (N), hydrogen (H) and sulfur (S) contents were determined using an elemental analyzer (Perkin Elmer, 2400 Series II CHNS/O, USA). Oxygen content was calculated as the difference between 100 % and the sum of ashes and other element percentages (Equation 3):

$$O\% = 100\ \% - (C\% + H\% + N\% + S\% + ashes\%) \quad (3)$$

Infrared spectra were obtained in the 4000-400 cm^{-1} spectral range, under vacuum in transmittance mode with 2 cm^{-1} of resolution and 128 scans, using a Bruker equipment, model Vertex 70v. The solid samples were dispersed in KBr and pelleted.

To quantify ashes, the TGA technique was also used. The TGA curves were obtained in a STA 449 F3 equipment from Netzsch under synthetic air (20 % oxygen and 80 % nitrogen) flow of 50

mL/min on the temperature range from 30 °C to 800 °C at 10 °C/min. Alumina crucibles were used. Water content was calculated as the difference between initial percentage mass (100 %) and 130 °C percentage mass. Ash content was determined as the final mass percentage at 800 °C.

For completeness, Raman spectra were also obtained for compositional and structural analysis. The LabRam equipment from Horiba was used with a backscatter geometry, using an Argon laser line of 488 nm. Raman spectra were collected using a 600 gr/mm diffraction grating. The spectrometer spectral resolution was 2 cm^{-1}. Radiation was focused on the sample surface using an optical microscope with spatial resolution of 1 μm in diameter and a 50x objective lens (numerical aperture (NA) of 0.75 and work distance (WD) of 0.38mm). Measurements were taken at room temperature (approximately 25 °C).

Also, for structural analysis, X-ray diffractograms were obtained on a X'Pert PRO MPD diffractometer from PANalytical, UK, using CoKα radiation (λ = 1,789 Å) generated at 40 mA and 40 kV in the range from 10 to 65° (2θ). For the measurements a 0.013° step with spinner revolution time of 2 s was used. The equipment was calibrated with a LaB6 standard sample. A diffractogrma of a sample of microcrystalline cellulose from Sigma Aldrich was characterized for comparison.

Textural properties were analyzed by N_2 adsorption-desorption isotherms in a Belsorp Mini II apparatus from Belsorp, Japan. About 80 mg of the samples were degassed at 150 °C for 3 h before analysis. Specific surface areas were obtained from isotherms using the Brunauer-Emmet-Teller (BET) method. Pore volume and diameter were obtained from the Barrett-Joyner-Halenda (BJH) method.

Morphology was evaluated by Scanning Electron Microscopy (SEM) images obtained at 5 to 20 kV using a microscope manufactured by FEI, model Quanta 450 FEG. To obtain the images, all samples were crushed, sieved and the sample powders were deposited on carbon tape over aluminum sample holders and coated with gold by sputtering using an ES Quorum QT150 metallizer.

3.7 Biochar-Water Interaction Evaluation

Several experiments were performed regarding the interaction of biochar with water. First, the Sessile Drop Technique was applied using ultra-pure water. Milled biochar samples were sprayed on the surface of double-sided adhesive tapes (3M, USA) (particle size was chosen as less than 150 μm), forming a thin sample layer above the double-sided tape. After that, 10 μL drops were dripped over the sample surface and after 30 s the drops were photographed. The procedure was repeated

nine times for each sample and data was processed with ImageJ software (version XY) using Dropsnake package (STALDER et al., 2006).

Also, a water retention test was done, where 1 g of each sample was saturated with ultrapure water for 24 h in a beaker with a magnetic agitation system and then allowed to drain for 20 h on filter paper in a funnel (BIKBULATOVA et al., 2018). Samples were weighed before being saturated (M_1) and after draining (M_2), and the filter paper mass with water (M_p) was subtracted according to Equation 4. The tests were made in duplicate.

$$\text{Water Holding Capacity (WHC) (\%)} = (M_2-M_1-M_p) / M_1 \quad (4)$$

The wet filter paper mass (M_p) was estimated by applying a control for each test. During calculations the paper mass used in each sample was multiplied by the paper humidification capacity, measured in grams of water per gram of paper (acquired from the control sample). The average error of filter paper humidification capacity was estimated in triplicate on a specific experiment, being about 1 % of sample mass.

Finally, the Differential Scanning Calorimetry (DSC) experiments were performed with a Netzsch equipment, model DSC 200 F3 MAIA, a Heat Flux DSC with a Disk-Type Measuring System. The samples were saturated with ultrapure water overnight in Eppendorfs. Then, these Eppendorfs were put on a desiccator with a connection for a vacuum system. They were then vacuum dried to the desired percentage of water mass per sample mass. The percentage of water was calculated according to the Equation 5:

$$\text{Percentage of water (\%)} = (P_w - P_s - P_E)/P_s \quad (5)$$

where P_w is the mass of saturated sample and Eppendorf, P_s is the mass of dry sample and P_E is Eppendorf mass. The desired percentage of water was around 60, 80 and 100 % for each sample.

About 8 mg of each sample was then placed on an aluminum crucible with a small hole on the top and then taken to the equipment. The samples were subjected from 20 °C to -60 °C in two runs, under N_2 atmosphere, while the equipment recorded changes in the sample specific heat and compared with the reference sample which was the empty aluminum crucible. The cooling was done with liquid nitrogen at 1K/min.

3.8 Water retention of Biochar added to Soil

The soil for studies of water retention with biochar addition was taken from Cascavel city in Ceará state, Northeastern Brazil (4°07'39.6"S 38°11'02.6"W). The soil was collected from the topmost 15 cm layer in December of 2019. Granulometric composition, degree of flocculation, density, pH, electric conductivity, sum of exchangeable bases, effective cation exchange capacity (CEC), total CEC, percentage of base saturation, C and N content, assimilable Phosphor (P) tests were performed by the Soil/Water Laboratory at UFC.

For Plant Available Water Capacity (PAWC) measurements 1 % (w/w) of biochar was added to soil. In these experiments only samples from Stage II were used. The samples were prepared in in quadruplicate and agitated with a spoon. The PAWC measurements were carried out using a Richards-type extractor from Soil Moisture Equipment co, model LAB023V2. Saturated samples were placed in equipment under the pressure of −0.33 bars until they were totally drained to determine Field Capacity (amount of water after rain drainage). After that, they were placed on another Richards-type extractor under the pressure of −15 bars to determine the Permanent Wilting point (the point where plant roots cannot pull water from soil). The amount of water retained between Field Capacity and Permanent Wilting Point is the Pant Available Water for most soils. Then, weighing humid soil on those two points and subtracting one another, the PAWC can be calculated (CASSEL; NIELSEN, 1986).

4 RESULTS AND DISCUSSION

The achievements in the Stage I and Stage II will be analyzed in separate sections. For each one, samples will be discussed in terms of composition, structure, texture, morphology and other properties. In the Stage I section, hydrochars and pyrochars will be also discussed in different subsections, and then its results compared in a new subsection. Between Stage I and Stage II sections a section regarding samples carbonized using different precursor batches and masses will be addressed. Activated samples will be discussed and compared to non-activated ones in the Stage II. In the last section the interaction of Stage II samples with water and their use for soil conditioning aiming retention of water available for plants will be discussed.

4.1 Stage I - Study of Cashew Bagasse Carbonization Parameters

The chars generated in Stage I were made using the first batch of cashew bagasse. The hydrochars were made under hydrothermal carbonization at 200 and 250 °C, during 4 and 24 h, using 2 g of bagasse each batch. Only one sample was done with 4 g of bagasse, under 200 °C for 4h. Therefore, pyrochars were made under 350, 450 and 550 °C during 1.5 h using 2 g of cashew bagasse each batch. The hydrothermal carbonization will be described in subsection 4.1.1 and pyrolysis on 4.1.2.

4.1.1 Hydrochars

Results of CHNS elemental analyzes, ash and water contents determined by TGA analyzes, initial and final pH of each reaction and yield are presented in Table 2. After each reaction, the reaction media pH showed a small decrease. Probably this is due to the formation of acidic products, such as levulinic acid and formic acid, that posteriorly acted as an *in situ* catalyst promoting further glucose dehydration (resulting from cellulose and hemicellulose decomposition) into HMF (FALCO et al., 2011). Subsequently, the HMF intermediate undergoes a series of polymerization–polycondensation reactions leading to the formation of polyfuran type compounds and carbonaceous chains of hydrochar (FALCO et al., 2011)

The yield of hydrochars was more influenced by temperature rather than residence time, with hydrochars obtained at 200 °C presenting an average of 40 % of yield and those of 250 °C approximately 30 %. The initial amount of biomass also influenced yield at 200 °C, increasing the

yield from 39.54 % (2 g) to 43.45 % (4 g) as shown in Table 2. The yield results suggest that samples under hydrothermal carbonization equilibrium before reaching 4 h of reaction, and after that there are no significant changes.

It is ensured that the raw material is largely carbon (42.72 % in mass), see Table 2. However, the hydrothermal carbonizations led to an increase of this element in the final hydrochars (60 ~ 70 %). In general, the concentration of nitrogen is also observed to increase in the hydrochars with increasing temperature, although the levels of hydrogen are lower than biomass but similar between hydrochars. The levels of sulfur stayed similar for all samples (Table 2). These differences in the composition between raw material and hydrochars are due to biomass undergo some reactions under hydrothermal treatments such as hydrolysis, dehydration and biomass sugars, polysaccharides and lignin degradation reactions and condensation and elimination (WANG et al., 2018). The increase in carbon concentration was probably because of the great release of oxygen and hydrogen during dehydration reactions and decarboxylation. The hydrogen content decreases are probably due to dehydration reactions and water elimination by heating of the biomass (WANG et al., 2018). The decrease was not so big, probably due to the mild temperatures of the hydrothermal treatments. The observed increase in nitrogen concentration in hydrochars could be due to the presence of condensed nitrogen-containing heterocycles (WANG et al., 2018).

Table 2 – Results of elemental analyses, initial and final reactional pH, yields, ash and water contents for Stage I hydrochars and BC.

Sample	C (%)	H (%)	N (%)	S (%)	O* (%)	Initial pH	Final pH	Yield ** (%)	Ashes* *** (%)	Water* *** (%)
BC	42.72	6.68	2.00	1.32	36.71	-	-	-	10.57	9.04
CH_200_4_4* **	60.33	5.65	2.58	1.12	25.76	4.55	4.12	43.45	4.56	6.08
CH_200_4	65.15	5.35	2.96	1.25	18.77	4.98	3.91	39.54	6.52	4.32
CH_200_24	60.23	5.17	2.64	1.13	25.69	4.74	4.33	39.46	5.14	8.18
CH_250_4	67.59	5.21	3.07	1.14	8.77	4.75	4.29	29.32	14.22	2.77
CH_250_24	70.30	5.16	3.37	1.48	18.99	4.66	4.38	28.83	0.70	6.33

*Oxygen content calculated by the Equation (O% = 100 % - (C% + H% + N% + S% + ashes%))
**Dry basis
***The last "4" goes for 4 g, because this was the only sample done with 4 g of BC.
****Results obtained by TGA analysis.
Source: elaborated by the author.

The TGA analyzes were used to determine ash and water contents in hydrochars. The percentage of ashes seems to be similar for hydrochars obtained at 200 °C, but varies a lot for hydrochars made in 250 °C (Table 2). It appears to diminish with reaction time but this is not obvious. The dependence of water contents with reaction parameters were clearer, diminishing with temperature reaction (possibly due to increasing hydrophobicity) and increasing with residence time, like the observed by OLSZEWSKI et al. (2019).

The infrared spectra (Figure 1) showed that the BC has its main vibration bands in the region between 3700 and 2800 cm^{-1} and 1800 and 900 cm^{-1}. As it can be seen from the tentative assignment table (Table 3), the BC vibrational bands were assigned to O-H stretching mode (3312 cm^{-1}), methylene stretching (2858 and 2922 cm^{-1}), carbonyl stretching (1738 cm^{-1}), C=C modes in aromatic rings (1626 cm^{-1}) and stretching of C-O-C present in polysaccharides (1105 cm^{-1}). The observation of most of these bands suggest the presence of cellulose and hemicellulose in the bagasse. Cashew bagasse is reported to be composed by 20.56 ± 2.19 % cellulose, 10.17 ± 0.89 % hemicellulose and 35.26 ± 0.90 % lignin (CORREIA et al., 2013). However, the composition of these bagasses may vary a little among batches and species.

Analyzing the spectra of hydrochars in Figure 1, a relative increase in the intensity of the bands between 1740-1700 cm^{-1} and 1630-1580 cm^{-1} (most evidently in CH_250_4 and CH_250_24) is noted. These vibrations were attributed to stretch C=O of carboxylic acids and aromatic ring modes (C=C stretch) and C-O in aromatic rings respectively (Table 3). Also compared to BC, an intensity decrease in bands at 1110 and 1030 cm^{-1} in CH_200_4_4, CH_200_4_2 samples and CH_200_24_2 were observed. Total absence of these bands in CH_250_4 and CH_250_24 samples can also be observed. These vibrations were attributed to C-H in-plane bending C-O-C symmetrical stretch in esters, respectively (Table 3). These observations are probably a consequence of increasing temperature reaction, and further aromatization of samples.

The increase of the precursor mass from 2 to 4 g in the reaction at 200 °C did not lead to significant changes in the spectral properties of these samples. On the other hand, increasing the reaction time from 4 to 24 h in the 200 °C reaction led to a decrease in the intensity of most vibration bands indicating that main functional groups were eliminated from hydrochars, suggesting a higher level of carbonization. No significant spectral differences were noticed between spectra of the samples obtained at 250 °C for 4 and 24 h. However, they stood out from the others due to the much lower intensity of the bands around 1030 cm^{-1}, corresponding to -C-O-C bonds and the increase of the band corresponding to C=C bonds in aromatic rings, indicating a higher degree of carbonization. These assertions will be further discussed in Raman spectroscopy results. In CH_250 samples it was

also observed low intensity bands between 850 and 650 cm^{-1}, associated with C-H vibrations in aromatic rings. Also, the decrease in C-H and -C-O-C bonds can be an indicative of degradation of cellulosic matrix of biomass. XRD results also point in the direction of this hypothesis and literature reports that cellulose is decomposed at 230 °C (VOLPE et al., 2020).

Figure 1 - FT-IR spectra of hydrochars from Stage I.

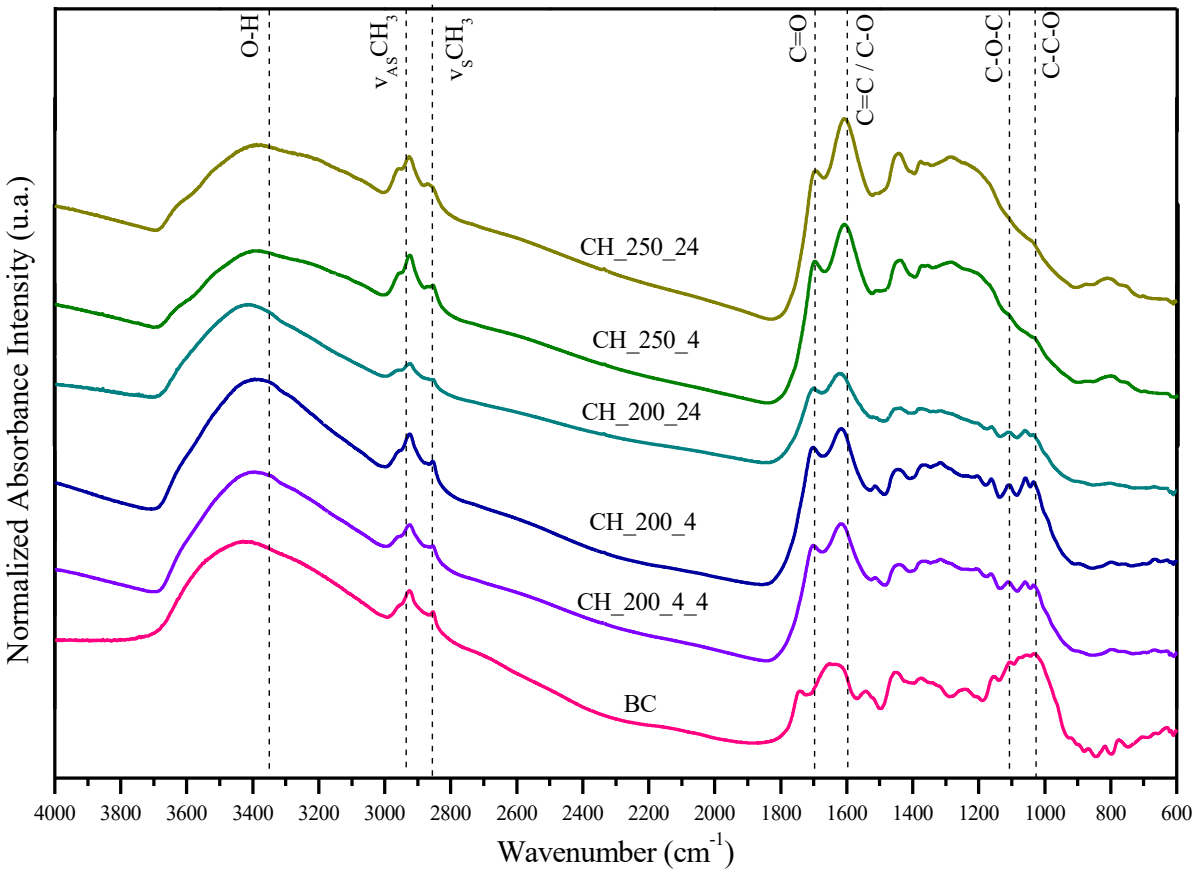

Source: Elaborated by the author.

Table 3 - Attempted attributions for the vibrational bands from FT-IR spectra in the 4000-600 cm^{-1} region.

BC (cm^{-1})	CH_200_4 (cm^{-1})	CH_200_24 (cm^{-1})	CH_250_4 (cm^{-1})	CH_250_24 (cm^{-1})	CP_350 (cm^{-1})	CP_450 (cm^{-1})	CP_550 (cm^{-1})	Attempted Attributions	References
3313	3338	3345	3437	3411	3336	3444	3425	O-H stretch in carboxylic acids, phenols and N-H stretch in amines.	(PAVIA et al., 2009; QI et al., 2016)
2962	2954	2965	2957	2962	2955	-	-	Asymmetrical stretch of (CH_3)	(LARKIN, 2011)
2925	2921	2926	2921	2925	2922	2920	2921	Asymmetrical stretch of ($v_{as}CH_2$)	(NANDA et al., 2013; PAVIA et al., 2009; PRADYOT PATNAIK, 1995; QI et al., 2016; SILVERSTEIN; WEBSTER; KIEMLE, 2005)
2852	2854	2853	2856	2895	2854	-	-	Symmetrical stretch of (v_sCH_2)	(PAVIA et al., 2009; PRADYOT PATNAIK, 1995; SILVERSTEIN; WEBSTER; KIEMLE, 2005)
1733	1707	1704	1705	1704	1696	1697	-	Stretch C=O of carboxylic acids, carboxylates, esters and ketones.	(NANDA et al., 2013; PAVIA et al., 2009; PRADYOT PATNAIK, 1995; QI et al., 2016; SILVERSTEIN; WEBSTER; KIEMLE, 2005; YU; DEHKHODA; ELLIS, 2010)
1626	1617	1609	1611	1654	1596	1586	1583	Aromatic ring modes (C = C stretch) and C-O in aromatic rings, δ deformation (H_2O).	(NANDA et al., 2013; PAVIA et al., 2009; PRADYOT PATNAIK, 1995; QI et al., 2016; SILVERSTEIN; WEBSTER; KIEMLE, 2005)
1457	1447	1446	1458	1444	1444	-	-	C-H bending in methyl groups	(PAVIA et al., 2009)
1433	-	-	1436	-	-	1433	1417	O-H bending carboxylic acid	(MERK, [s.d.])
1365	1330	1379	1370	1374	1373	1336	-	O-H bending in phenol	(PAVIA et al., 2009)
1105	1166	1105	1152	1094	-	1117	1115	C-O-C asymmetric stretching in esters	(NANDA et al., 2013; PAVIA et al., 2009; PRADYOT PATNAIK, 1995; SILVERSTEIN; WEBSTER; KIEMLE, 2005; YU; DEHKHODA; ELLIS, 2010)

Source: Elaborated by the author.

To be continued

Continuation

Table 3 - Tentative Assignments of vibrational bands from FT-IR spectra in the 4000-600 cm^{-1} region.

BC (cm^{-1})	CH_200_4 (cm^{-1})	CH_200_24 (cm^{-1})	CH_250_4 (cm^{-1})	CH_250_24 (cm^{-1})	CP_350 (cm^{-1})	CP_450 (cm^{-1})	CP_550 (cm^{-1})	Attempted Attributions	References
1047	1057	1059	-	-	-	-	-	C-H In-plane bending and/or C-O-C symmetrical stretch in polysaccharides.	(PAVIA et al., 2009; YU; DEHKHODA; ELLIS, 2010;SILVERSTEIN; WEBSTER; KIEMLE, 2005)
1011	1031	1035	-	-	1016	1012	1014	Asymmetric stretch at C-C-O bond	(PRADYOT PATNAIK, 1995)
-	-	-	798	801	-	-	-	C-H bending in aromatic rings	(CASTRO, 2018)

Source: Elaborated by the author.

Raman spectra of BC and hydrochars from Stage I (Figure 2) had their baseline taken and then they were normalized. Figure 2 shows that for BC no clear band was detected. Only fluorescence emission from the organic matrix of biomass was observable. All hydrochars presented the characteristic bands of disordered graphite, located around 1350 and 1580 cm^{-1}. The G band (1580 cm^{-1}) originates from the vibration mode that is attributed to the relative motion between two sp^2 carbon atoms (E_{2g} mode). The D band (1350 cm^{-1}) comes from the ring breathing mode (A_{1g}). The A_{1g} mode is symmetrically prohibited in perfect graphite (XING et al., 2013). It is possible to identify the effects of carbonization reactions in the hydrochars, since sp^2 carbon and ring breathing modes are not molecular structures present in the original biomass, but characteristic of carbonized material.

Figure 2 - Raman spectra of hydrochars from Stage I.

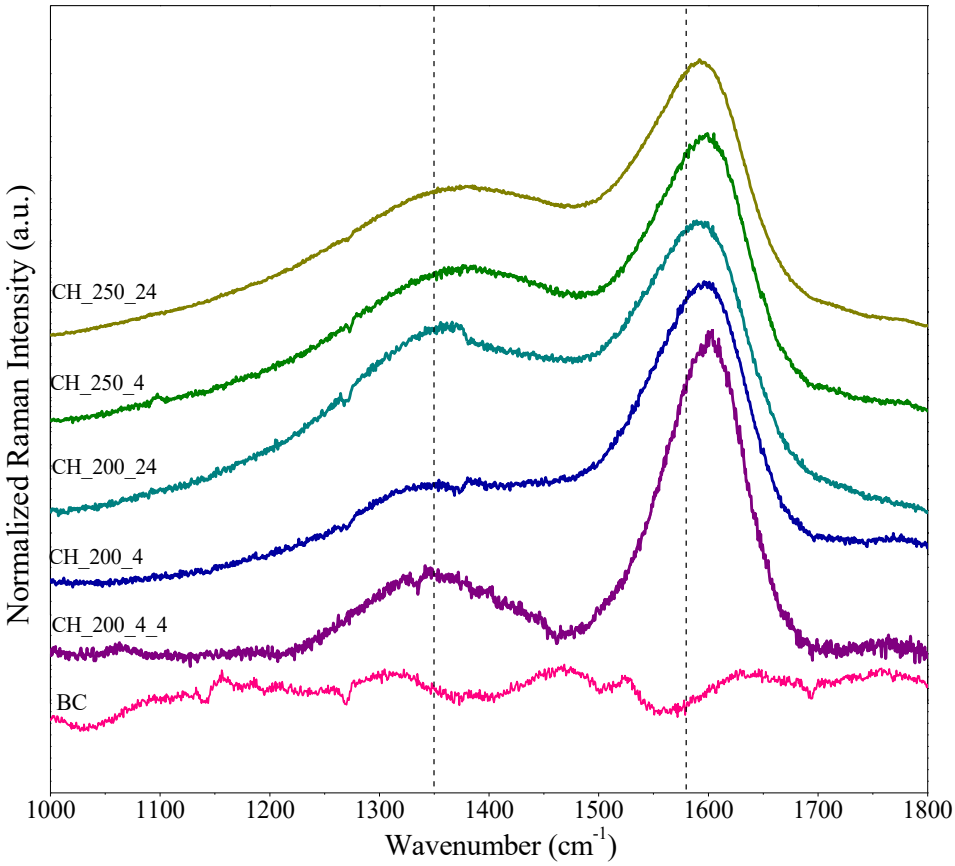

Source: Elaborated by the author.

The calculation of the relative intensities of the D and G bands are widely used in the literature because they provide information on the structural defects such as the sp^2 and sp^3 ratio and crystallite size (CASTRO, 2013; GHOSH et al., 2019). This ratio would be used to obtain structural information by comparing the biochars to each other (Table 4). However, it is noticed that there is no observable

relation between the reaction severity and the I_D/I_G ratios that range from 0.18 to 0.49. The only sample that stands out is CH_200_4, because of the very low I_D/I_G ratio. Probably it is due to the fact that the D mode is defect-induced and is used as an indicator of the degree of structural order in graphene-like materials, presenting dependence on carbonization temperature and reaction time. CH_200_4 sample was performed in mild carbonization temperature and short time of reaction, so this sample is expected to have low crystallinity (VELTRI et al., 2020). For the same reason, CH_200_4_4 sample's D and G bands were not distinguishable enough for I_D/I_G ratio calculation.

Table 4 – I_D/I_G Ratios of Stage I hydrochars.

Sample	**I_D/I_G ratio**
BC	-
CH_200_4_4	-
CH_200_4	0.18
CH_200_24	0.46
CH_250_4	0.34
CH_250_24	0.37

Source: Elaborated by the author.

The raw material, microcrystalline cellulose and Stage I hydrochars XRD patterns are shown in Figure 3 for structured studies. These measurements are important to study the structural properties of the hydrochars. The diffraction pattern of BC presents, probably, two broad peaks characteristic of cellulose superimposed to amorphous halo (CASTRO, 2018). These suggest the presence of cellulose as a constituent of the bagasse. On the other hand, for all hydrochar samples, characteristic peaks of crystalline material are absent. Only the presence of amorphous halos superimposed with large and low intensity peaks are observed, revealing that the samples are predominantly of low structural order.

Figure 3 - X-ray diffractograms (XRD) of cashew bagasse (BC), cellulose and hydrochars from Stage I.

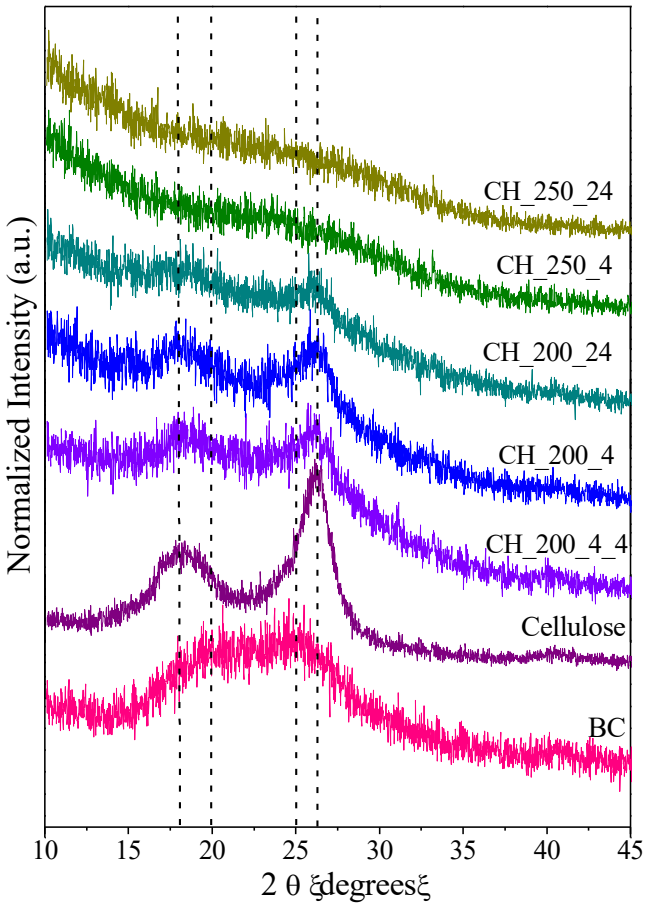

Source: Elaborated by the author.

Hydrochar samples prepared at 200 °C show peaks at 18 and 26 (2θ) superimposed to amorphous halo between 15 and 30° (2θ). These peaks are coincident to those attributed to microcrystalline cellulose (Figure 3). This observation could be assigned to thermal stability of cellulose, which decomposes at temperatures above 230 °C (CASTRO, 2018; KIM et al., 2012). Compared to BC, it is observed that there was a decrease in the intensity of the halos between 15 ° and 30 ° (2θ) after hydrothermal carbonization at 200 °C. Thermal treatment at 250 °C reduces the BC halo further, probably by destroying part of the crystalline structure, mainly associated with cellulose. The amorphous halo now is centered at 26° (2θ) suggesting that it corresponds to disorderly graphite (LEE et al., 2017).

To characterize textural properties, N_2 adsorption-desorption isotherms were done and they provided information on the sample's specific surface area, pore volume and average pore diameter,

as explained in Table 5. According to the International Union of Pure and Applied Chemistry (IUPAC), pores present in solids can be classified into three groups as to their size: micropores (less than 2 nm), mesopores (between 2 and 50 nm) and macropores (greater than 50 nm) (ROUQUEROL et al., 1994).

Table 5 – Textural properties of cashew bagasse (BC) and hydrochars from Stage I.

Sample	S_{BET}* (m^2/g)	Total Pore Volume** (cm^3/g)	Average Pore Diameter** (nm)
BC	28	0.024	2.8
CH_200_4_4	33	0.102	11.9
CH_200_4	33	0.095	11.0
CH_200_24	31	0.118	15.1
CH_250_4	36	0.082	8.6
CH_250_24	34	0.069	7.6

Source: Elaborated by the author.
*Specific surface area was calculated by BET method.
**Total Pore Volume and Average Pore Diameter was calculated by BJH method.

BC presented the relatively low specific surface area (S_{BET}) of 28 m^2/g, pore volume of 0.024 cm^3/g and the average pore diameter of 2.8 nm. It was observed that the hydrochars showed similar properties, but with a bit greater specific surface area (~ 33 m^2/g) and greater pore volume (~ 0.100 cm^3/g) than BC. Despite being larger, the surface area of hydrochars is still considered low. This behavior would be due to most particles being formed by dense carbon (KHOSHBOUY et al., 2019; WANG et al., 2019).

N_2 adsorption-desorption isotherms of the hydrochars (Figure 4) exhibit characteristics of Type II and H3 hysteresis curve (THOMMES et al., 2015). This curve profile is typical of non-porous or macroporous materials and agrees with low values for specific surface area. The isotherms shape is the result of unrestricted monolayer-multilayer adsorption up to high p/p_0. More gradual curvature is an indication of a significant amount of monolayer overlap and the onset of multilayer adsorption. The adsorbed multilayer thickness generally seems to increase monotonically when p/p_0 goes to 1. The hysteresis curve can be associated with a pore network consisting of macropores that are not completely filled with condensed gas (THOMMES et al., 2015).

Figure 4 – N_2 adsorption-desorption isotherms at 77 K for bagasse (BC) and hydrochars from Stage I.

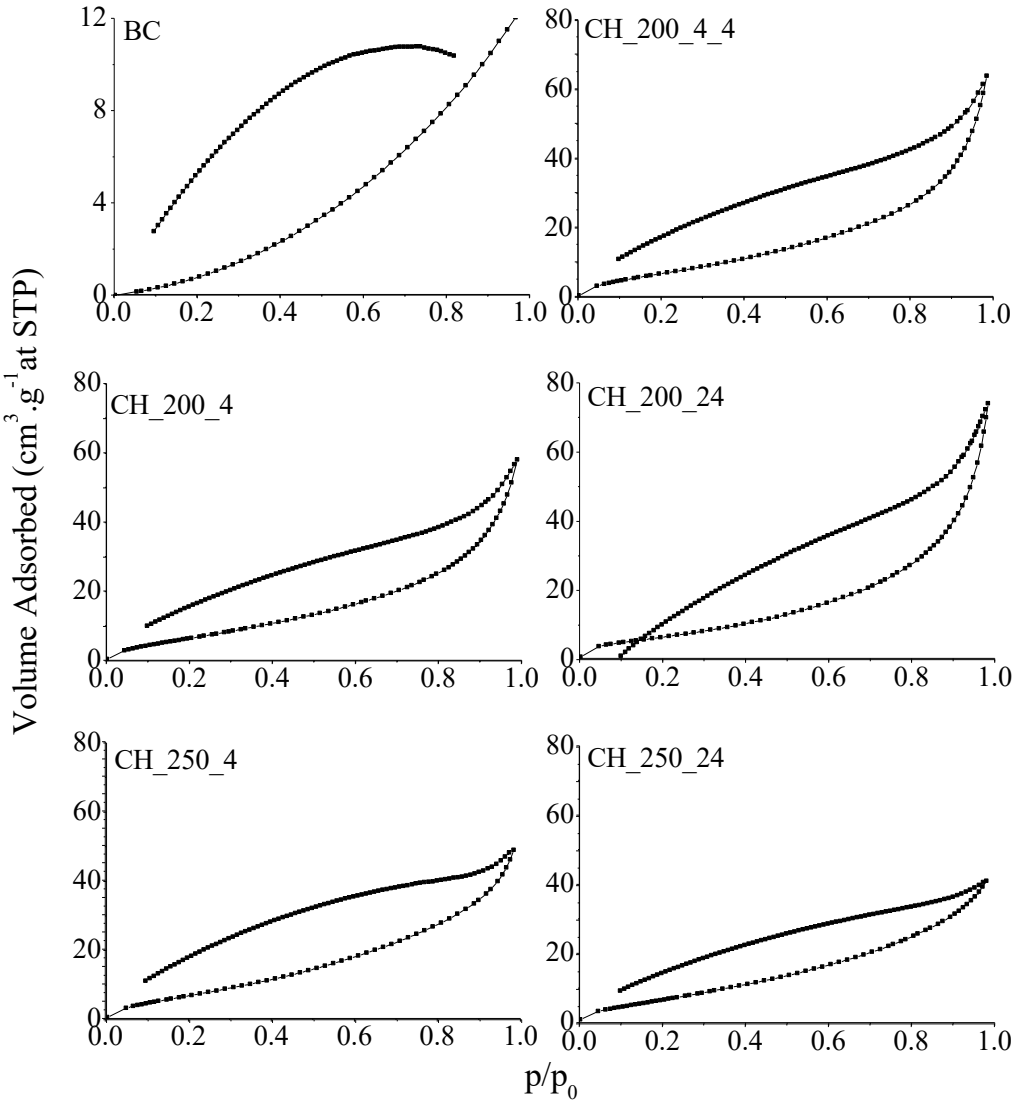

Source: Elaborated by the author.

Hydrochars Pore size distribution (Figure 5) shows that hydrochars were remarkably similar in this property, but reveal that hydrothermal carbonization developed larger pores when compared to BC.

Figure 5 - Pore size distribution obtained by BJH method of bagasse (BC) and Hydrochars from Stage I.

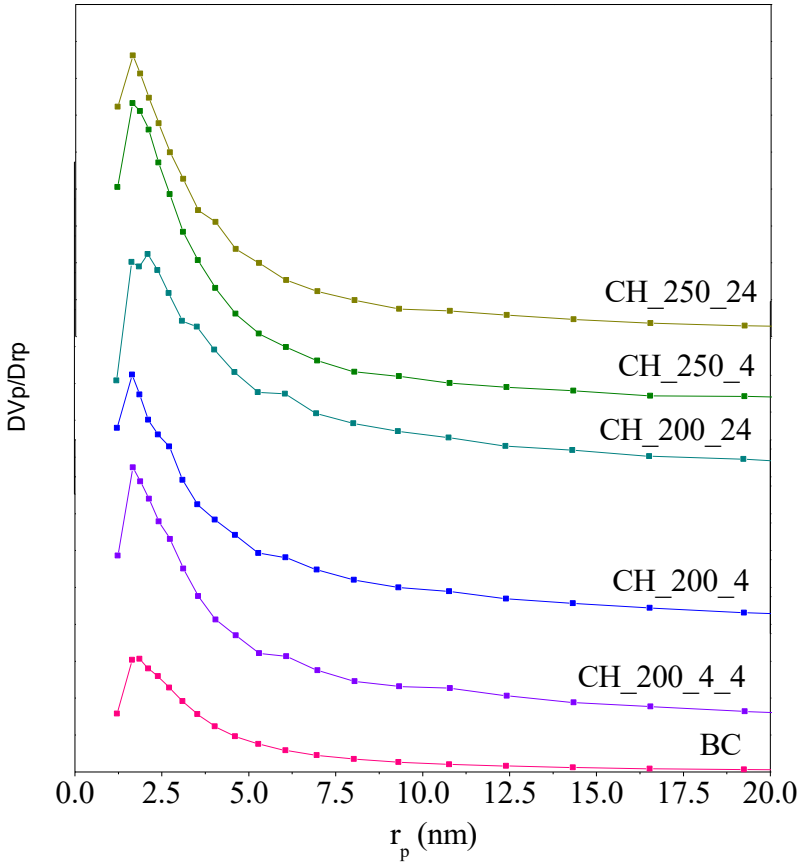

Source: Elaborated by the author.

In order to investigate morphology of the carbonaceous materials, some representative samples from Stage I were selected to be studied by SEM microscopy (Figure 6). The SEM images revealed that the hydrochars are formed by micrometer particles with different shapes, highlighting the formation of some spheres on the order of 2.5 micrometers (CH_250_4 sample). The formation of dense carbon spheres during hydrothermal carbonization is related to cellulose suffering a series of reactions to become 5-hydroxymethylfurfural (HMF) and subsequently polycondensation in carbon nanoparticles (˜3-5 nm) and then aggregating to form carbon spheres (QI et al., 2016).

Figure 6 - SEM images of three selected hydrochars produced in Stage I.

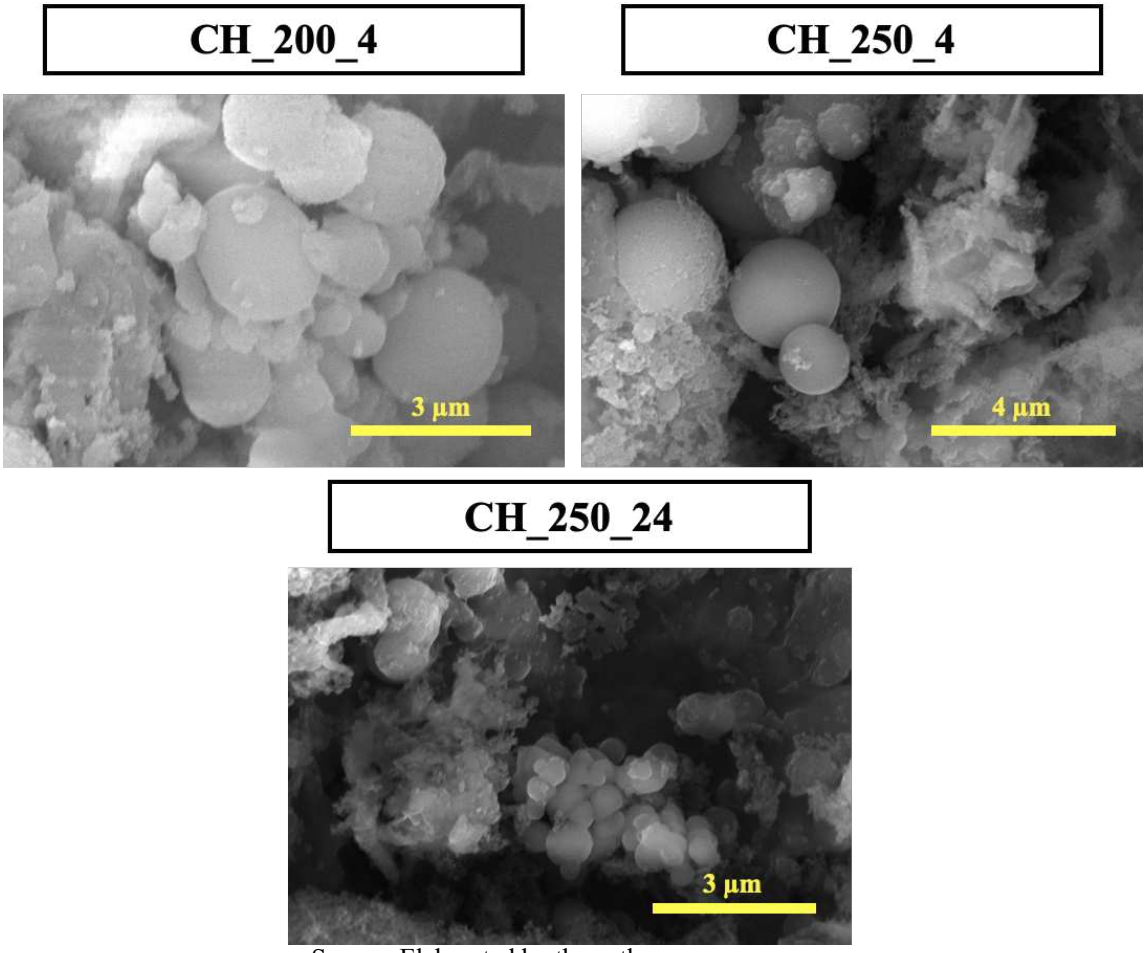

Source: Elaborated by the author.

4.1.2 Pyrochars

For pyrochars prepared in the Stage I, results of CHNS elemental analyzes, yield and ashes and water contents are presented in Table 6. Yields were inversely proportional to carbonization temperatures, ranging from 53.91 to 36.74 %, between 350 and 550 °C (Table 6). The relationship between reaction temperature and pyrolysis yield may be linked to the occurrence of dehydration reactions by the heat supplied to the sample. Therefore, higher temperatures resulted in greater sample dehydration reactions. Thus, greater would be the mass loss. Additionally, the literature shows that volatile compounds drop from biomass up to 900 °C, but between 350 and 550 °C there is the most loss of mass due to the release of these compounds (LI et al., 2005).

Pyrolytic reactions led to a carbon content in the final carbonaceous materials of 66 ~ 77 %. Compared to BC, C and N contents increased and H, S and O contents decreased. In general, as

reaction temperature increased from 350 to 550 °C, the concentrations of nitrogen and sulfur stayed stable in the pyrochars as the levels of oxygen and hydrogen decreased. This was possibly due water elimination, and detachment of volatile, oxygen-rich compounds and hydrogen, by depolymerization, dehydration and subsequent repolymerization reactions during pyrolysis (DOBELE et al., 1999). The increase in carbon content compared to BC was made possible by the fact that thermal treatment was performed in N_2 atmosphere, reducing the amount of oxygen to react with structural carbon and form gases such as CO_2 and CO. Observations on hydrogen decrease are probably due to dehydration reactions and water elimination during pyrolysis.

Table 6 – Results of CHNS elemental analyses, yields, ash and water contents for BC and Stage I pyrochars.

Sample	C (%)	H (%)	N (%)	S (%)	O* (%)	Yield** (%)	Ashes*** (%)	Water*** (%)
BC	42.72	6.68	2.00	1.32	36.71	-	10.57	9.04
CP_350	66.49	4.99	3.21	0.98	18.81	53.91	5.52	5.41
CP_450	74.53	3.96	3.25	0.78	7.82	40.17	9.66	5.55
CP_550	77.00	2.99	3.24	0.63	4.37	36.74	11.77	5.75

*Oxygen content calculated by the Equation (O% = 100 % - (C% + H% + N% + S% + ashes%))
**Dry basis
***Results obtained by TGA analysis.
Source: elaborated by the author.

Comparing the different samples of pyrochars, it is observed that while the concentrations of nitrogen (~ 3.23 %) and sulfur (~ 0.80 %) remained similar, concentrations of carbon, hydrogen and oxygen tended to vary considerably by increasing reaction temperature. It is easy to observe that CP_450 composition resembles CP_550 more than CP_350, even though the interval of reaction temperature was the same. The reduction in hydrogen concentration is expected to be due to dehydration reactions during carbonization. Also, it was observed that a lot of water condensed in the quartz tube after the end of the reaction corroborating with the suggestion aforesaid. During pyrolysis, the literature has been shown that SO_2 and COS (carbonyl sulfide) release can occur between 178 and 900 °C, which could explain the small decrease observed in sulfur content (BASSILAKIS et al., 1993).

The ash contents (results obtained by TGA analyses) tended to increase with the reaction temperature increase (Table 6). The literature points out a correspondence between final material

hydrophilicity and ash content (MAO et al., 2019). This result can be a sign that CP_550 will be more hydrophilic than the other samples due to its high ash content. Water content results for all pyrochar samples were very alike, but a little smaller when compared to BC. Meanwhile, water content in pyrochar from TGA results was probably water caught from the atmosphere after pyrolysis, as long as our samples left the reactor completely dried due to the high temperatures. That can be an indicative of pyrochar water affinity.

As can be seen in Figure 7, FT-IR spectra of pyrochars show (compared to raw biomass) a decrease in intensity of almost all bands associated to detectable functional groups. This decrease is related to the increase in the temperature of thermal treatment. Only CP_350 still had bands around 2935 cm^{-1} and 2885 cm^{-1} (attributed to methyl groups). Nevertheless, in all spectra we still see low intensity bands between 3700 and 3000 cm^{-1} (O-H stretching in carboxylic acids, phenols and N-H stretching in amines and amides) and 1600 and 1000 cm^{-1} (aromatic rings, water, methyl groups, carboxylic acids, phenols and esters). These bonds can be related to the water still present in samples (Table 6). Also, even though the measurements were performed in vacuum, some of these bands can be partly associated with the KBr present in the FT-IR measurements, especially in the frequencies at 3434 cm^{-1} and 1632 cm^{-1} (LARKIN et al., 2011).

The spectra clearly indicate the decrease in the intensity of the band associated to O-H stretching between 3500-3200 cm^{-1} as well as asymmetric (2935 cm^{-1}) and symmetrical (2885 cm^{-1}) H-C-H stretches for aliphatic methylene groups and carbonyl C=O (1700-1740 cm^{-1}) was observed. That can be an indicative of dehydration reactions (H_2O elimination). Reduction of symmetrical C-O-C stretching (1030 and 1110 cm^{-1}) was also observed. Such bands are related to precursor cellulose, hemicellulose and lignin components. However, the band around 1620 cm^{-1} (stretching vibration of C=C bonds in aromatic structure) can still be observed in the spectra, indicating the formation of aromatic moieties, as will be confirmed by Raman spectroscopy (SONIBARE; HAEGER; FOLEY, 2010).

Figure 7 - FT-IR spectra of BC and pyrochars from Step I.

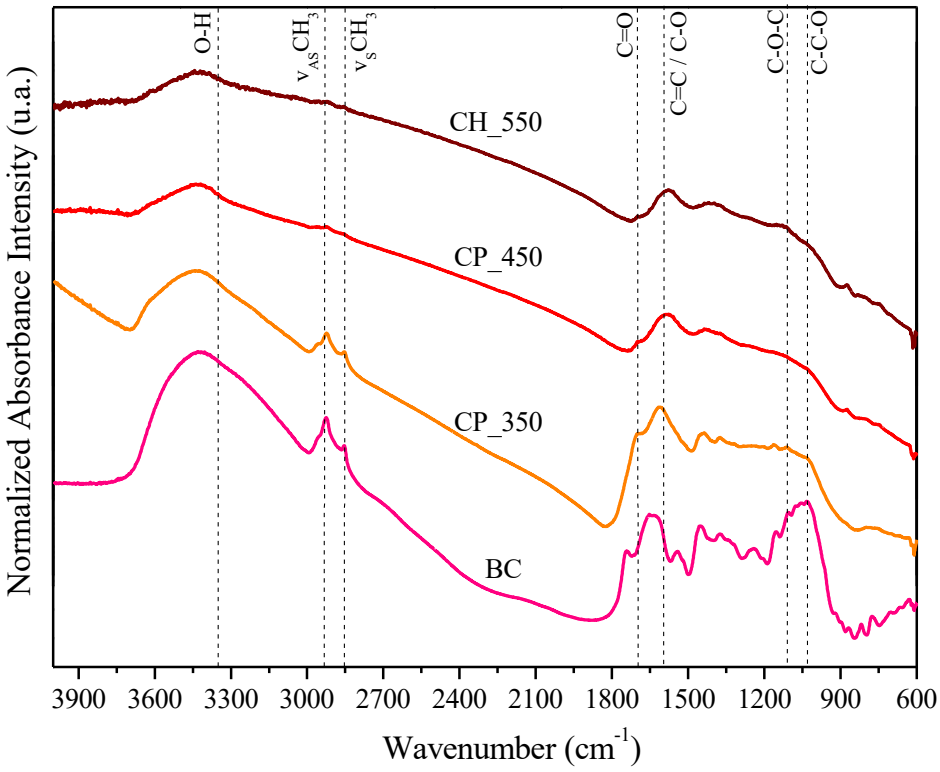

Source: Elaborated by the author.

In Raman spectra (Figure 8) it is observed that the profiles of G band are similar for all samples, but D bands are slight distinct for CP_350 sample. Raman spectra of CP_550 and CP_450 are remarkably similar. This corroborates to the assumption that the occurrence of defects in carbonaceous matrix of pyrochars increases when temperature increases (ZHAO et al., 2016). According to Huang et al. (2011), pyrolysis of biomass has four main levels divided by temperature ranges of <150 °C, 150–250 °C, 250–500 °C, and >500 °C. Where the first one refers to drying, the second to the production on some light hydrocarbons, the third to higher reaction rates and the fourth to char self-gasification. The work also reports that the temperature range between 150–500 °C shall be recognized as the pyrolysis of lignocellulose content, remaining only a small portion of lignin after that (HUANG et al., 2011). So, the increase in the intensity of D band can be observed when comparing its intensity (I_D) to the intensity of G band (I_G) through the calculation of I_D/I_G ratios (Table 7). CP_350 I_D/I_G ratio was the smallest (0.30) and CP_550 the highest (0.46) and CP_450 was closer to CP_550. This may be associated to the reactions with the lignocellulosic raw material, that leaded to the formation of grossly disordered nano crystallites with graphitic-like structure in amorphous matrix (TSANEVA et al., 2014). Corroborating that, FT-IR spectra (Figure 7) and CHNS elemental analysis (Table 6) show that a great part of H and O were eliminated. Also, condensation of small

aromatic ring structures into larger ones has been proposed by the possible mechanism for this structural evolution (KEILUWEIT et al., 2010).

Figure 8 – Raman spectra of BC and Stage I pyrochars

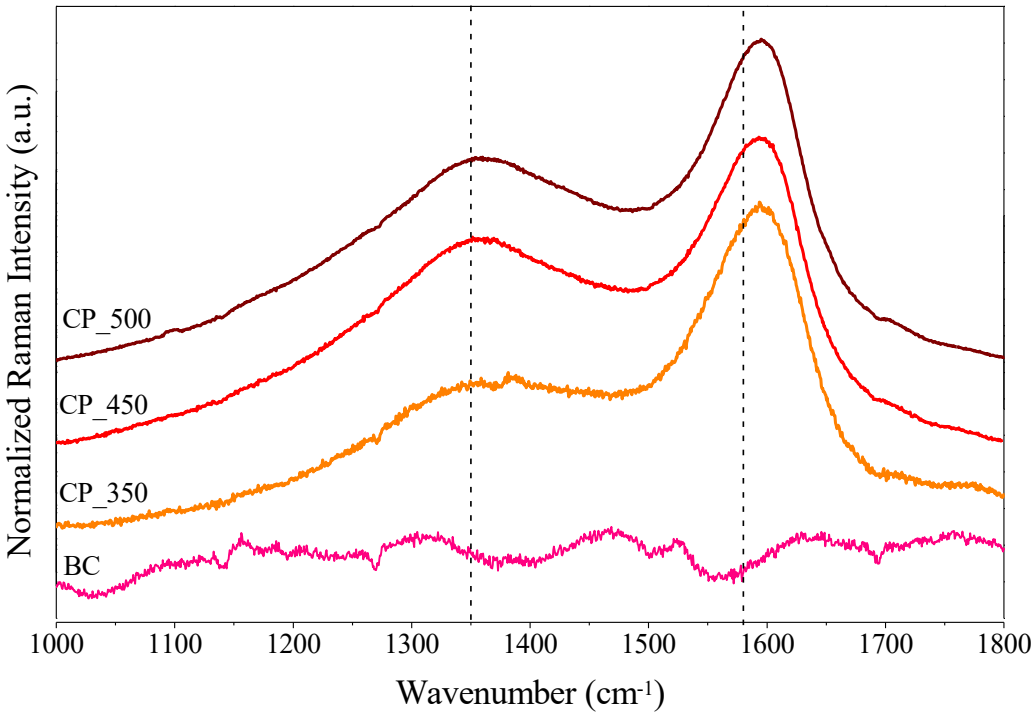

Source: Elaborated by the author.

Table 7 – I_D/I_G Ratios of Stage I pyrochars.

Sample	I_D/I_G ratio
BC	-
CP_350	0.30
CP_450	0.43
CP_550	0.46

Source: Elaborated by the author.

The diffraction patterns (XRD) for pyrochars are shown in Figure 9. The XRD pattern of CP_350 present the same profile to that of BC, showing a amorphous halo between 15 and 30° (2θ), which may be because no severe damage to the lignocellulosic structure was done up to 350 °C. At the same time, CP_450 and CP_550 amorphous halos shifted to higher angles centered at 28° (2θ) and became less intense, indicating that turbostratic crystallinity increased, as observed in hydrochars prepared at 250 °C (LEE et al., 2017).

Figure 9 - X-ray diffractograms (XRD) of cashew bagasse (BC), cellulose and pyrochars from Stage I.

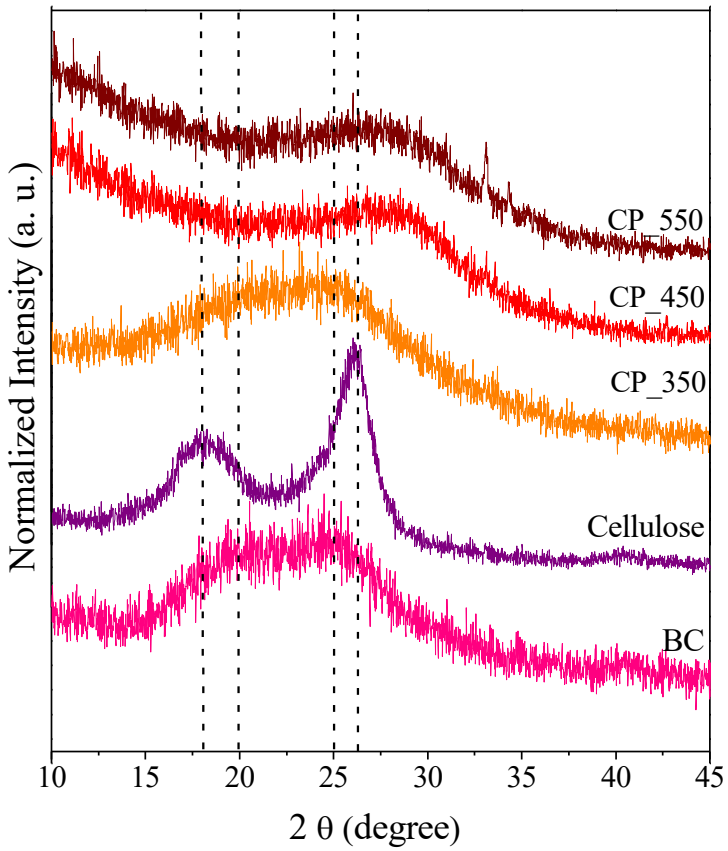

Source: Elaborated by the author.

Table 8 presents textural properties of pyrochars. It was observed a small decrease in the specific surface area (S_{BET}) of CPs compared with bagasse (from 28 to ~17 m^2/g), but it was also observed a small increase in pore volume. This result is possibly related to elimination of volatile compounds. It can be noticed that CP_550 results stood out this time, possibly because self-gasification began under 550 °C for cashew bagasse (HUANG et al., 2011).

Table 8 – Textural properties of cashew bagasse (BC) and pyrochars from Stage I.

Sample	S_{BET}* (m^2/g^{-1})	Total Pore Volume** (cm^3/g)	Average Pore Diameter** (nm)
BC	28	0.024	2.8
CP_350	17	0.031	6.0
CP_450	17	0.037	7.2
CP_550	21	0.041	6.5

Source: Elaborated by the author.
*Specific surface area is calculated by BET method.
**Total Pore Volume and Average Pore Diameter is calculated by BJH method.

The profile of the N_2 adsorption-desorption isotherms from Stage I pyrochars are very similar to BC isotherm (Figure 10). The samples present Type III adsorption curve, characteristic of materials where adsorbent-adsorbed interactions are relatively weak and adsorbed molecules are clustered around the most favorable locations on the non-porous or macro porous solid surface (THOMMES et al., 2015). But these curves have a characteristic hysteresis (H2 type) of materials where pores communicate with the surface through narrow channels. This characteristic interferes in the exit of adsorbed and condensed gases from the materials (THOMMES et al., 2015). The volume of adsorbed N_2 was similar, although the CP_550 sample presented the highest volume of adsorbed N_2 (20 cm^3/g), as can be seen in Figure 10.

Figure 10 - N_2 adsorption-desorption isotherms for cashew bagasse (BC) and pyrochars from Stage I at 77 K.

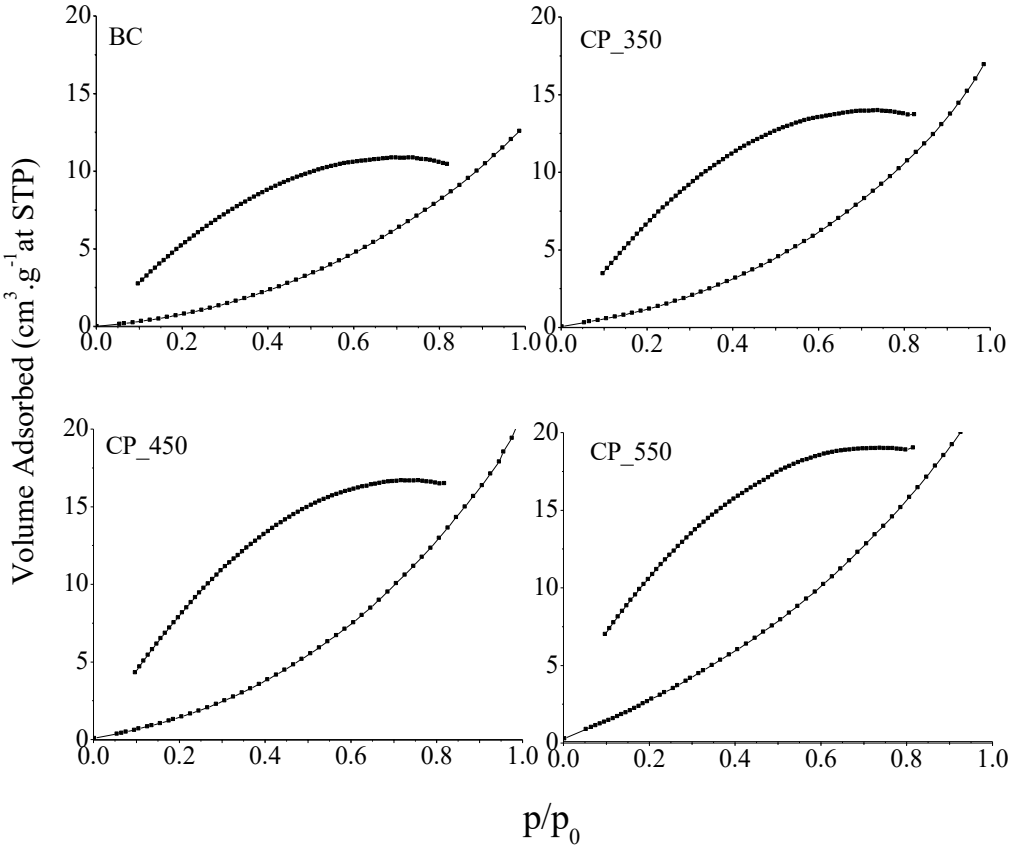

Source: Elaborated by the author.

Pyrochars Pore size distribution (Figure 11) shows that CP_350 is similar to BC in this property, but also reveals that CP_450 and CP_550 developed larger pores.

Figure 11 - Pore size distribution for cashew bagasse (BC) and pyrochars from Stage I obtained by BJH method.

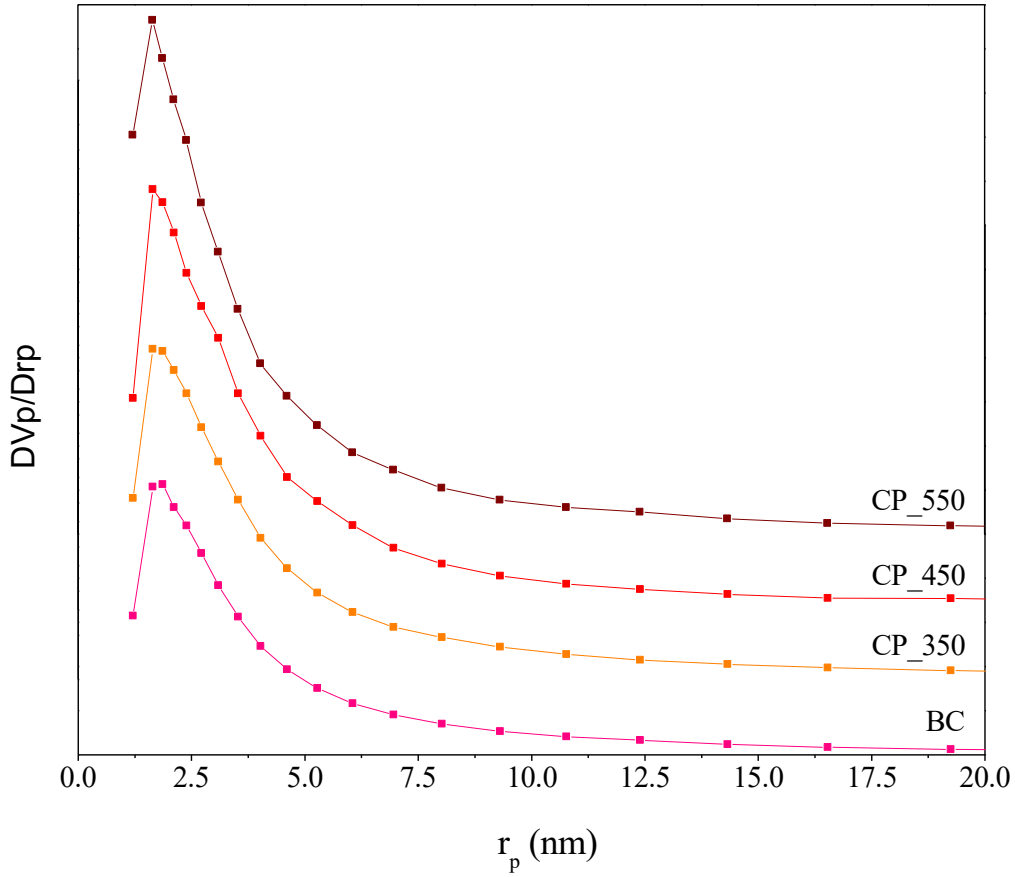

Source: Elaborated by the author.

Morphology of pyrochars were examined with SEM microscopy (Figure 12). The particles of CPs present micrometric sizes, with rough surface and with some channels and macropores, as can be seen highlighted by the arrows in Figure 12.

Figure 12 - SEM images of pyrochars from Stage I.

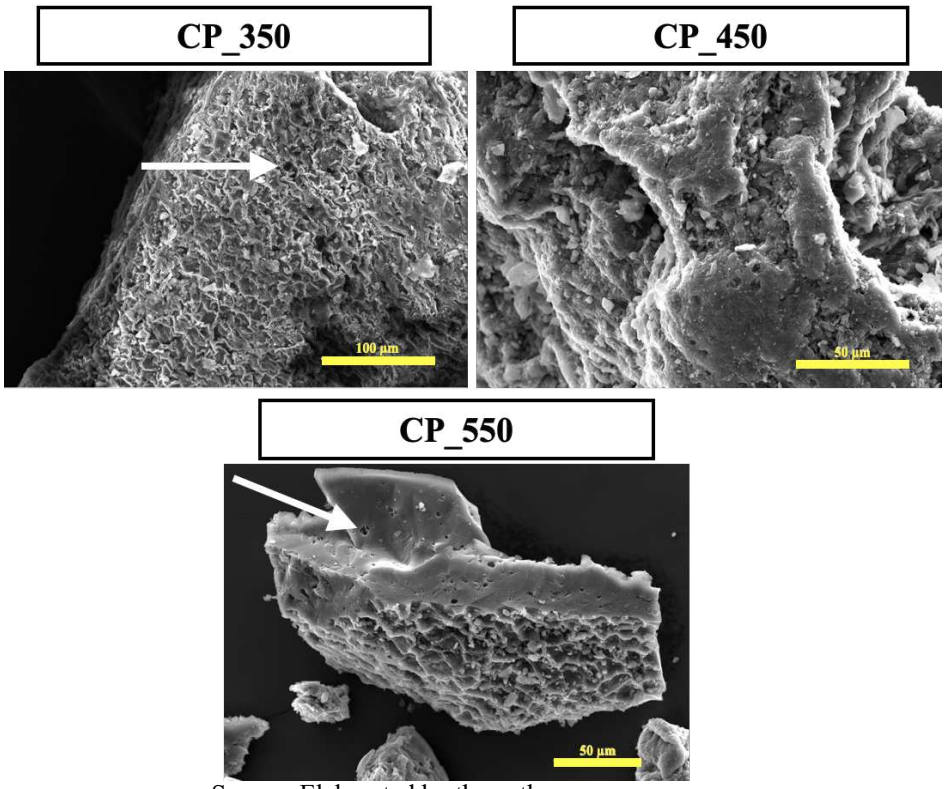

Source: Elaborated by the author.

4.1.3 Pyrolysis and Hydrothermal Carbonization: A Comparison

Although pyrolysis and hydrothermal carbonization are known for being performed in different temperatures and environments, they are done on an attempt to achieve the same goal, for example, create a soil conditioner capable to enhance soil qualities (NOVOTNY et al., 2015). The objective would be to mimetize what happened centuries ago in Amazon Forest with the formation of Terra Preta de Indio soils (TEIXEIRA et al., 2009). The choice for one or another method depends on the precursor profile and soil demands. For example, a raw material with high content of water that would demand high energy costs to dry is more indicated to hydrothermal carbonization than pyrolysis. On the other hand, somewhere short in water supply would prefer pyrolysis. Also, it would be better to add pyrochar instead of hydrochar in a more acidic soil since pyrochars have intrinsic basic pH, as can be seen on Table 9.

Table 9 – pH measurements for the samples from Stage I.

Sample	pH
BC	4.74
CH_200_4_4	4.11
CH_200_4	4.26
CH_200_24	3.74
CH_250_4	4.93
CH_250_24	4.78
CP_350	9.18
CP_450	10.43
CP_550	11.18

Source: Elaborated by the author.

Pyrochars presented higher pHs (9,18 ~ 11,18) than hydrochars (3,74 ~ 4,93) possibly due to the higher levels of organic acids of hydrochars (FANG et al., 2015). This can be due to the fact that during hydrothermal carbonization occurs the solubilization of inorganic fraction and acidic products (such as organic acid) and later they migrate from the liquid to the solid products (ZHU et al., 2015). Also, even after distilled water washing, adsorbed acidic compounds (produced by the reactions described in section 1.2.1) that remained in the final product could migrate to the aqueous phase when resuspended in water for pH measurement. Another reason is that carbon oxidation can still occur, generating carboxylic acids on the hydrochar surface, which when suspended in water could also release H^+, decreasing pH. On the other hand, regarding pH differences inside each category of biochar, samples with higher ash content seem to have higher pHs (Tables 2 and 6). This can be linked to the increasing carbonization temperature that increases the concentration of non-volatized or non-solubilized inorganic elements that can increase pyrochar and hydrochar pH (NOVAK et al., 2009).

On compositional differences, higher C and slightly higher N contents are observed on pyrochars, although lower H, S and O are also observed (Tables 2 and 6). No significant differences were observed on ash and water contents (Tables 2 and 6). Although carbonization temperature varied significantly for pyrochar from 350 to 550 °C, the yield varied only a bit more widely (36 ~ 53 %) compared to hydrochar (28 ~ 43 %), since hydrochar carbonization temperature varied only 50 °C from 200 to 250 °C. That might be related to biomass conversion by temperature and pressure, because in hydrothermal carbonization at 200 °C pressure inside the reactor was 200 psi. At 250 °C pressure shifted to 580 psi, accelerating the reactions.

According to FT-IR spectroscopies (Figures 1 and 7), hydrochars presented much more functional groups than pyrochars. Raman spectra of pyrochars reported a temperature increasing I_D/I_G ratios while hydrochars presented no obvious pattern (Tables 4 and 7). These results suggest that hydrochars were not so recalcitrant as pyrochars. On XRD measurements however, samples presented very characteristic patterns, and seemingly only samples CH_200_4_4, CH_200_4, CH_200_24 and CP_350 still showed traces of BC, such as cellulose diffraction pattern. These observations might be due to reaction temperature that was milder than the other samples, preserving part of the raw material structure. Higher temperature pyrochars tended to present an amorphous halo centered on a higher 2 θ degree, while hydrochars halo did not shift so much.

For N_2 adsorption-desorption results, specific surface area and pore volume of hydrochars were slightly higher than pyrochars, although all results were of the same order (Tables 5 and 8). Isotherms however, presented different patterns, suggesting that pyrochars bonded with N_2 weaker and only in more favorable sites, in spite hydrochars adsorbed indiscriminately in mono and multi layers.

4.2 Evaluation of Precursor Mass in the Carbonization Reactions

In order to proceed to the next step of this project it was made necessary to study more accurately the effect of precursor mass during carbonization processes. So, 13.5 g of cashew bagasse was evaluated for pyrolysis and hydrothermal carbonization. The bagasse mass was based on the volume limitation of the available pyrolysis boat. Then, for Stage II, carbonizations would be done using 13.5 g of biomass.

As seen on Stage I, increasing raw material mass on hydrothermal carbonization from 2 to 4 g induced an increase in carbonization yield (Table 2) from 39 to 43 % mass conversion. According to Guo et al. (2016), the ratio between water and biomass has a significant effect on the hydrochar yield. The researchers observed that as the ratio of biomass to water increases, hydrochar yield increases. This is consistent with other studies that have shown that the concentration of intermediate compounds in the liquid phase may increase faster and the polymerization reaction may start earlier with a higher biomass/water ratio (ÁLVAREZ-MURILLO et al., 2015; KAMBO; MINARET; DUTTA, 2018).

Table 10 provides information about CHNS elemental analyzes, ashes and water contents and yield for carbonized samples with 13.5 g and BC_2 (the second batch of cashew bagasse from Stage II). It was observed that although they were from different batches, BC and BC_2 compositions were

similar (see Table 2). Also, comparing Tables 2 (samples carbonized using 2 g) and 10, it is possible to infer that when precursor mass was changed, the solid sample did not significantly change its composition (C, N, H and S). The most expressive difference in C content (Table 2) was observed between CH_200 sample done with 2 and 4 g (4.82 %). Higher variations can be seen in ash (6 % between CH_250 2 g (Table 2) and CH_250 13.5 g (Table 10)) and consequently in O content (7.51 % between CH_250 2 g (Table 2) and CH_250 13.5 g (Table 10)). As already explained, variations in yield for hydrothermal carbonization are described in the literature and can also be observed in this work. For CH_200 sample, yield increased proportionally more when the increasing in the mass of the precursor was from 2 to 4 g (Table 2) than from 4 to 13.5 g, indicating that yield tends to stabilize when the mass of raw material increase. The highest variation of yield can be seen for samples carbonized at 250 °C (Δ = 15.23 %).

Table 10 – Results of CHNS elemental analyses, ash and water contents, initial and final reactional pH of hydrothermal carbonization and yields for biochars prepared with 13.5 g in Stage II.

Sample	C (%)	H (%)	N (%)	S (%)	O* (%)	Initial pH	Final pH	Yield ** (%)	Ash *** (%)	Water *** (%)
BC_2	41.42	7.11	1.42	1.77	40.58	-	3.93	-	7.7	6.95
CH_200 13.5 g	62.36	5.82	1.56	1.18	26.28	3.77	3.79	51.97	2.8	5.20
CH_250 13.5 g	70.1	5.38	1.99	1.12	13.21	4.08	4.02	44.55	8.2	1.44
CP_350 13.5 g	69.59	4.70	2.44	0.81	18.46	-	-	48.12	4.0	4.13
CP_550 13.5 g	78.46	3.01	2.25	0.93	4.35	-	-	34.27	11.0	4.27

*Oxygen content calculated by the Equation (O% = 100 % - (C% + H% + N% + S% + ashes%))
**dry basis
***Results obtained by TGA analysis.
Source: elaborated by the author.

For FT-IR spectra of hydrochars (Figures 1 and 13), the bands at 1700 cm^{-1} (stretching of C=O on carboxylic acids, carboxylates, esters and ketones) and 1600 cm^{-1} (C = C aromatic ring modes or water deformation δ (H_2O)), the first are stronger on 13.5 g samples than vibrations at 1600 cm^{-1}. This result indicates that 13.5 g samples are more oxidized than obtained in Stage I. For FT-IR spectra of pyrochars (Figures 7 and 13), despising differences in baseline, 2 g and 13.5 g samples have no clear difference, indicating that the same product was produced.

Figure 13 - FT-IR spectra of cashew bagasse (BC_2) and hydrochars and pyrochars produced in Stage II with 13.5 g.

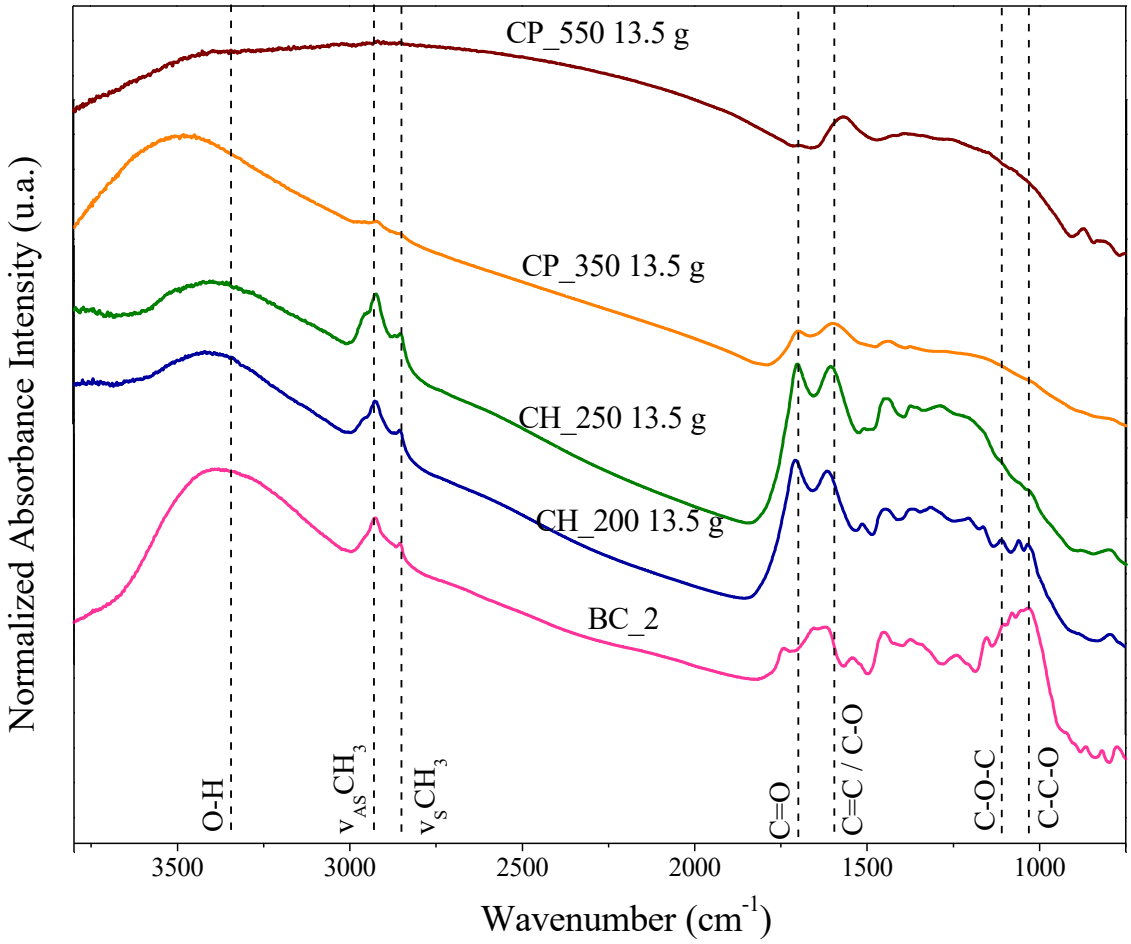

Source: Elaborated by the author.

Raman spectra show that CH_200 2 g sample presents a little less prominent D band than CH_200 13.5 g sample (Figures 2 and 14 and Tables 4 and 11). Such difference in D band between 2 g and 13.5 g samples is not observed for samples CH_250, CP_350 and CH_550 (Figures 2, 8 and 14 and Tables 4, 7 and 11). In addition, as can be seen in Figure 15, XRD diffractograms are not different for samples prepared with distinct masses. Regarding these results, no expressive difference was observed in biochar structures with mass augmentation.

Figure 14 – Raman spectra of cashew bagasse (BC_2) and hydrochars and pyrochars produced in Stage II with 13.5 g.

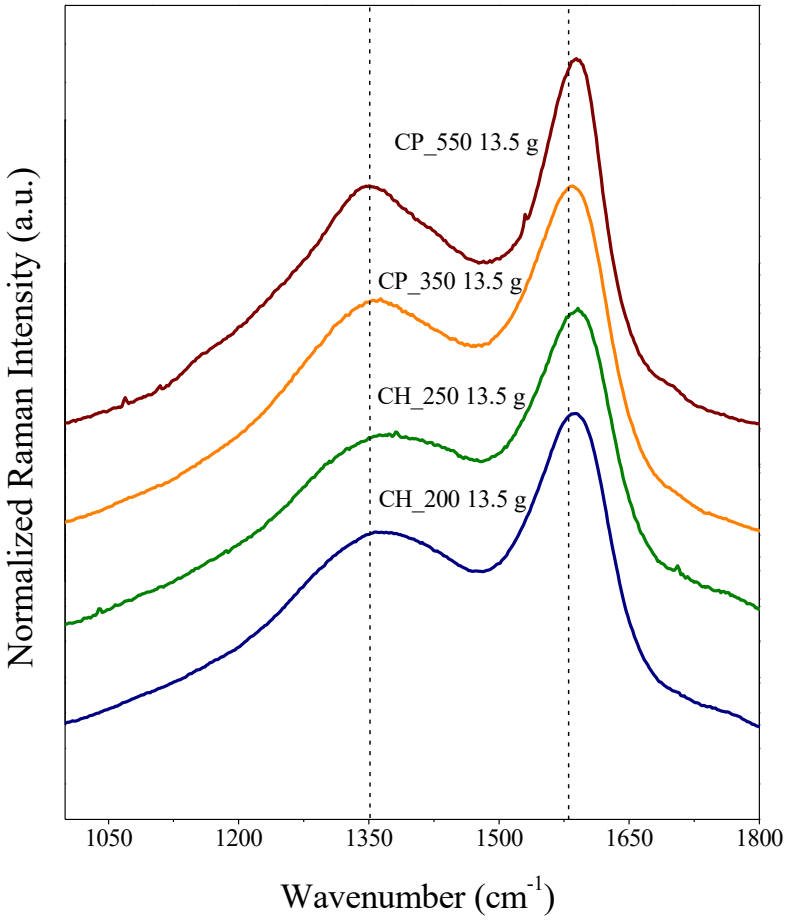

Source: Elaborated by the author

Table 11 – I_D/I_G ratios for biochars produced in Stage II with 13.5 g.

Sample	I_D/I_G ratio
BC_2	-
CH_200 13.5 g	0.36
CH_250 13.5 g	0.41
CP_350 13.5 g	0.29
CP_550 13.5 g	0.37

Source: Elaborated by the author.

Figure 15 – XRD diffractograms of cashew bagasse (BC_2), cellulose, hydrochars and pyrochars produced in Stage II with 13.5 g.

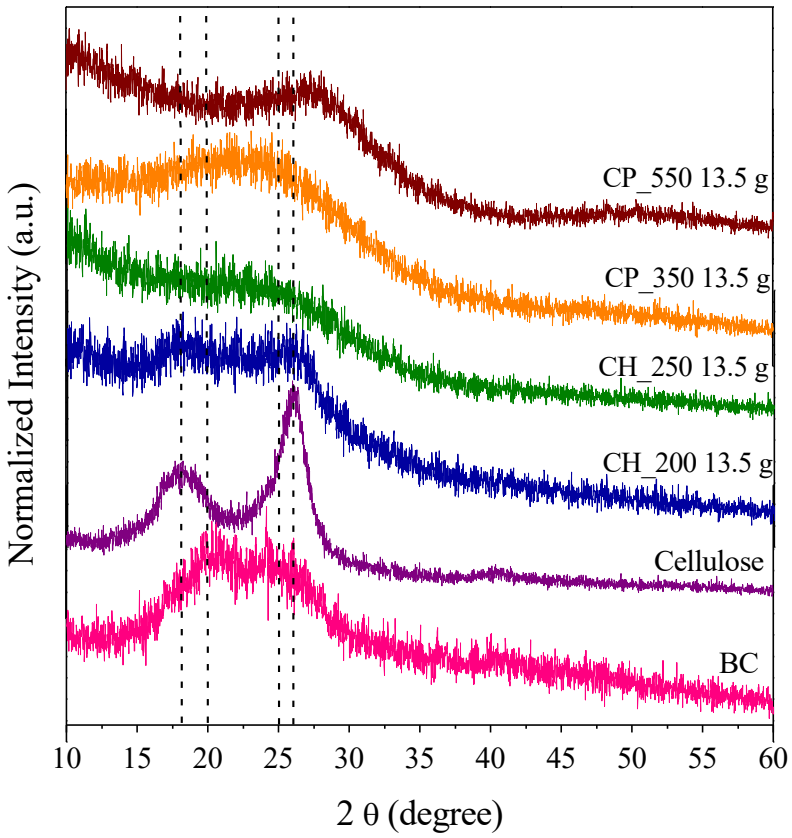

Source: Elaborated by the author.

Textural properties of Stage II biochars are described in Table 12. The results closely resemble to those obtained for Stage I samples (see Tables 5 and 8).

Table 12 – Textural Properties of cashew bagasse (BC_2) and hydrochars and pyrochars produced in Stage II with 13.5 g.

Sample	S_{BET}* (m^2/g)	Total Pore Volume** (cm^3/g)	Average Pore Diameter** (nm)
BC_2	43	0.0385	2.96
CH_200 13.5 g	33	0.0970	11.14
CH_250 13.5 g	30	0.0723	9.06
CP_350 13.5 g	16	0.0343	7.18
CP_550 13.5 g	13	0.0334	8.58

Source: Elaborated by the author.
*Specific surface area is calculated by BET method.
**Total Pore Volume and Average Pore Diameter is calculated by BJH method.

The 13.5 g samples showed N_2 adsorption-desorption isotherms with similar profiles when compared to the samples from the Stage I (Figures 4, 10 and 16). Pyrochars are similar to BC_2, presenting Type III adsorption isotherm, characteristic of materials where adsorbent-adsorbed interactions are relatively weak and adsorbed molecules are clustered around the most favorable locations on the surface of the non-porous or macro porous solid (THOMMES et al., 2015). It also has a characteristic hysteresis (H2) of materials where pores communicate with the surface through narrow channels.

Hydrochars exhibit N_2 adsorption isotherm of Type II and H3 hysteresis. This is typical of non-porous or macroporous materials (THOMMES et al., 2015) and agrees with low values for specific surface area. The isotherms shape is the result of unrestricted monolayer-multilayer adsorption up to high p/p_0. More gradual curvature is an indication of a significant amount of monolayer overlap and the onset of multilayer adsorption. The adsorbed multilayer thickness generally seems to increase monotonically when p/p_0 goes to 1. The hysteresis curve can be associated with a pore network consisting of macropores that are not completely filled with condensed gas (THOMMES et al., 2015). Also, pore size distributions are similar for samples CH_200, CH_250 and CP_350, but sample CP_550 13.5 g shows a small decrease on pores with a radius smaller than 2.5 nm when compared to CP_550 2 g (see Figures 11 and 17).

Figure 16 - N_2 adsorption-desorption isotherms for cashew bagasse (BC_2) and biochars from Stage II and cashew bagasse (BC_2) at 77 K.

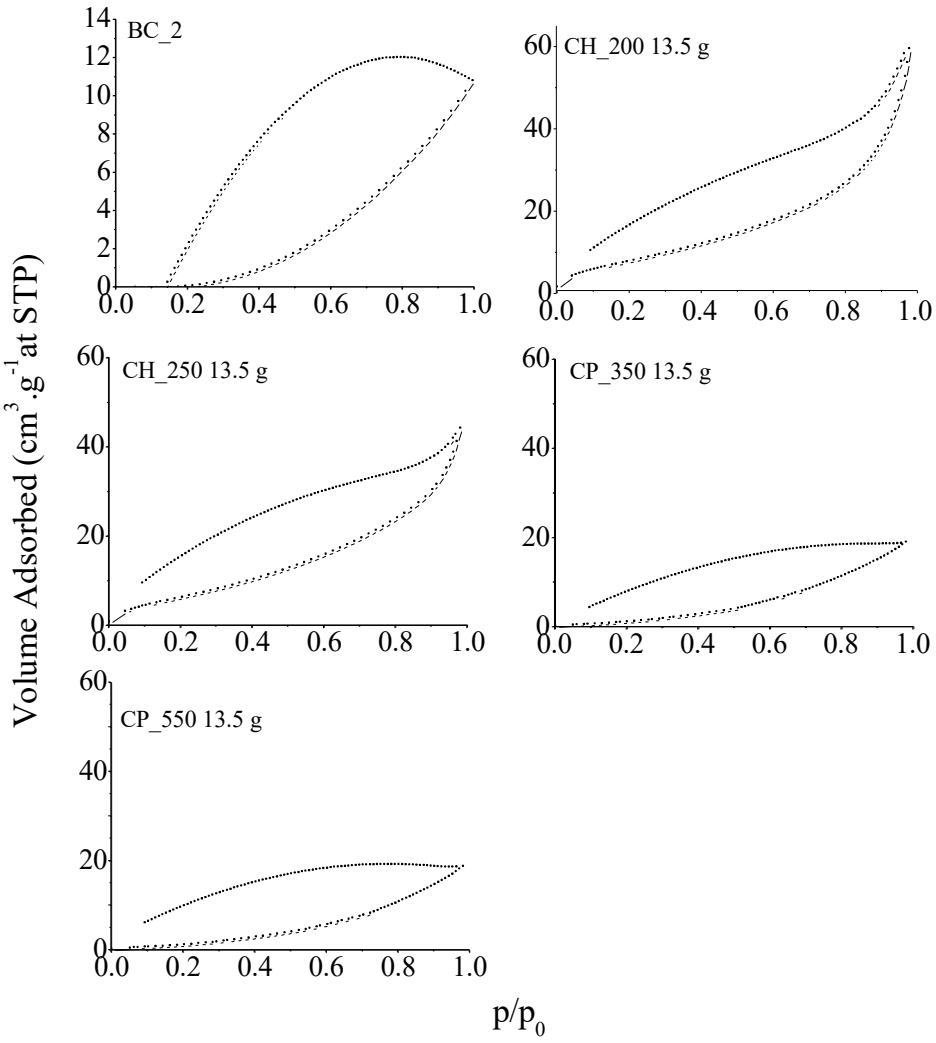

Source: Elaborated by the author.

Figure 17 – Pore size distribution for cashew bagasse (BC_2) and biochars from Stage II obtained by BJH method.

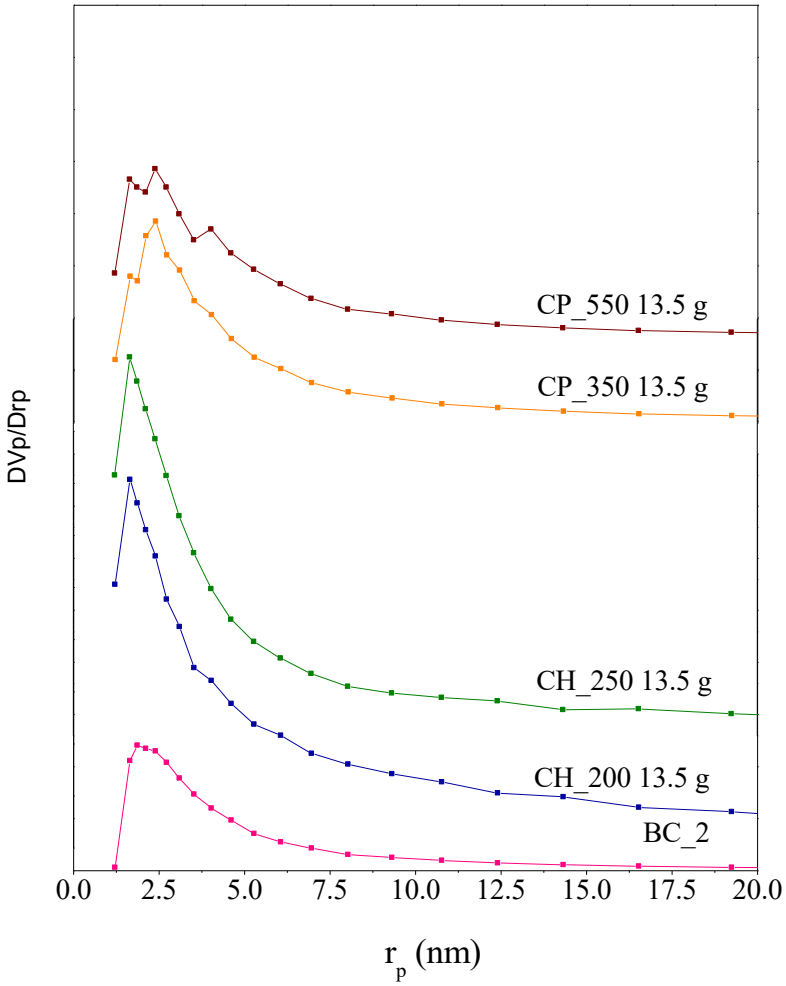

Source: Elaborated by the author.

Another result that shows the similarities between samples prepared with 2 g and 13.5 g was those obtained for pH measurements (Tables 9 and 13). This might be an indicative that temperature and reaction time are more determinant to final product pH both in pyrolysis and in hydrothermal carbonization. The same tendency of pH augmentation with increasing temperature for all samples were also observed.

Table 13 – pH results for cashew bagasse (BC_2) and biochars from Stage II.

Sample	pH
BC_2	3.93
CH_200 13.5 g	4.10
CH_250 13.5 g	5.37
CP_350 13.5 g	8.6
CP_550 13.5 g	10.26

Source: Elaborated by the author.

SEM images (Figures 6, 12 and 18) indicate no obvious differences between 2 and 13.5 g pyrochars. However, there was no formation of carbon spheres for 13.5 g samples, inspite of what was observed for hydrochar samples obtained with 2 g. Sphere formation can be understood in the context of carbonization severity, where furfurals polymerize and generate carbon microspheres with extending reaction time and increasing temperature (Lei et al., 2016; Liu et al., 2017). On lower water:biochar ratio, furfural polymerization was probably inhibited with the increase in concentration of intermediate compounds in the liquid phase (GUO et al., 2016). Also, according to Jain et al. (2016), higher reactant-to-water ratio leads to polymerization at comparatively shorter residence times, but at the same time leaves most of the reactant unhydrolyzed (JAIN; BALASUBRAMANIAN; SRINIVASAN, 2016). Likewise, Sevilla et al. (2009) observed in the case of higher concentration of biomass, smaller microsphere formation because of less extensive hydrolysis at higher substrate concentrations (less water), so most of the dissolved products might have not undergone condensation and thus lead to smaller sized spheres.

Figure 18 – SEM images of cashew bagasse (BC_2) and hydrochars and pyrochars produced in Stage II with 13.5 g.

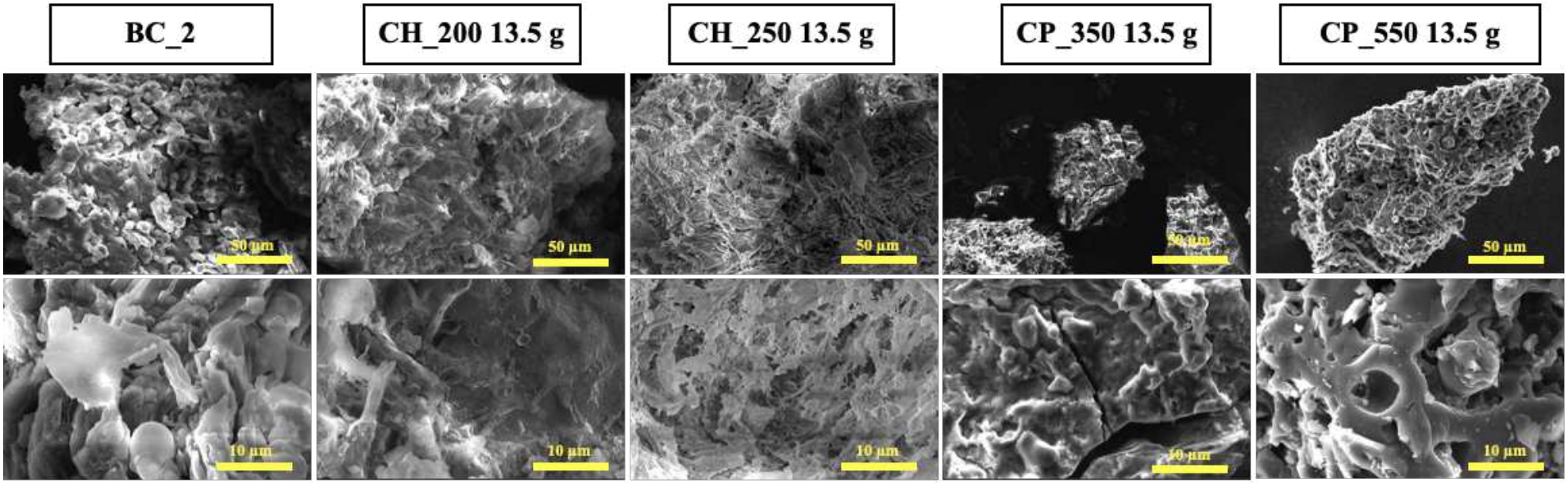

Source: Elaborated by the author.

Ultimately, augmentation in precursor mass in pyrolysis had no significant influence in final products. On the other hand, regarding hydrothermal carbonization, this augmentation was enough to prevent sphere formation and boost yield on final products. Nevertheless, composition and structure were not significantly affected in hydrothermal carbonization.

4.3 Stage II – Thermochemical Activation of Cashew Bagasse Biochars

For the step of thermochemical activation were used the CH_200 13.5 g, CH_250 13.5 g, CP_350 13.5 g and CP_550 13.5 g samples produced in Stage II. In this section, samples CH_200 13.5 g, CH_250 13.5 g, CP_350 13.5 g and CP_550 13.5 g will be simply addressed as CH_200, CH_250, CP_350 and CP_550, respectively, i.e the precursor samples were renominated before thermochemical activation.

The CHNS elemental analyzes, ashes and water contents and yield for the solid materials after the activation process with KOH at 700 ºC are presented in Table 14. The activated biochars had similar yields of 13.91, 14.35 and 15.70 % for CP_350 KOH, CH_200 KOH and CH_250 KOH, respectively (Table 14). An exception was observed for CP_550 KOH that presented yield of 23.50 %. Probably, the yield of this sample is higher because the precursor biochar was carbonized at the closest temperature to 700 °C among the samples. So, a higher carbonization degree took place, and the biochar underwent self-gasification. From 550 to 700 °C, less organic matter was carbonized compared to the other samples.

For all activated biochars it was noticed that their compositions are very close to each other (Table 14). In general, they presented growth in carbon content compared to non-activated biochars (see Table 10), having on average of 70 % of their mass in carbon. Also, samples presenting a decrease in the contents of hydrogen and nitrogen. CHs had greater hydrogen reduction than CPs after activation, probably because they had higher H contents and this element would be eliminated as H_2O and low weight molecules due to high temperature. On the other hand, CPs had greater nitrogen reduction. The only sample that showed a decrease in carbon content was CP_550, probably because it had a higher C content and more reactions occurred with KOH releasing carbon as carbon monoxide and dioxide (WANG; KASKEL, 2012). The observed compositional changes may be associated with the reactions that occurred under the thermochemical activation (at 700 °C) leading to an increase in the degree of carbonization. Jin et al. (2014), pointed out that KOH activation increased carbon and oxygen content, but not polarity since O-H groups were eliminated and the C/O ratio remained constant (JIN et al., 2014).

Table 14 – Results of CHNS elemental analyses, ash and water contents and yields for thermochemical activated biochars treated with KOH at 700 °C.

Sample	C (%)	H (%)	N (%)	S (%)	O* (%)	Yield** (%)	Ashes*** (%)	Water*** (%)
CH_200 KOH	70.81	2.82	1.5	0.85	21.02	14.35	3.0	19.90
CH_250 KOH	70.99	2.44	1.44	0.78	18.85	15.70	5.5	19.10
CP_350 KOH	67.94	3.05	0.76	1.08	21.97	13.91	5.2	25.10
CP_550 KOH	71.63	3.1	0.67	0.76	12.84	23.50	11.0	21.07

*Oxygen content calculated by the Equation (O% = 100 % - (C% + H% + N% + S% + ashes%))
**dry basis
***Results obtained by TGA analysis.
Source: elaborated by the author.

From TGA results, high water contents were observed in the activated samples when compared to non-activated ones (Tables 10 and 14). This can be a strong indicator of water affinity, since samples were completely dried after activation and immediately stored in glass bottles away from humidity, like all other samples. Even doing so, activated samples possibly adsorbed part of atmosphere water.

Figure 19 presents Van Krevelen diagram of samples from Stage II. It maps the relation between H/C and O/C atomic ratios and correlates them with those known in several types of charcoal (peat, lignite, coal and anthracite) or biomass. This diagram is presented here so that the reader can recap all the discussed achievements. Now, samples that underwent distinct processes can be compared to each other and to carbonaceous materials that are found in nature.

Under this light, BC_2 had a little higher H/C ratio than the original biomass area, indicating a higher presence of hydrogen than usually observed for biomasses. Also, CH_200 sample was more related to peat, a soft organic material consisting of partly degraded plants and, in some cases, deposited mineral matter (USGS, 2020). It was observed that this was probably because CH_200 was the less severe carbonization. Hydrochar samples moved away from BC_2 on the diagram on the path of dehydrogenation, demethylation and dehydration, just like pyrochar samples, but stayed closer to BC_2. CH_250 and CP_350 stayed close each other on the diagram, between lignite (the lowest grade coal with the least concentration of carbon) and coal (a middle rank coal between lignite and anthracite, with a high heating value and very discrete layer formation) (USGS, 2020). Pyrochar samples moved further in the direction of smaller H/C and O/C ratio, presenting more severe dehydration. CP_550 and activated samples were more related to coal, close to anthracite, probably due to the high severity reaction they underwent. These samples have a closer H/C ratios, although a little more diversified O/C ratio. In the case of CP_350 KOH sample, O/C ratio stood out. It presented

the highest O/C ratio among activated samples although this atomic ratio for CP_350 was closer to CH_250 sample before activation. This can be an indicative of higher demethylation.

Figure 19 -Van Krevelen Diagram for biochars produced in Stage II using 13.5 g of cashew bagasse (BC) and KOH activated biochar prepared at 700 °C.

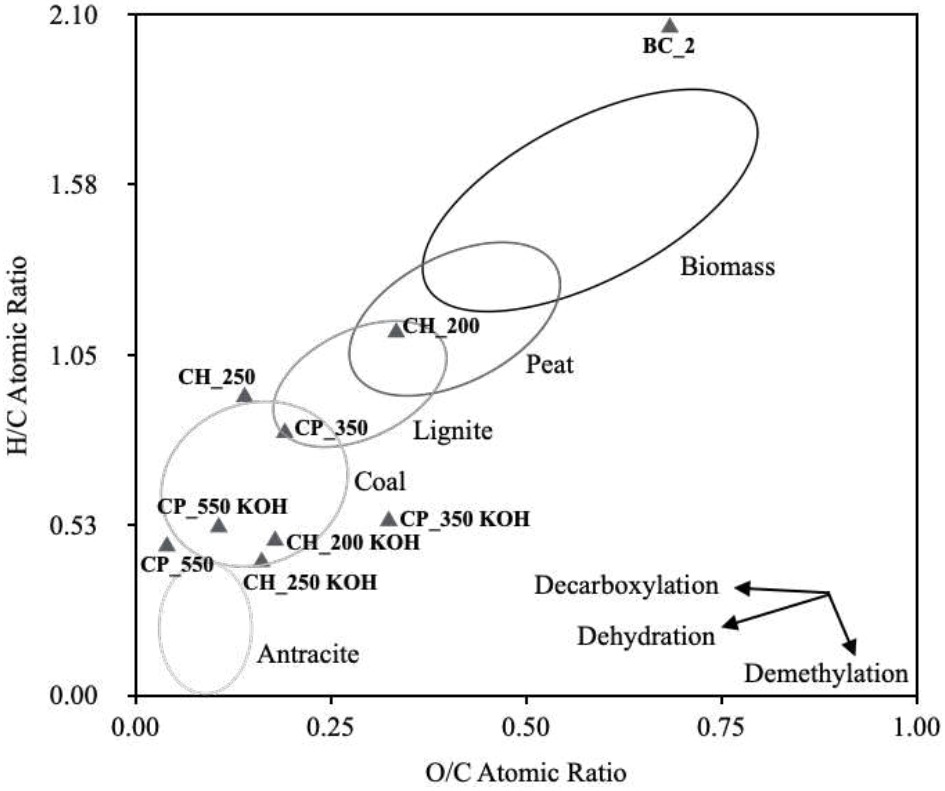

Source: elaborated by the author.

The infrared spectra of activated biochars are shown in Figure 20. It is noticed that all activated biochars have very similar spectral profiles with few and weak absorption bands, suggesting that functional groups were almost completely eliminated and the remaining groups are inactive in the infrared spectroscopy. The bands still observed at 3434 and 1632 cm^{-1} can be related to water absorbed on KBr involved in the FTIR analysis (LARKIN, 2011).

Figure 20 - FT-IR spectra of the KOH activated biochars at 700 °C.

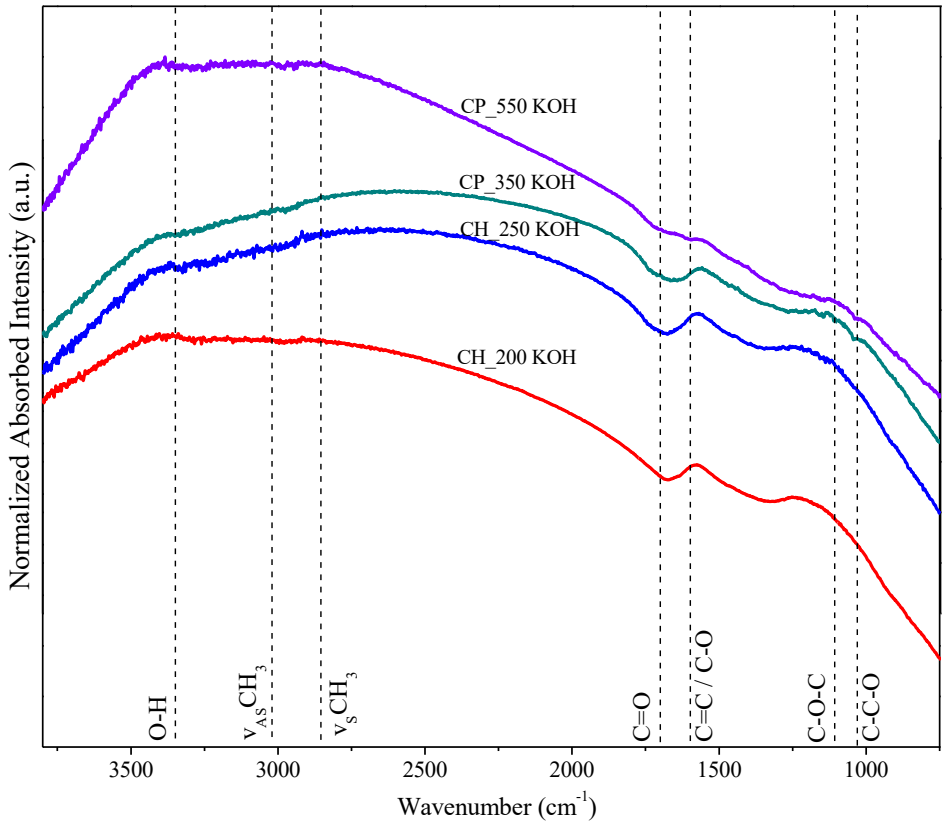

Source: elaborated by the author.

The Raman spectra of the activated samples are shown in Figure 21. The same bands centered around 1350 and 1580 cm^{-1} attributed to D and G vibrational bands, respectively, of graphitic structure are observed for all activated samples (Figure 21). There is great similarity between activated biochar spectra, in agreement with the absorption spectra in the infrared region, suggesting that all samples have similar structure.

Table 15 shows the I_D/I_G ratios for activated biochars. It is noticeable that the ratio of intensities of D and G bands are higher for activated carbons (~ 0.8), compared to non-activated carbons (~ 0.35) (Tables 11 and 15). This result indicates greater structural disorganization, which might be caused by the greater reaction temperature, generating disordered graphitic moieties (AKBAR; GÜNGÖR, 2014; VELTRI et al., 2020).

Figure 21 - Raman spectra of activated biochar produced by KOH activation at 700 °C.

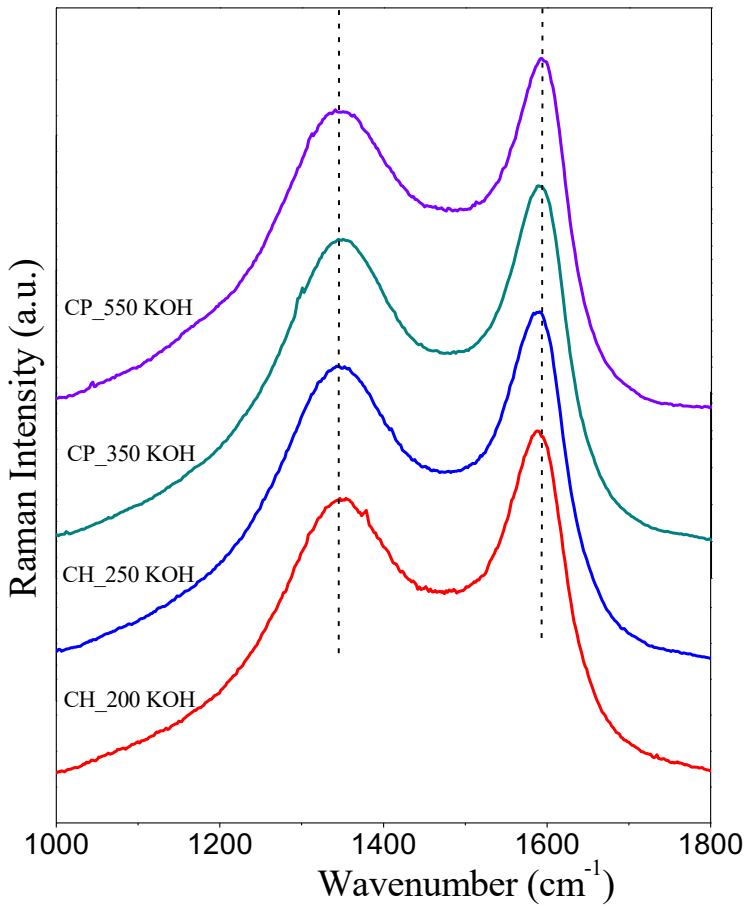

Source: Elaborated by the author.

Table 15 – I_D/I_G ratios of activated biochars produced by KOH activation at 700 °C.

Sample	I_D/I_G ratio
CH_200 KOH	0.72
CH_250 KOH	0.82
CP_350 KOH	0.85
CP_550 KOH	0.78

Source: Elaborated by the author.

Similarly, analyzing diffractograms of activated samples (Figure 22), it is observed that the amorphous halos became even less apparent compared to non-activated samples (Figure 15). However, all activated carbons still have a low intensity halo centered around 28° (2 θ), with CP_550 KOH being the sample with the least apparent halo.

Figure 22 - X-ray diffractograms (XRD) of activated biochars produced by KOH activation at 700 °C.

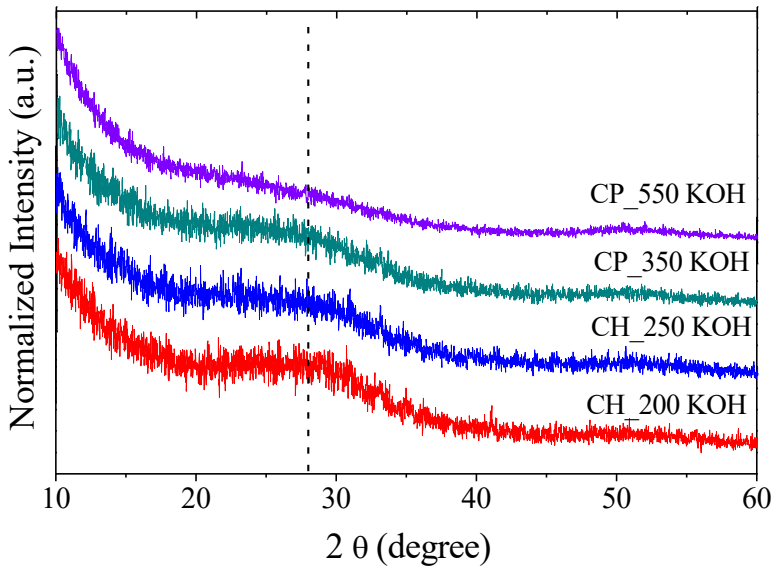

Source: Elaborated by the author.

Textural properties are shown in Table 16. A large increase was observed in specific surface area (S_{BET}) for activated samples that went from 33, 30, 16 and 13 m^2/g to 639, 598, 847 and 783 m^2/g for CH_200, CH_250, CP_350 and CP_550, respectively. The increase in pore volume was not as expressive, but pore volume for pyrochars was about 3 times bigger after activation. Average pore diameter decreased, as has been observed in other KOH activation studies (WU et al., 2010). All of those were expected since KOH activation is extensively used for micropore formation. Micropores and mesopores are formed due to the intercalation of potassium into the carbon network during the activation process (HUI et al., 2015). The micropores may collapse to form mesopores and eventually macropores if the activation temperature and time are further increased to temperatures higher than 800 °C, which may result in both lower surface area and carbon yield (HUI et al., 2015).

Table 16 – Textural Properties of activated biochars produced by KOH activation at 700 °C.

Sample	S_{BET}* (m^2/g)	Total Pore Volume ** (cm^3/g)	Average Pore Diameter ** (nm)
CH_200 KOH	639	0.115	3.2
CH_250 KOH	598	0.113	3.2
CP_350 KOH	847	0.110	3.0
CP_550 KOH	783	0.094	3.0

Source: Elaborated by the author.
* Specific surface area is calculated by BET method.
** Total Pore Volume and Average Pore Diameter are calculated by BJH method.

Activated samples showed Type I (a) isotherms (Figure 23), characteristic of microporous solids with relatively small external surfaces (e.g. some activated carbons, molecular size zeolites and certain porous oxides) (THOMMES et al., 2015). For nitrogen and argon adsorption at 77 K and 87 K, type I (a) isotherms are given by microporous materials with mainly narrow micropores (width <± 1 nm). Activated samples also showed H4 hysteresis type, where the more pronounced uptake at small p/p_0 ratio is associated with the filling of micropores. H4 loops are often found with micro-mesoporous carbons (THOMMES et al., 2015). A very abrupt uptake of N_2 at low p/p_0 is due to a high number of adsorbate-adsorbent interaction sites in narrow micropores (micropores of molecular size), resulting in micropores being filled in small p/p_0 ratio. Hysteresis curves can mean slightly narrower pore channels (THOMMES et al., 2015).

Figure 23 - N_2 adsorption-desorption isotherms at 77 K for KOH activated samples.

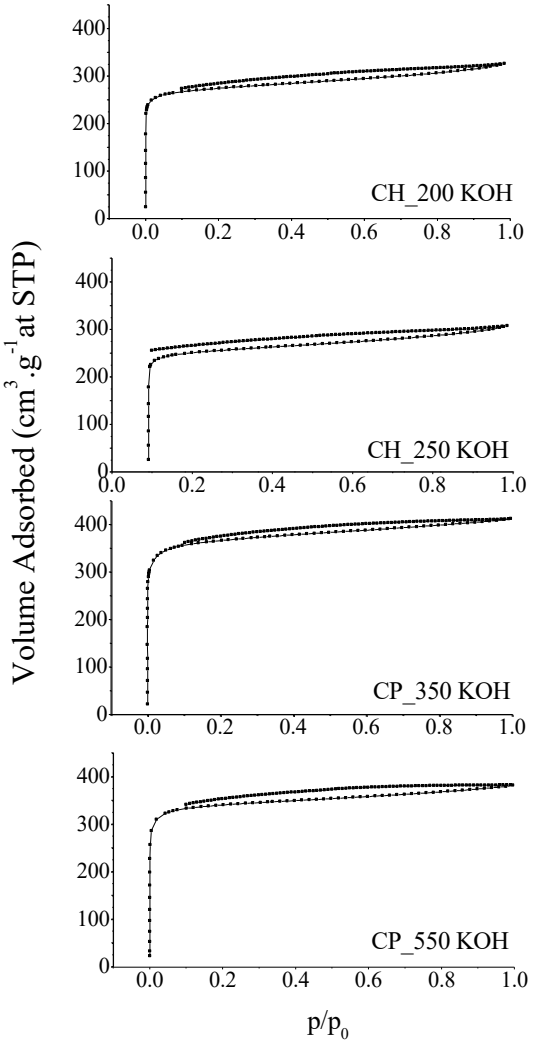

Source: Elaborated by the author.

Pore size distribution of activated samples (Figure 24) shows the increase on the number of pores with radius smaller than 2.5 nm, when compared to non-activated samples (Figure 17). What was already expected by the isotherm's shape.

Figure 24 - Pore size distribution for KOH activated samples from Stage II obtained by BJH method.

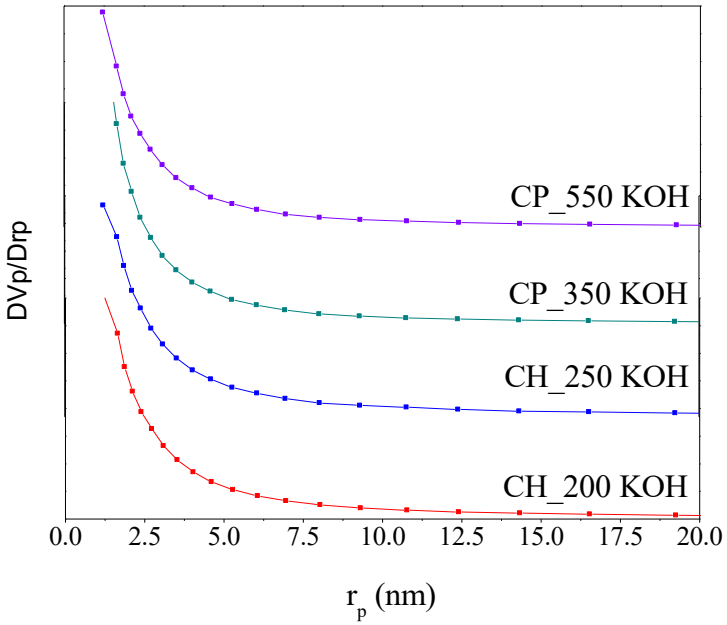

Source: Elaborated by the author.

The scanning electron microscopy (SEM images) of the samples (Figures 18 and 25) allows the visualization of drastic modifications in the sample´s morphology caused by thermochemical activation, making visible the open macrochannels in the particles probably due to the KOH carbonaceous matrix reactions and the subsequent elimination of K_2CO_3 after HCl wash and the elimination of volatile compounds (GONZÁLEZ-GARCÍA, 2018).

Figure 25 - SEM images of activated biochars produced by KOH activation at 700 °C.

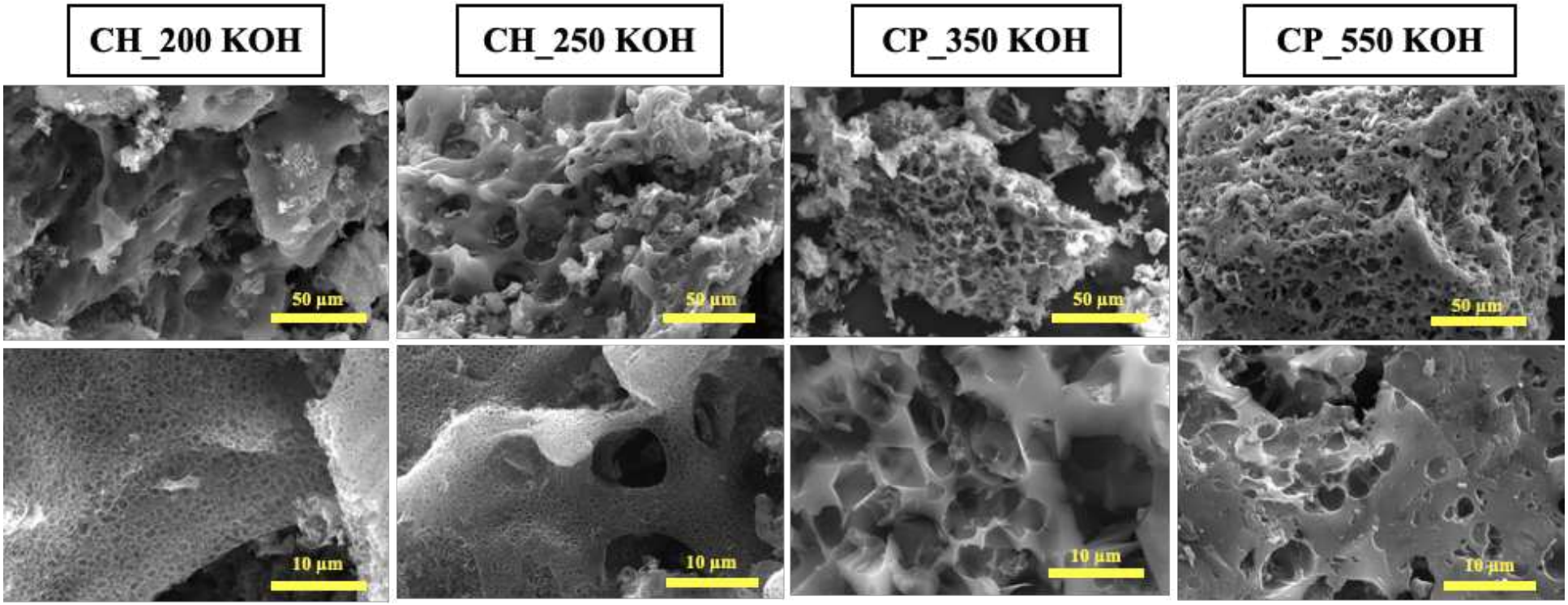

Source: Elaborated by the author.

As the final goal of studying biochar is soil application, it is important to analyze its pH as that can be determinant when matching soil and biochar type. In Table 17 are listed the value of the pH measurements for activated samples. All activated biochars presented acidic pHs. These results could be associated to washing step, since all activated samples was first HCl washed and subsequently washed with distilled water until pH of around 5. It is important to comment that the effect of the activation process on the elimination of nutrients in the biochars will be evaluated in future studies.

Table 17 – pH results for KOH activated samples from Stage II.

Sample	pH
CH_200 KOH	4.91
CH_250 KOH	5.38
CP_350 KOH	4.87
CP_550 KOH	6.83

Source: Elaborated by the author.

4.4 Water-biochar interaction and water retention capacity

4.4.1 Wetting properties

The first analysis concerning the interaction of biochar with water was the sessile drop technique. The results are expressed in Table 18. The technique is based on the liquid surface tension (BUBICI et al., 2016). In fact, superficial molecules in a liquid do not have neighboring molecules in all directions to provide a balanced net force. Instead, they are pulled inward by the neighboring molecules, thereby creating an internal pressure. As a result, the liquid contracts its surface area to maintain the lowest surface free energy (BUBICI et al., 2016). The more affinity the liquid has with the solid surface, the more it spreads on its surface (Figure 26a). Conversely, when affinity between the two phases decreases, the liquid beads on the solid (Figure 26b) (BUBICI et al., 2016).

According to the literature (BUBICI et al., 2016; EIBISCH et al., 2015), a material is considered hydrophilic if the angle between the solid surface and the external liquid wall of the drop forms an angle of less than 90°, and hydrophobic if the angle is more than 90°.

Figure 26 - Illustrative image of the contact angle for a drop of water on a (a) hydrophilic solid surface and on a (b) hydrophobic solid surface.

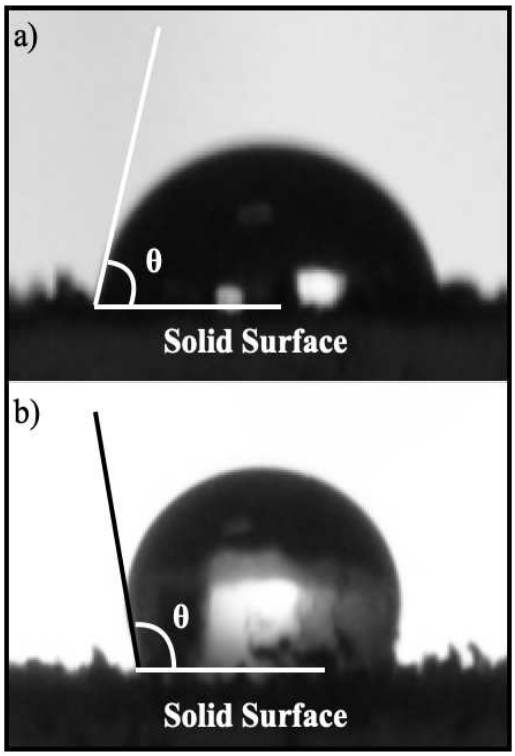

Source: Elaborated by the author.

Table 18 – Results of contact angle measured by sessile drop method for cashew bagasse (BC_2), samples produced in Stage II and activated biochars with KOH.

Sample	θ (°)
BC_2	62
CH_200	109
CH_250	113
CP_350	109
CP_550	94
CH_200 KOH	69
CH_250 KOH	76
CP_350 KOH	80
CP_550 KOH	71

Source: Elaborated by the author.

In the contact angle measurements of the Stage II samples, it was observed that even though BC_2 is hydrophilic, after pyrolysis (CP_350 and CP_550) and hydrothermal carbonization (CH_200

and CH_250) the samples get hydrophobic (Table 18). Considering all the reactions that BC_2 underwent during carbonization, this result is completely possible. Our sample characterization by CHNS elemental analyses, FTIR spectroscopy, X-ray diffractometry and scanning electron microscopy indicated that composition, structure and morphology of biochars were completely different compared to raw material. This acquired hydrophobicity can be related to aromatic moieties formation, and this compound is known to be hydrophobic (DOBLE; KUMAR, 2005; HE; GIANNIS; WANG, 2013; MAIER, 2019).

Comparing the contact angle results for hydrochars, they were found to be similar. Also, CP_350 showed similar contact angle value to the hydrochars. On the other hand, CP_550 showed a smaller contact angle (94 °) on the limit to be classified as hydrophobic. Considering that CP_550 had the greatest loss of functionalized groups (as shown by the infrared spectrum in Figure 13), and low surface area, this sample was not expected to be the most hydrophilic of the non-activated samples, since that materials with more polar groups and larger surface areas would be more hydrophilic (EIBISCH et al., 2015). Nevertheless, literature presents indicatives that high ash content can enhance hydrophilicity (MAO et al., 2019) and graphitic surfaces when exfoliated from airborne hydrocarbon contamination are hydrophilic (KOZBIAL et al., 2017). This sample was the non-activated biochar with highest ash content, and the most similar to graphitic structure.

The behavior of activated samples in relation to the precursor biochars stands out. The samples have become hydrophilic upon activation. Furthermore, the activated samples are similar to each other in this property, reflecting the similarities already observed in the FT-IR and Raman spectroscopies, XRD and N_2 adsorption-desorption isotherm measurements. As already cited in the literature, the development of hydrophilicity in activated samples can be associated to the increase in surface area (see Tables 12 and 16), as well as elimination of non-polar aliphatic and aromatic groups of organic compounds due to the reaction of KOH with carbon chains (Refer to Figures 13 and 20) (EIBISCH et al., 2015). Since hydrophilic, oxygen-containing functional groups or polar ends of amphiphilic molecules (molecules that contain both hydrophilic and hydrophobic components) can bind to each other and turn their non-polar ends to the surface under drying conditions, inducing water repellency (DOERR; SHAKESBY; WALSH, 2000).

Macroscopic tests on water-activated biochar interaction were made to observe the behavior of biochar's particles in water (Figure 27). For this, a small quantity of biochar was agitated in a beaker with 20 mL of ultrapure water and photographed after settlement (3 min). The visual inspection of these pictures reflects what we saw on the contact angle test for BC_2 and non-activated samples. Most of BC_2 sinks to the bottom of the beaker due to its high hydrophilicity. On the

contrary, CH_200, CH_250 and CP_350 samples do not even get soaked due to their high hydrophobicity. However, CP_550 sample showed small hydrophobicity in contact angle test, and part of it soaked and sinked to the bottom of the beaker as expected from a material that is almost classified as hydrophilic.

For activated samples, the results suggest that CH_200 KOH and CP_550 KOH samples tend to stay more stable in the water suspension than the other samples (Figure 27). This behavior is probably due to their high hydrophilicity, as shown in the contact angle test. By contrast, CP_350 KOH sample gathers in agglomerates of itself instead of spreading through water, which also agrees with the result for contact angle (the most hydrophobic sample among activated samples). However, our results do not agree with literature that states absolute proportion between surface area and hydrophilicity in biochars, since CP_350 KOH showed the highest result (847 m^2g^{-1}) (EIBISCH et al., 2015). Meanwhile, it is also important to comment that hydrophilicity on biochar is a complex subject and can be related to many factors (BIKBULATOVA et al., 2018; MANGRICH et al., 2015).

Figure 27 - Stage II samples and activated ones on ultrapure water after agitation and allowed to settle for 3 min. For these pictures a small quantity of biochar was agitated with 20 mL of ultrapure water.

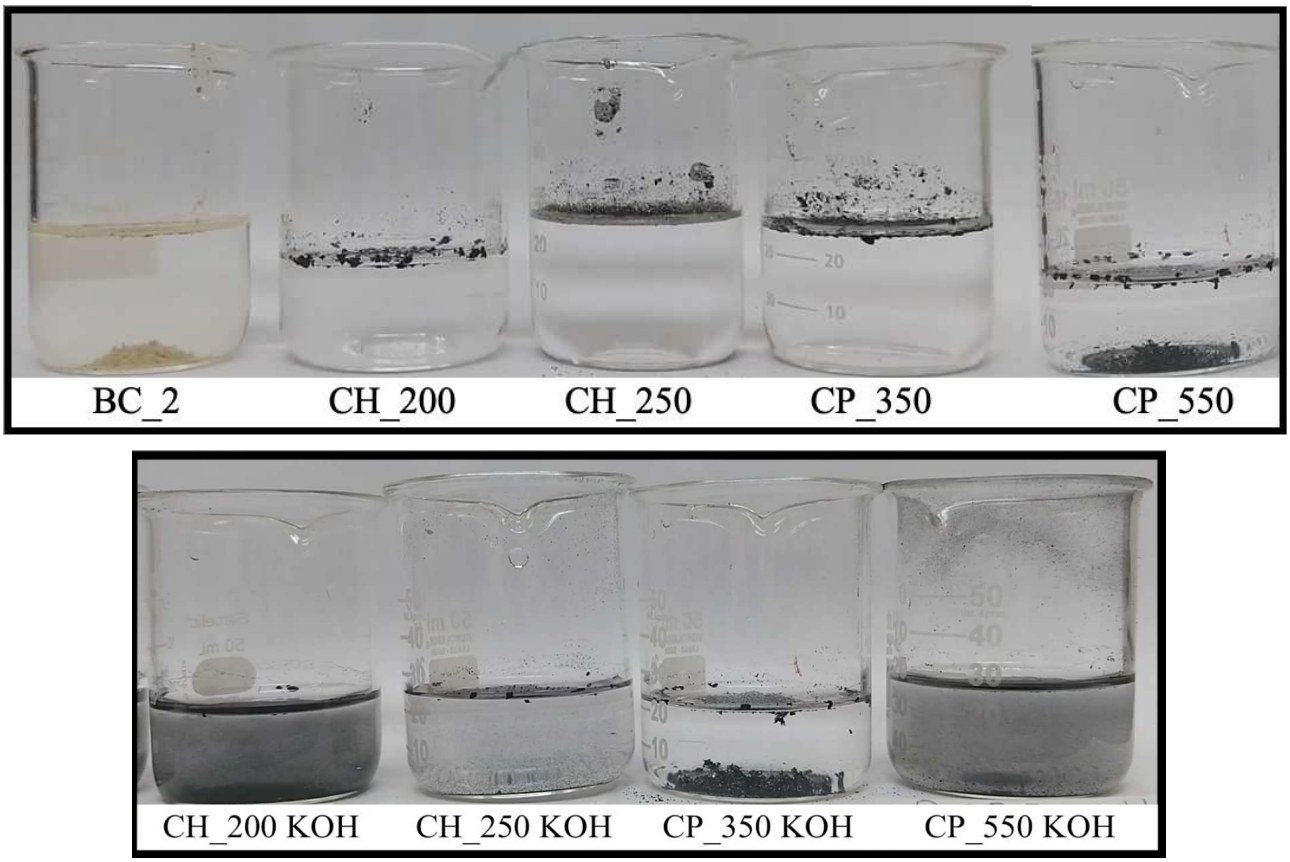

Source: Elaborated by the author.

Water holding capacity (WHC) experiments results of activated and non-activated Stage II samples are shown in Table 19. These experiments were performed only with biochar, to investigate their intrinsic WHC. A sandy soil was also examined for comparison. The characterization of this soil is described Table 20.

The results expressed in Table 19 represent the mass gain due to the water retention. Under this light, it was observed during saturation for WHC test that hydrochars were much harder to soak, but they were also less dense, demanding a greater amount of water to be completely immerse. Results on textural properties corroborate showing that hydrochar pore volume were a little higher than pyrochars (Table 12). So hydrochars could have more sites for water accommodation in their structure. The difficulty to soak and latter higher WHC of hydrochars (when compared to pyrochars) can be related to the fact that hydrochars present water repellency on dry conditions due to the presence of amphiphilic functional groups, as already discussed in contact angle results (DOERR; SHAKESBY; WALSH, 2000; EIBISCH et al., 2015). Also, great increase in WHC was observed when comparing activated to non-activated samples. The greatest increase was observed in CP_350 sample after activation (from 147 % to 399 % for CP_350 KOH), although the highest absolute retention value was observed for activated hydrochars (almost 500 %). Comparing these results (Table 19) to the results of surface area, pore volume and average pore diameter (Table 16), WHC of activated samples seems to be more direct proportional to pore volume than specific surface area (Table 16). This value can also be related to surface functional groups, pore volume and pore size distribution (ABEL et al., 2013b; BIKBULATOVA et al., 2018; CONTE et al., 2013; MANGRICH et al., 2015).

Table 19 – Results of water holding capacity (WHC) expressed as percentage of mass gain for non-activated and activated and samples. Soil was described for comparison.

Sample	WHC (%)
Soil	138
CH_200	365
CH_250	300
CP_350	147
CP_550	132
CH_200 KOH	499
CH_250 KOH	499
CP_350 KOH	399
CP_550 KOH	220

Source: Elaborated by the author.

4.4.2 Plant Available Water Capacity (PAWC) test

To analyze the behavior of biochars on soil under water interaction light, PAWC tests were done. In these tests, the part of the water retained that is available for plants can be calculated. For so, a sandy soil (collected in Cascavel, Ceará state, Brazil - 4°07'39.6"S 38°11'02.6"W) was mixed with 1% (w:w) of each activated or non-activated biochar. Soil characterization results are showed in Table 20. Regarding texture, the soil was classified as sandy. Soil carbon content was 25.38 g/kg, nitrogen content was 2.79 (g/kg), assimilable phosphorus content was 12 (mg/kg), global density 1.09 g/cm^3, particle density 2.55 g/cm^3, pH 5.6 and electrical conductivity 6.1 dS m^{-1}. Assorted complex, granulometric composition are described in Table 20:

Table 20 – Physicochemical properties of the soil used in the plant available water capacity (PAWC) tests.

Soil Exchangeable Cations (cmol$_c$/kg)		**Granulometric Composition (g/kg)**	
Ca^{2+}	4.80	Coarse Sand	541
Mg^{2+}	0.60	Thin Sand	353
Na^{+}	0.60	Silt	78
K^{+}	0.60	Clay	28
H^{+}+Al^{3+}	7.92	Natural Clay	25
Al^{3+}	0.45		
S*	6.6		
T**	14.5		

Source: elaborated by the author.
*Sum of bases
** Cation Exchange Capacity at pH 7.

The test was performed in triplicate and soil with no biochar was used as control. The results showed (Figure 28) that soil added with hydrochars (CH_200 e CH_250) and CP_350 pyrochar presented only a small increase in PAWC. PAWC results show that surface hydrophilicity is not the predominant factor for non-activated samples, since the 3 most water repellent non-activated biochars presented the best PAWC. This result can be related to a more open particle packing configuration of soil and formation of pores between soil and biochar particles. On the other hand, CP_550 pyrochar added to sandy soil promoted a decrease in PAWC, agreeing with the previous result that CP_550 had

a smaller WHC than soil (Table 19). LIU et al. (2017) observed that big biochar particles may create spaces in soil that enhances water leakage, since CP_550 was more granular than the other samples, then granules size could be the parameter more responsible to low PAWC values observed for this sample. Another hypothesis is that this behavior may reflect biochar porosity. The CP_500 sample has the lowest pore volume, indicating the collapse of the pore structure when the heat treatment was carried out at higher temperatures.

It is important to observe that N_2 adsorption-desorption technique is more appropriate to study micro and mesoporous materials (THOMMES et al., 2015). So, the influence of sample's macro porosity was not accessed in these studies. Also, according to Embrapa's Manual of Soil Analysis Methods, water in pores smaller than 200 nm is not available for plants. Then, a study on the macroporosity of the samples could probably present a better explanation for PAWC results and direct relation to texture features (TEIXEIRA et al., 2017).

Since activated carbon is used as adsorbent, activated samples were expected to have the highest retention capacity. So, as expected, the highest results were achieved with activated biochars (Figure 28). The highest one was CH_250 KOH, which contained about 4.5 times more water available for plants than the control (Figure 28). The other samples followed the same tendency, but CP_550 KOH samples presented the smaller PAWC (only 2.4 times more water than control). These results show that KOH activated biochar can retain more water for agricultural usage and that the high micro porosity formation did not prevent high plant available water release. SEM results show formation of macropores that may be linked to the enhancement of PAWC (Figure 25). In Figure 29 is showed PAWC versus WHC curve. It is also showed the linear regression presenting a R^2 of 0.79. This value for R^2 would be a relevant linear relation since for soil experiments R^2 results ≥ 0.8 are considered to be very reliable (SILVA et al., 2017). That indicates that the biochar WHC is a good indicator of soil-biochar PAWC for this soil type.

Figure 28 – Results of plant available water capacity (PAWC) expressed as percentage of mass gain for Stage II activated and non-activated samples. Soil was described for comparison.

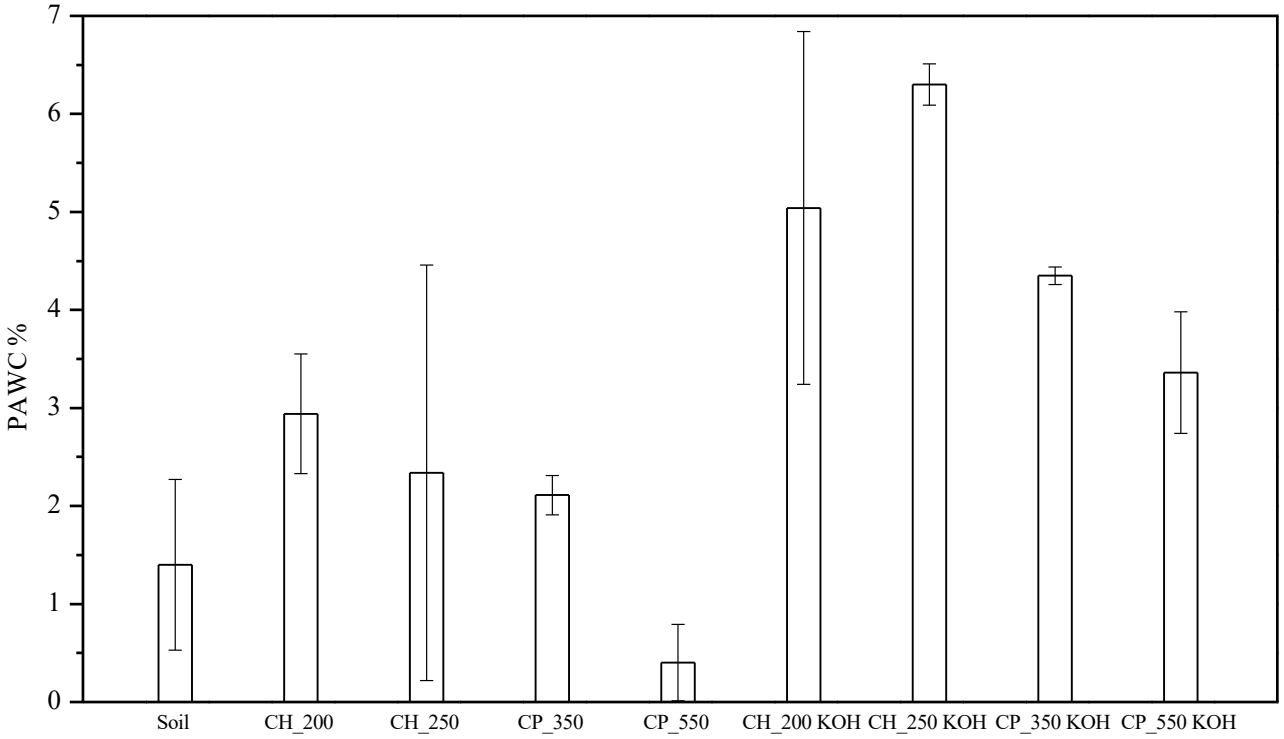

Source: Elaborated by the author.

Figure 29 – Plant Available Water Capacity and Water holding Capacity linear regression for activated and non-activated samples from Stage II. Soil is described for comparison.

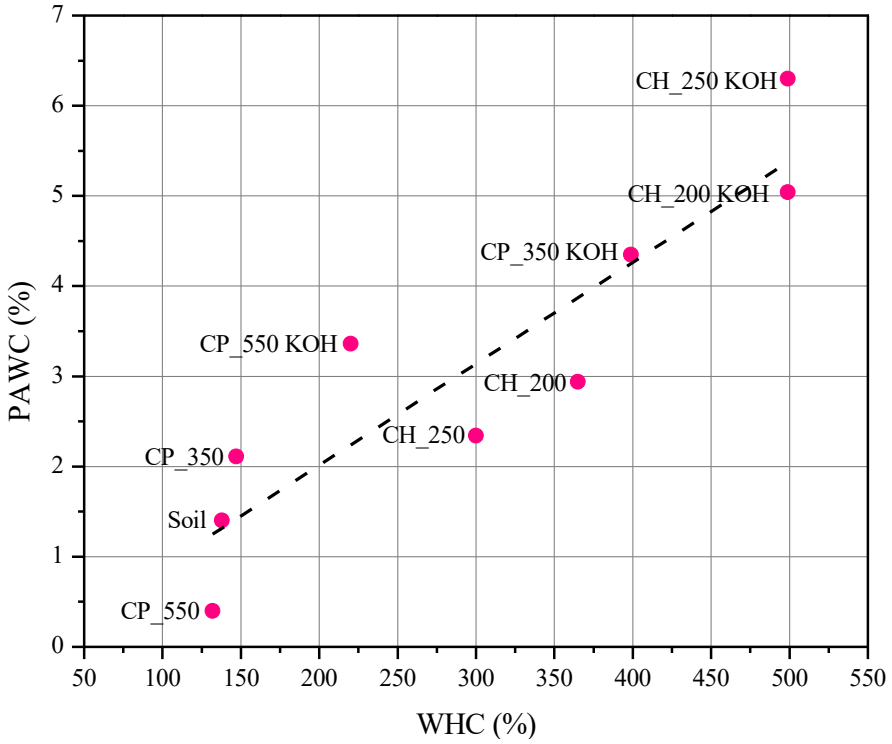

Source: Elaborated by the author.

Table 21 shows some achievements from literature for PAWC results. Most of these studies use a soil that has a better capacity to retain water naturally and a higher biochar:soil ratio. Overall, none of the results are as expressive as the one achieved in this work when compared to initial soil PAWC.

Table 21 – Achievements for Plant Available Water Capacity (PAWC) from Literature.

Feedstock	Carbonization Method	Soil Type	Biochar: Soil Ratio	Soil PAWC (%)	Soil + Biochar PAWC (%)	Reference
Eucalyptus spp. bark	Slow Pyrolysis	Sandy loam	0.5, 1, 2, 4 and 6 %	8.6	8.5, 8.7, 9.2, 9.3, 12 respectively	TANURE et al., 2019
Pine Wood, Pine Bark and Poplar Wood	Pyrolysis and Air Oxidation	Sandy	2	11.5	17 - 24	(SULIMAN et al., 2017)
Corn stover and Switchgrass	Fast and Slow Microwave-Pyrolysis	Fine Sandy and Clay	4	10 (sandy) and 13 (clay)	12 - 17	(MOLLINEDO; SCHUMACHER; CHINTALA, 2015)
Mesquite	Pyrolysis	Sandy	2	2	4	(LIU et al., 2017)
Digestate and woodchips	Pyrolysis and hydrothermal carbonization	loamy sand	2	-	Up to 15 % increase (hydrochar)	(EIBISCH et al., 2015)
Beechwood (pyrolysis) maize silage (HC)	Pyrolysis and hydrothermal carbonization	Sandy	1, 2.5 and 5	12.7	16.2, 16.2 and 17.2	(ABEL et al., 2013)

Source: Elaborated by the author.

4.4.3 Low-temperature Differential Scanning Calorimetry (DSC) analysis

DSC analysis was performed in order to get information about how water would interact with chars on a microscopic level (Figures 30 and 31). To do so, biochars were saturated with ultrapure water and vacuum dried to achieve a specified moisture level (60, 80 or 100 % water:biochar ratio). Different levels of humidity were applied because it would be more easily distinguishable when all present water would be water present in micropores or non-freezing water. During DSC analysis, moisturized chars would undergo temperatures from 20 to -60 ºC while the heat flow was recorded and compared to a reference sample (empty crucible). In this way, any phase change in water would be detected as an exothermic peak in heat flow *versus* temperature curves.

Before any measurements with biochar samples, the test with the temperature cycle was applied to only ultrapure water. It was observed only one exothermic peak during the cooling process that appeared in -20 °C, going up to -15.7 mW/mg due to water solidification. Supercooling happened

probably because of the high purity of water used, and the lack of vibrations during the experiment (CHEN; LEE, 1998). This experiment was also done in order to compare sole ultrapure water behavior to those adsorbed on biochars samples.

Figure 30 – Differential scanning Calorimetry (DSC) curves recorded during the cooling process on the second run for activated and non-activated hydrochars from Stage II with different water contents. Moist contents were calculated according to Equation 5.

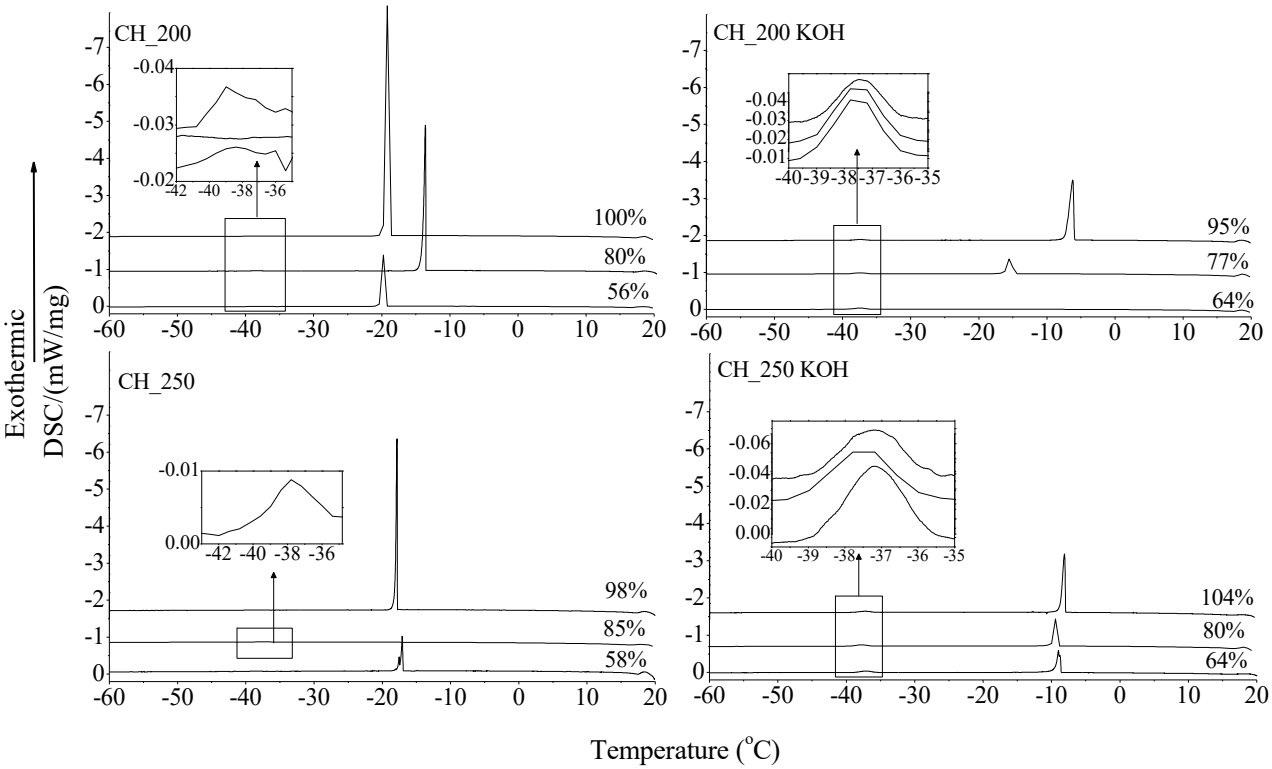

Source: Elaborated by the author.

Figure 31 – Differential scanning Calorimetry (DSC) curves recorded during the cooling process on the second run for activated and non-activated pyrochars from Stage II with different water contents. Moist contents were calculated according to Equation 5.

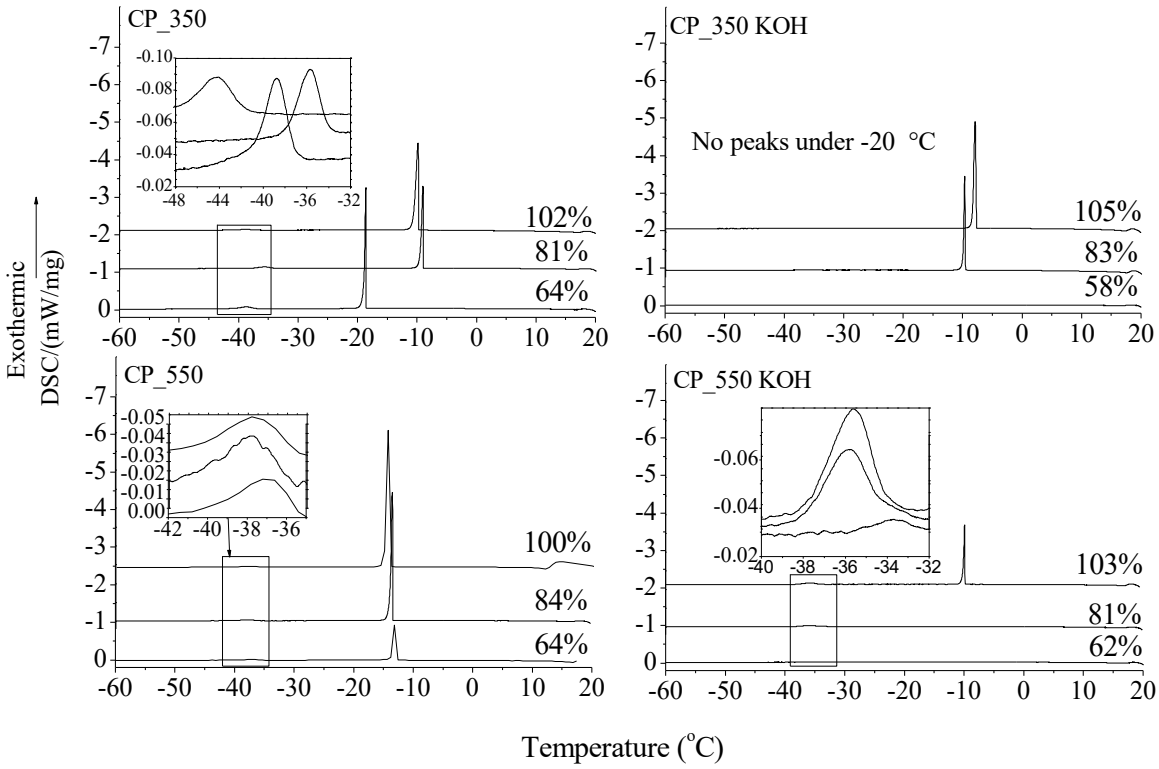

Source: Elaborated by the author.

Overall, it was observed two main exothermic peaks in the DSC curves for the most samples, one intense between -10 and -20 °C and other of low intensity between -32 and -48 °C. The intense exothermic peak observed between -10 and -20 °C was attributed to solidification of bulk water. On the other hand, low intensity exothermic peak between -32 and -48 °C would be due to the water present in micropores (NWAKA et al., 2016; BIKBULATOVA et al., 2018). The fact that water in solid phase has longer molecule-molecule distance than in liquid phase explains why when liquid water is confined in small spaces it would be harder to solidify (JÄHNERT et al., 2008). This fact probably explains why water present in micropores solidified at lower temperatures. So, in micropores there was probably no available space at -20 °C to solidify. Only in lower temperatures there was sufficient enthalpy for solidification.

In Figure 32, are plotted the peak areas for bulk water solidification as a function of humidity in the samples. The peak area corresponds to the total energy (in joules) per sample mass (grams) released during solidification (HÖHNE; HEMMINGER; FLAMMERSHEIM, 2003). The energy

released per mass for most samples increased with humidity (Figure 32), this is probably due to more water not entrapped in micropores nor too bound to the surface and free to solidify and release energy.

Figure 32 – Peak area (J/g) calculated from DSC curves for bulk water solidification around - 20 and - 10 °C.

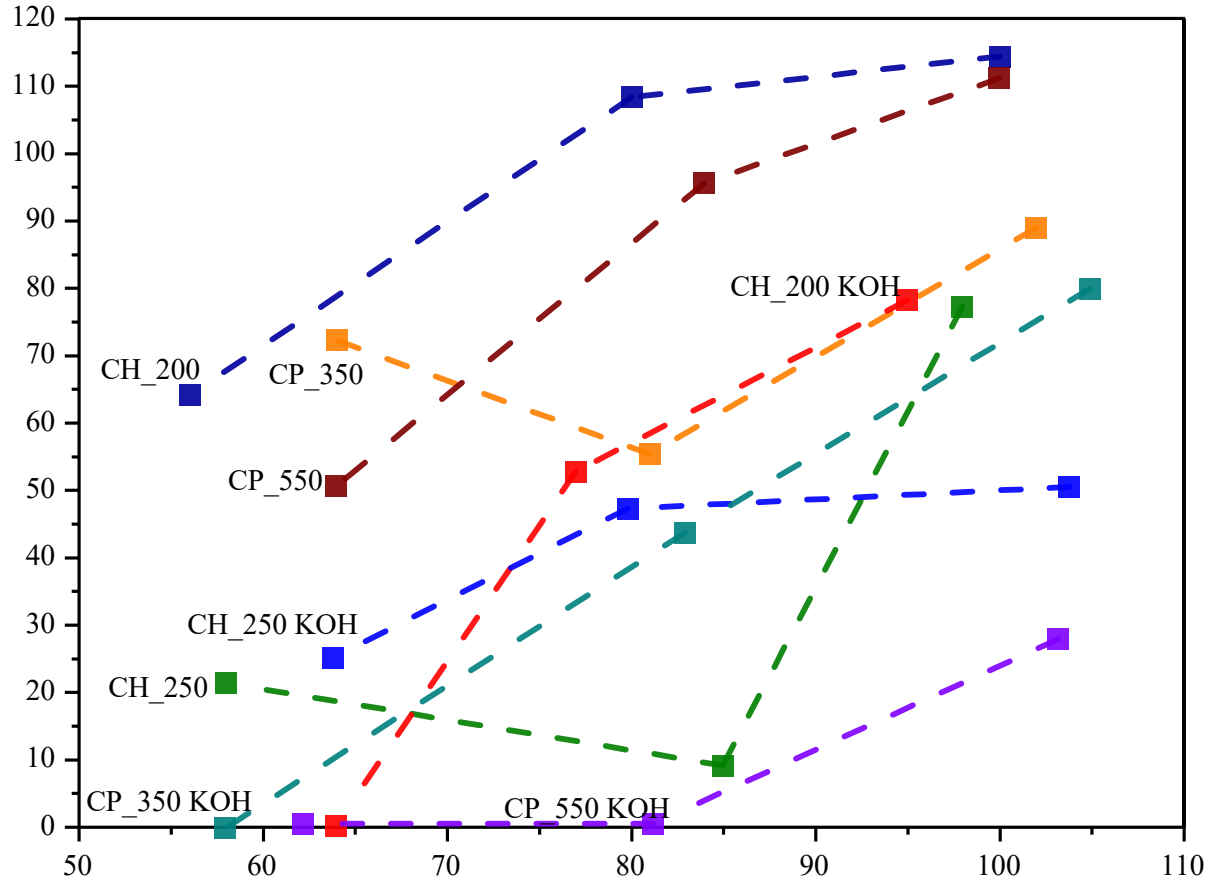

Source: Elaborated by the author.

For hydrochars (CH_200 and CH_250) in all humidity levels studied, the DSC curves present the main exothermic peak between – 20 and – 10 °C attributed to bulk water (Figure 30). On contrary, micropore water peaks around – 48 and -32 °C were almost negligible. These results are consistent with already discussed, as N_2 adsorption-desorption isotherms of hydrochar showed that they were predominantly a macropore system (Figures 4 and 16). Also, contact angle showed that they had little affinity with water (Table 18). Such that water was not as bonded to it as to all other samples, nor it had micropores to lodge water, so it was expected that the all water present change to solid phase at the same temperature. Hydrochars showed the highest solidification peaks among samples (Figure 30), when comparing 100 % humidity samples. CH_200 samples showed the highest peak area for

all humidity levels (Figure 32), meaning that the release of energy during solidification for these samples had the highest potency (mW) per mg. However, they showed low intensity peaks attributed to water in micropores, agreeing with the fact that they were a non-porous or macroporous sample.

The DSC curves for activated hydrochars (CH_200 KOH and CH_250 KOH) (Figure 30), presented bulk water peaks (around -10 and -20 °C) that diminished a lot in intensity when compared to non-activated samples. Also, stronger micropore water peaks (around -32 and -48 °C) appeared after activation, for each level of humidity. That is again are consistent with textural properties of the activated samples that present micropores as revealed by N_2 adsorption/desorption technique. Also, it was observed that bulk water solidification peaks migrated to a higher temperature, they were around -20 °C before activation and then shifted to around -10 °C for activated samples. These results indicates that activation made the supercooling harder, probably because the activated hydrochars gave to water more nucleation sites for solidification (CHEN; LEE, 1998).

Pyrochars (Figure 31) in general presented different results from that of hydrochars, with less intense peaks for bulk water and they were closer to 0 °C for almost all levels of humidity, and much more significant micropore water peaks, with very surprising results for CP_350 sample, that showed the highest peaks for micropore water among all samples. This can be explained if a link with N_2 adsorption-desorption isotherms is made (Figure 16). Since the shape of pyrochar's isotherms had a characteristic hysteresis attributed to materials where pores communicate with the surface through narrow channels, from which adsorption and condensation of gases are more difficult to exit, meaning that these pores could also trap water and make them harder to solidify than bulk water. Nevertheless, the two pyrochar samples responded to DSC analyses in a distinct manner after activation. While CP_350 KOH showed a little higher bulk water peaks and no micropore water peaks, CP_550 KOH showed smaller, or no bulk water peaks and higher micropore water peaks. But both samples showed a little shift of bulk water peak towards higher temperatures just like activated hydrochars. This indicates that activation could have opened up the narrow channels in CP_350 and created more microporosity in CP_550. It is also noticeable that the most hydrophilic samples (CH_200 KOH and CP_550 KOH) had smaller and less bulk water peaks, indicating that less or no water solidified either because they were either trapped in micropores or stayed supercooled. This could be an indication that they are capable to retain water, but it was verified that they were not the most capable of delivering it to plants (Figure 28).

Finally, the sample with highest PAWC (CH_250 KOH) was also the only activated sample that had bulk water and relevant micropore water peaks in all moist ratios. That was also observed

for CP_350 and CP_550, but both samples had very timid surface area and pore volume results. This indicates that even though not determinant, surface area and pore volume contribute to PAWC.

5 CONCLUSIONS

Waste obtained from industrial processing of cashew was reused as a raw material for preparation of carbon-based functional nanostructured materials to study the interaction between water and biochars for application as soil conditioner, focusing on water retention. Nanostructured carbon-based materials were prepared by the techniques of hydrothermal carbonization and pyrolysis, combined with thermochemical activation.

The structure, composition, morphology and texture of biochars subjected to different reaction conditions (carbonization temperature, precursor mass and reaction time) were evaluated. It was possible to produce biochars from cashew bagasse with different features, for example, with functionalized surface (CHs) or non-functionalized surface (CPs), low structural organization and low surface area. According to SEM images they are formed by carbon micrometric spheres (CHs) or particles with micrometric irregularities with some macropores (CPs) and according to contact angle test, are predominantly hydrophobic. It was also evident that the most important reactions of hydrothermal carbonization occur in the first 4 h of carbonization.

The effect of thermochemical activation on hydro and pyrochars regarding porosity formation and its influence on water retention was studied. After thermochemical activation, the biochars remained carbon-rich, but many functional groups were eliminated. They remained with low structural organization and their specific surface area increased by the formation of micropores and tunnels and became predominantly hydrophilic. Hydrophilicity enhancement was probably related to expansion on surface area and pore volume and the elimination of amphiphilic surface functional groups.

The DSC exothermic peaks indicated a tendency of activated samples to lodge a small part of water on less accessible pores, but this did not prevent the samples from increasing appreciably soil PAWC. WHC and PAWC results were found to have a relevant linear correlation ($R^2 = 0.79$). No direct relation between texture and water retention results were observed. Probably, the N_2 adsorption-desorption method is designed to observe pores in a smaller size range than the pores that contributed to water retention and posterior delivery to plants.

Notwithstanding, the most hydrophilic non-activated sample (CP_550) had the smallest results for WHC and PAWC, as well as the worst results for specific surface area and pore volume. It was found that although hydrochars were very hydrophobic, that could be overcome with enough saturation and it is probably linked to the presence of amphiphilic molecules on the dry hydrochar surface. That can be a challenge in a field study since it can put on some difficulty when watering

plants. Nonetheless, activation enhanced hydrophilicity and 1% addition of CH_250 KOH sample to soil improved PAWC from 1.4% to 6.3%. Addition of activated and non-activated pyrochars were not so expressive, and 1% addition of CP_550 sample did worsen soil PAWC from 1.4% to 0.4%. This result is important to unravel the importance of chemical activation of biochar for agricultural usage. Also, few studies were done on this feedstock for biochar, and most that were done with different feedstocks did not improve PAWC as much as activated samples in this study. In addition, these numbers could be underestimated if it is considered that Field Capacity in Sandy soils is usually higher than -0.33 bar. It can be an indicative that the studied biochars are even more capable of water retention for plants than presented in the literature (TANURE et al., 2019; SULIMAN et al., 2017; MOLLINEDO; SCHUMACHER; CHINTALA, 2015; LIU et al., 2017; EIBISCH et al., 2015; ABEL et al., 2013)

This work successfully reused residues obtained from cashew industrial processing as a precursor source for carbon-based functional materials preparation, which can be used for application as soil conditioners, especially for water retention.

6 BIBLIOGRAPHY

ABEL, S.; PETERS, A.; TRINKS, S.; SCHONSKY, H.; FACKLAM, M.; WESSOLEK, G. Impact of biochar and hydrochar addition on water retention and water repellency of sandy soil. **Geoderma**, v. 202, p. 183–191, 2013.

AKBAR, D.; GÜNGÖR, Ü. E. Study of high radio frequency plasma discharge effects on carbon fiber using Raman spectroscopy. **Surface and Coatings Technology**, v. 240, p. 233–242, 2014.

ANOARDO, E.; GALLI, G.; FERRANTE, G. Fast-field-cycling NMR: applications and instrumentation. **Applied Magnetic Resonance**, v. 20, n. 3, p. 365–404, 2001.

ATKINSON, C. J.; FITZGERALD, J. D.; HIPPS, N. A. Potential mechanisms for achieving agricultural benefits from biochar application to temperate soils: a review. **Plant and soil**, v. 337, n. 1–2, p. 1–18, 2010.

AZARGOHAR, R.; DALAI, A. K. Steam and KOH activation of biochar: Experimental and modeling studies. **Microporous and Mesoporous Materials**, v. 110, n. 2–3, p. 413–421, 2008.

BANKS, S. W.; BRIDGWATER, A. V. Catalytic fast pyrolysis for improved liquid quality. In: **Handbook of Biofuels Production**. [s.l.] Elsevier, 2016. p. 391–429.

BASSILAKIS, R., ZHAO, Y., SOLOMON, P. R., & SERIO, M. A. Sulfur and nitrogen evolution in the Argonne coals. Experiment and modeling. **Energy & Fuels**, v. 7, n. 6, p. 710–720, 1 nov. 1993.

BIKBULATOVA, S.; TAHMASEBI, A.; ZHANG, Z.; RISH, S. K.; YU, J. Understanding water retention behavior and mechanism in bio-char. **Fuel Processing Technology**, v. 169, p. 101–111, 2018.

BREWER, C. E.; HU, Y. Y.; SCHMIDT-ROHR, K.; LOYNACHAN, T. E.; LAIRD, D. A.; BROWN, R. C. Extent of pyrolysis impacts on fast pyrolysis biochar properties. **Journal of environmental quality**, v. 41, n. 4, p. 1115–1122, 2012.

BUBICI, S.; KORB, J. P.; KUČERIK, J.; CONTE, P. Evaluation of the surface affinity of water in three biochars using fast field cycling NMR relaxometry. **Magnetic Resonance in Chemistry**, v. 54, n. 5, p. 365–370, 2016.

CASTRO, A. J. R. **(Nano)Materiais À Base De Carbono E Nitrogênio Obtidos A Partir Da Carbonização Hidrotérmica De Biomassa**. Thesis (Masters in Physics) – Department of physics, Federal University Of Ceará, 2013.

CASTRO, A. J. R. DE. **Carbonização Hidrotérmica e Celulose e Nanocelulose e Preparação De Compósitos Magnéticos em Única Etapa**. Dissertation (Doctor in Physics) – Department of physics, Federal University of Ceará, 2018.

CASTRO, M. O. **Micro E Nanopartículas De Carbono Obtidas Por Carbonização Hidrotérmica: Preparação, Caracterização E Interação Com Proteína**. Dissertation (Doctor in Physics) – Department of physics, Federal University of Ceará, 2017.

CHARRIÈRE, D.; BEHRA, P. Water sorption on coals. **Journal of Colloid and Interface Science**, v. 344, n. 2, p. 460–467, 2010.

CONTE, P.; HANKE, U. M.; MARSALA, V.; CIMÒ, G.; ALONZO, G.; GLASER, B. Mechanisms of Water Interaction with Pore Systems of Hydrochar and Pyrochar from Poplar Forestry Waste. **Journal of Agricultural and Food Chemistry**, v. 62, n. 21, p. 4917–4923, 28 maio 2014.

CONTE, P.; MARSALA, V.; DE PASQUALE, C.; BUBICI, S.; VALAGUSSA, M.; POZZI, A.; ALONZO, G. Nature of water-biochar interface interactions. **GCB Bioenergy**, v. 5, n. 2, p. 116-121, 2013.

CORREIA, J. A. C.; JÚNIOR, J. E. M.; GONÇALVES, L. R. B.; ROCHA, M. V. P. Alkaline hydrogen peroxide pretreatment of cashew apple bagasse for ethanol production: study of parameters. **Bioresource Technology**, v. 139, p. 249–256, 2013.

DAI, Z.; ZHANG, X.; TANG, C.; MUHAMMAD, N.; WU, J.; BROOKES, P. C.; XU, J. Potential role of biochars in decreasing soil acidification-A critical review. **Science of the Total Environment**, v. 581, p. 601–611, 2017.

DOERR, S. H.; SHAKESBY, R. A.; WALSH, R. P. D. Soil water repellency: its causes, characteristics and hydro-geomorphological significance. **Earth-Science Reviews**, v. 51, n. 1, p. 33–65, 2000.

EIBISCH, N.; DURNER, W.; BECHTOLD, M.; FUSS, R.; MIKUTTA, R.; WOCHE, S. K.; HELFRICH, M. Does water repellency of pyrochars and hydrochars counter their positive effects on soil hydraulic properties? **Geoderma**, v. 245–246, p. 31–39, 2015.

ENDERS, A.; HANLEY, K.; WHITMAN, T.; JOSEPH, S.; LEHMANN, J. Characterization of biochars to evaluate recalcitrance and agronomic performance. **Bioresource technology**, v. 114, p. 644–653, 2012.

FALCO, C.; BACCILE, N.; TITIRICI, M.-M. Morphological and structural differences between glucose, cellulose and lignocellulosic biomass derived hydrothermal carbons. **Green Chemistry**, v. 13, n. 11, p. 3273–3281, 2011.

FANG, J.; GAO, B.; CHEN, J.; ZIMMERMAN, A. R. Hydrochars derived from plant biomass under various conditions: Characterization and potential applications and impacts. **Chemical Engineering Journal**, v. 267, p. 253–259, 2015.

FREGOLENTE, L. G. Vinhaça da Indústria Sucroalcooleira como Matéria-Prima na Carbonização Hidrotérmica. 2015.

GHOSH, A.; DO AMARAL RAZZINO, C.; DASGUPTA, A.; FUJISAWA, K.; VIEIRA, L. H. S.; SUBRAMANIAN, S.; TERRONES, M. Structural and electrochemical properties of babassu coconut mesocarp-generated activated carbon and few-layer graphene. **Carbon**, v. 145, p. 175–186, 2019.

HARDIE, M.; CLOTHIER, B.; BOUND, S.; OLIVER, G.; CLOSE, D. Does biochar influence soil physical properties and soil water availability? **Plant and Soil**, v. 376, n. 1, p. 347–361, mar. 2014.

HÖHNE, G. W. H.; HEMMINGER, W. F.; FLAMMERSHEIM, H.-J. **Differential Scanning Calorimetry**. 2. ed. Berlin: Springer, 2003.

HUANG, Y. F.; KUAN, W. H.; CHIUEH, P T; LO, S. L. Pyrolysis of biomass by thermal analysis–mass spectrometry (TA–MS). **Bioresource technology**, v. 102, n. 3, p. 3527–3534, 2011.

IBI. **Biochar-international**: Biochar International Iniciative, c2018. Sustainability & Climate Change. [S.I]. [2013?]. Available at: <https://biochar-international.org/sustainability-climate-change/>. Accessed in: Aug 19, 2020.

IBI. **Standardized product definition and product testing guidelines for biochar that is used in soilIBI biochar standards**. 2015. Available at: <https://www.biochar-international.org/wp-content/uploads/2018/04/IBI_Biochar_Standards_V2.1_Final.pdf>. Accessed in: Mar 6, 2021.

IBGE. **Sidra**: Banco de Tabelas Estatísticas, 2018. Tabela 1613. Available at: <https://sidra.ibge.gov.br/tabela/1613#resultado>. Accessed in: Aug 19, 2020.

USBI. **Biochar-US**: Building the Future from the Ground Up, 2020. Biochar Then & Now. Avaiable at: <https://biochar-us.org/biochar-then-now>. Accessed in: Aug 19, 2020.

IPECE. **IPECE Informe –Nº 166–Janeiro/2020: Desempenho do Comércio Exterior do Ceará em 2019**. [s.l: s.n.]. Available at: <https://www.ipece.ce.gov.br/wp-content/uploads/sites/45/2020/01/ipece_informe_166_29_jan2020.pdf>.

JÄHNERT, S.; CHÁVEZ, F. V.; SCHAUMANN, G. E.; SCHREIBER, A.; SCHÖNHOFF, M.; FINDENEGG, G. H. Melting and freezing of water in cylindrical silica nanopores. **Physical Chemistry Chemical Physics**, v. 10, n. 39, p. 6039–6051, 2008.

JIN, H.; CAPAREDA, S.; CHANG, Z.; GAO, J.; XU, Y.; ZHANG, J. Biochar pyrolytically produced from municipal solid wastes for aqueous As (V) removal: adsorption property and its improvement with KOH activation. **Bioresource technology**, v. 169, p. 622–629, 2014.

KADIOĞLU, Y.; VARAMAZ, M. The effect of moisture content and air-drying on spontaneous combustion characteristics of two Turkish lignitesa. **Fuel**, v. 82, n. 13, p. 1685–1693, 2003.

KAJI, R.; MURANAKA, Y.; OTSUKA, K.; HISHINUMA, Y. Water absorption by coals: effects of pore structure and surface oxygen. **Fuel**, v. 65, n. 2, p. 288–291, 1986.

KEILUWEIT, M.; NICO, P. S.; JOHNSON, M. G.; KLEBER, M. Dynamic molecular structure of plant biomass-derived black carbon (biochar). **Environmental science & technology**, v. 44, n. 4, p. 1247–1253, 2010.

KIM, K. H.; KIM, J. Y.; CHO, T. S.; CHOI, J. W. Influence of pyrolysis temperature on physicochemical properties of biochar obtained from the fast pyrolysis of pitch pine (Pinus rigida). **Bioresource Technology**, v. 118, p. 158–162, 2012.

KIM, S. H.; LEE, C. M.; KAFLE, K. Characterization of crystalline cellulose in biomass: Basic principles, applications, and limitations of XRD, NMR, IR, Raman, and SFG. **Korean Journal of Chemical Engineering**, v. 30, n. 12, p. 2127–2141, 2013.

LARKIN, P. J. **Infrared and Raman Spectroscopy**. Oxford: Elsevier, 2011.

LEE, Y. E.; JO, J. H.; KIM, I. T.; YOO, Y. S. Chemical Characteristics and NaCl Component Behavior of Biochar Derived from the Salty Food Waste by Water Flushing. **Energies**, v. 10, n. 10, p. 1555, 2017.

LEHMANN, J.; GAUNT, J.; RONDON, M. Bio-char sequestration in terrestrial ecosystems–a review. **Mitigation and adaptation strategies for global change**, v. 11, n. 2, p. 403–427, 2006.

LI, S.; WHITELY, N.; XU, W.; PAN, W. P. Characterization of coal by thermal analysis methods. 2005.

LIMA, A. C.; PAIVA, F. F. A.; MORAES, I.; V. M.; NETO, R. M. S. **Industrialização do caju**. Disponível em: <https://www.spo.cnptia.embrapa.br/conteudo?p_p_id=conteudoportlet_WAR_sistemasdeproducaolf6_1ga1ceportlet&p_p_lifecycle=0&p_p_state=normal&p_p_mode=view&p_p_col_id=column-1&p_p_col_count=1&p_r_p_-76293187_sistemaProducaoId=7705&p_r_p_-996514994_topicoId=1>. Acesso em: 11 dez. 2020.

LIU, C.; WANG, H.; KARIM, A. M.; SUN, J.; WANG, Y. Catalytic fast pyrolysis of lignocellulosic biomass. **Chemical Society Reviews**, v. 43, n. 22, p. 7594–7623, 2014.

LIU, Z.; DUGAN, B.; MASIELLO, C. A.; GONNERMANN, H. M. Biochar particle size, shape, and porosity act together to influence soil water properties. **Plos one**, p. 1–20, 2017.

MANGRICH, A. S.; CARDOSO, E. M. C.; DOUMER, M. E.; ROMÃO, L. P. C.; VIDAL, M; RIGOL, A.; NOVOTNY, E. H. Improving the water holding capacity of soils of Northeast Brazil by biochar augmentation. In: **Water Challenges and Solutions on a Global Scale**. [s.l.] ACS Publications, 2015. p. 339–354.

MAO, J.; ZHANG, K.; CHEN, B. Linking hydrophobicity of biochar to the water repellency and water holding capacity of biochar-amended soil. **Environmental Pollution**, v. 253, p. 779–789, 2019.

MELLO, C. Uso do bagaço de caju reduz em 30 % custos com ração para ruminantes. **ASN**, 15 out. 2015.

MELO, C. A.; JUNIOR, F. H. S.; BISINOTI, M. C.; MOREIRA, A. B.; FERREIRA, O. P. Transforming sugarcane bagasse and vinasse wastes into hydrochar in the presence of phosphoric acid: an evaluation of nutrient contents and structural properties. **Waste and biomass valorization**, v. 8, n. 4, p. 1139–1151, 2017.

MOLLINEDO, J.; SCHUMACHER, T. E.; CHINTALA, R. Influence of feedstocks and pyrolysis on biochar's capacity to modify soil water retention characteristics. **Journal of analytical and applied pyrolysis**, v. 114, p. 100–108, 2015.

MRAW, S. C.; NAAS-O'ROURKE, D. F. Water in Coal Pores: Low-Temperature Heat Capacity Behavior of the Moisture in Wyodak Coal. **Science**, v. 205, n. 4409, p. 901 LP – 902, 31 ago. 1979.

NANDA, S.; MOHANTY, P.; PANT, K. K.; NAIK, S.; KOZINSKI, J. A.; DALAI, A. K. Characterization of North American Lignocellulosic Biomass and Biochars in Terms of their Candidacy for Alternate Renewable Fuels. **Bioenergy Research**, *6*(2), 663-677, 2013.

NOVOTNY, E. H.; MAIA, C. M. B. D. F.; CARVALHO, M. T. D. M.; MADARI, B. E. Revisão De Literatura Biochar : Pyrogenic Carbon For Agricultural Use - A Critical Review. **Revista Brasileira de Ciência do Solo***,* n. 1, p. 321–344, 2015.

NOVAK, J. M.; LIMA, I.; XING, B.; GASKIN, J. W.; STEINER, C.; DAS, K. C.; DAS, K.C.; AHMEDNA, M.; REHRAH, D.; WATTS. D. W.; BUSSCHER, W. J.; SCHOMBERG, H. Characterization of designer biochar produced at different temperatures and their effects on a loamy sand. **Annals of Environmental Science**, 2009.

NWAKA, D.; TAHMASEBI, A.; TIAN, L.; YU, J. The effects of pore structure on the behavior of water in lignite coal and activated carbon. **Journal of Colloid and Interface Science**, v. 477, p. 138–147, 2016.

OLIVEIRA, N. C.; PASCHOAL, A. R.; PAULA, R. J.; CONSTANTINO, I. C.; BISINOTI, M. C.; MOREIRA, A. B.; FREGOLENTE, L. G.; SANTANA, A. M.; SOUSA, F. A.; FERREIRA, O. P.; PAULA, A. J. Morphological analysis of soil particles at multiple length-scale reveals nutrient stocks of Amazonian Anthrosols. **Geoderma**, v. 311, p. 58–66, 2018.

PAVIA, D. L.; LAMPMAN, G. M.; KRIZ, G. S.; VYVYAN, J. A. **INTRODUCTION TO SPECTROSCOPY**. 4. ed. Belmont, CA: Brooks/Cole, 2009.

PRADYOT PATNAIK. **Dean's Analytical Chemistry Handbook**. 2. ed. [s.l.] The McGraw-Hill Companies, Inc., 1995.

QI, Y.; ZHANG, M.; QI, L.; QI, Y. Mechanism for the formation and growth of carbonaceous spheres from sucrose by hydrothermal carbonization. **RSC Adv.**, v. 6, n. 25, p. 20814–20823, 2016.

Queiroz, R. F.; CORRÊA, M. D. M.; CRISOSTOMO, L.; de LIMA, F. F.; CAVALCANTE, R. Aproveitamento do bagaço de caju como fertilizante orgânico em pomar de cajueiro em produção. Embrapa Agroindústria Tropical-Artigo em anais de congresso (ALICE). **Anais,** In: CONGRESSO BRASILEIRO DE FRUTICULTURA, 21., 2010, Natal. Anais.. Natal …, 2010

RAJARAO, R.; MANSURI, I.; DHUNNA, R.; KHANNA, R.; SAHAJWALLA, V. Study of structural evolution of chars during rapid pyrolysis of waste CDs at different temperatures. **Fuel**, v. 134, p. 17–25, 2014.

READ, P. This gift of nature is the best way to save us from climate catastrophe. **The Guardian**, 27 mar. 2009.

ROUQUEROL, J.; AVNIR, D.; FAIRBRIDGE, C. W.; EVERETT, D. H.; HAYNES, J. M.; PERNICONE, N.; Ramsay, J. D. F.; Sing, K. S. W.; UNGER, K. K. Recommendations for the characterization of porous solids (Technical Report). **Pure and Applied Chemistry**, v. 66, n. 8, p. 1739–1758, 1994.

SERRANO, L. A. L.; PESSOA, P. F. A. DE P.; TODO, L. **Aspectos econômicos da cultura do cajueiro**.

SILVA, C. C. Efeito do uso de diferentes aditivos na produção de hidrochar obtido da mistura bagaço de cana-de-açúcar e vinhaça com potencial para aplicação agrícola. [s.l: s.n.].

SILVA, S. H. G.; TEIXEIRA, A. F. S.; MENEZES, M. D.; GUILHERME, L. R. G.; MOREIRA, F. M. S.; CURI, N. Multiple linear regression and random forest to predict and map soil properties using data from portable X-ray fluorescence spectrometer (pXRF). **Ciência e Agrotecnologia**, v. 41, n. 6, p. 648–664, 2017.

SILVERSTEIN, R. M.; WEBSTER, F. X.; KIEMLE, D. J. **Spectrometric Identification of Organic Compounds**. 7. ed. Denvers: John Wiley & Sons, Inc., 2005.

SIQUEIRA, A. M. DE A.; BRITO, E. DE S. Aproveitamento do bagaço do caju para alimentação humana e utilização em outras indústrias de alimentos. **ARAÚJO, JPP Agronegócio caju: práticas e inovações. Brasília, DF: Embrapa**, p. 349–361, 2013.

SOARES, F. H. J. **Carbonização Hidrotérmica Para A Obtenção De Sistemas Inorgânicos-Carbono: Compósitos Magnéticos E Carbono Hidrotérmico Contendo Nutrientes.** Dissertation (Doctor in Physics) – Department of physics, Federal University of Ceará, 2017.

SOHI, S. P.; KRULL, E.; LOPEZ-CAPEL, E.; BOL, R. A review of biochar and its use and function in soil. In: **Advances in agronomy**. [s.l.] Elsevier, 2010. v. 105p. 47–82.

SULIMAN, W.; HARSH, J. B.; ABU-LAIL, N. I.; FORTUNA, A. M.; DALLMEYER, I.; GARCIA-PÉREZ, M. Science of the Total Environment The role of biochar porosity and surface functionality in augmenting hydrologic properties of a sandy soil. **Science of the Total Environment, The**, v. 574, p. 139–147, 2017.

SUN, Y.; GAO, B.; YAO, Y.; FANG, J.; ZHANG, M.; ZHOU, Y.; CHEN, H.; YANG, L. Effects of feedstock type, production method, and pyrolysis temperature on biochar and hydrochar properties. **Chemical Engineering Journal**, v. 240, p. 574–578, 2014.

ŠVÁBOVÁ, M.; WEISHAUPTOVÁ, Z.; PŘIBYL, O. Water vapour adsorption on coal. **Fuel**, v. 90, n. 5, p. 1892–1899, 2011.

TAHMASEBI, A.; YU, J.; SU, H.; HAN, Y.; LUCAS, J.; ZHENG, H.; WALL, T. A differential scanning calorimetric (DSC) study on the characteristics and behavior of water in low-rank coals. **Fuel**, v. 135, p. 243–252, 2014.

TANIGUCHI, C. A. K.; CRISOSTOMO, L. A. **Clima e solo para o cajueiro**. Disponível em: <https://www.spo.cnptia.embrapa.br/conteudo?p_p_id=conteudoportlet_WAR_sistemasdeproducaolf6_1ga1ceportlet&p_p_lifecycle=0&p_p_state=normal&p_p_mode=view&p_p_col_id=column-1&p_p_col_count=1&p_r_p_-76293187_sistemaProducaoId=7705&p_r_p_-996514994_topicoId=1>. Acesso em: 11 dez. 2020.

TEIXEIRA, P. C.; DONAGEMMA, G. K.; FONTANA, A.; TEIXEIRA, W. G. **Manual de métodos de análise de solo**. Rio de Janeiro, Embrapa. 573p, 2017.

TEIXEIRA, W. G.; KERN, D. C.; MADARI, B. E.; LIMA, H. N.; WOODS, W. **As terras pretas de índio da Amazônia : sua caracterização e uso deste conhecimento na criação de novas áreas.** Manaus: Embrapa, 2009.

THOMMES, M.; KANEKO, K.; NEIMARK, A. V.; OLIVIER, J. P.; RODRIGUEZ-REINOSO, F.; ROUQUEROL, J.; SING, K. S. Physisorption of gases, with special reference to the evaluation of surface area and pore size distribution (IUPAC Technical Report). **Pure and Applied Chemistry**, v. 87, n. 9–10, p. 1051–1069, 2015.

TSANEVA, V. N.; KWAPINSKI, W.; TENG, X.; GLOWACKI, B. A. Assessment of the structural evolution of carbons from microwave plasma natural gas reforming and biomass pyrolysis using Raman spectroscopy. **Carbon**, v. 80, p. 617–628, 2014.

What are the types of coal? **USGS**, [s.d.]. Available in: <https://www.usgs.gov/faqs/what-are-types-coal?qt-news_science_products=0#qt-news_science_products>. Accessed in: 11 de dez. de 2020.

UZOMA, K. C.; INOUE, M.; ANDRY, H.; FUJIMAKI, H.; ZAHOOR, A.; NISHIHARA, E. Effect of cow manure biochar on maize productivity under sandy soil condition. **Soil use and management**, v. 27, n. 2, p. 205–212, 2011.

VIEIRA, L. H. E. S. **Preparação E Caracterização De Materiais Híbridos Ferro- Carbono E Avaliação De Suas Propriedades Catalíticas**. Thesis (Masters in Chemestry) – Department of Chemestry, Federal University Of Ceará. Fortaleza, p. 44. 2016.

VIEIRA, L. H. S.; VIEIRA, L. H. S.; SABINO, C. M. S.; SOARES, F. H.; ROCHA, J. S.; CASTRO, M. O.; ALENCAR, R. S.; DA COSTA, L. S.; VIANA, B. C.; DE PAULA, A. J.; SOARES, J. M. Strategic design of magnetic carbonaceous nanocomposites and its application as multifunctional adsorbent. **Carbon**, v. 161, p. 758–771, 2020.

VOLPE, M.; MESSINEO, A.; MÄKELÄ, M.; BARR, M. R.; VOLPE, R.; CORRADO, C.; FIORI, L. (2020). Reactivity of cellulose during hydrothermal carbonization of lignocellulosic biomass**. Fuel Processing Technology**, 206, 106456.

WANG, J.; KASKEL, S. KOH activation of carbon-based materials for energy storage. **Journal of Materials Chemistry**, v. 22, n. 45, p. 23710–23725, 2012.

WANG, X.; CHI, Q.; LIU, X.; WANG, Y. Influence of pyrolysis temperature on characteristics and environmental risk of heavy metals in pyrolyzed biochar made from hydrothermally treated sewage sludge. **Chemosphere**, v. 216, p. 698–706, 2019.

WU, F. C.; WU, P. H.; TSENG, R. L.; JUANG, R. S. Preparation of activated carbons from unburnt coal in bottom ash with KOH activation for liquid-phase adsorption. **Journal of environmental management**, v. 91, n. 5, p. 1097–1102, 2010.

XING, T.; LI, L. H.; HOU, L.; HU, X.; ZHOU, S.; PETER, R.; PETRAVIC, M.; CHEN, Y. Disorder in ball-milled graphite revealed by Raman spectroscopy. **Carbon**, v. 57, p. 515–519, 2013.

YOUSAF, B.; LIU, G.; WANG, R.; ABBAS, Q.; IMTIAZ, M.; LIU, R. Investigating the biochar effects on C-mineralization and sequestration of carbon in soil compared with conventional amendments using the stable isotope (δ13C) approach. **Gcb Bioenergy**, v. 9, n. 6, p. 1085–1099, 2017.

YU, J.; TAHMASEBI, A.; HAN, Y.; YIN, F.; LI, X. A review on water in low rank coals: The existence, interaction with coal structure and effects on coal utilization. **Fuel Processing Technology**, v. 106, p. 9–20, 2013.

YU, J. T.; DEHKHODA, A. M.; ELLIS, N. Development of biochar-based catalyst for transesterification of canola oil. **Energy & Fuels**, v. 25, n. 1, p. 337–344, 2010.

ZHAO, L.; CAO, X.; ZHENG, W.; WANG, Q.; YANG, F. Endogenous minerals have influences on surface electrochemistry and ion exchange properties of biochar. **Chemosphere**, v. 136, p. 133–139, 2015.

ZHAO, Y.; FENG, D.; ZHANG, Y.; HUANG, Y.; SUN, S. Effect of pyrolysis temperature on char structure and chemical speciation of alkali and alkaline earth metallic species in biochar. **Fuel Processing Technology**, v. 141, p. 54–60, 2016.